

Magnetic correlations in the diluted magnetic semiconductor Sn_{1-x}Mn_xTe : an experimental study

Citation for published version (APA):

Vennix, C. W. H. M. (1993). *Magnetic correlations in the diluted magnetic semiconductor Sn_{1-x}Mn_xTe : an experimental study*. [Phd Thesis 1 (Research TU/e / Graduation TU/e), Applied Physics and Science Education]. Technische Universiteit Eindhoven. <https://doi.org/10.6100/IR403381>

DOI:

[10.6100/IR403381](https://doi.org/10.6100/IR403381)

Document status and date:

Published: 01/01/1993

Document Version:

Publisher's PDF, also known as Version of Record (includes final page, issue and volume numbers)

Please check the document version of this publication:

- A submitted manuscript is the version of the article upon submission and before peer-review. There can be important differences between the submitted version and the official published version of record. People interested in the research are advised to contact the author for the final version of the publication, or visit the DOI to the publisher's website.
- The final author version and the galley proof are versions of the publication after peer review.
- The final published version features the final layout of the paper including the volume, issue and page numbers.

[Link to publication](#)

General rights

Copyright and moral rights for the publications made accessible in the public portal are retained by the authors and/or other copyright owners and it is a condition of accessing publications that users recognise and abide by the legal requirements associated with these rights.

- Users may download and print one copy of any publication from the public portal for the purpose of private study or research.
- You may not further distribute the material or use it for any profit-making activity or commercial gain
- You may freely distribute the URL identifying the publication in the public portal.

If the publication is distributed under the terms of Article 25fa of the Dutch Copyright Act, indicated by the "Taverne" license above, please follow below link for the End User Agreement:

www.tue.nl/taverne

Take down policy

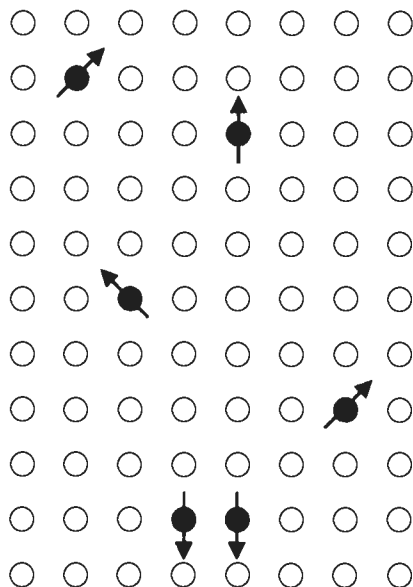
If you believe that this document breaches copyright please contact us at:

openaccess@tue.nl

providing details and we will investigate your claim.

Magnetic correlations in the diluted magnetic semiconductor $\text{Sn}_{1-x}\text{Mn}_x\text{Te}$

An experimental study



C.W.H.M. Vennix

Magnetic correlations in the diluted magnetic semiconductor $\text{Sn}_{1-x}\text{Mn}_x\text{Te}$

An experimental study

PROEFSCHRIFT

ter verkrijging van de graad van doctor aan de
Technische Universiteit Eindhoven, op gezag van
de Rector Magnificus, prof. dr. J.H. van Lint, voor
een commissie aangewezen door het College
van Dekanen in het openbaar te verdedigen op
vrijdag 8 oktober 1993 om 16.00 uur

door

CORNELIS WILHELMUS HENRICUS MARIA VENNIX

Geboren te Oost-, West- en Middelbeers

Dit proefschrift is goedgekeurd door de promotoren

prof. dr. ir. W.J.M. de Jonge

prof. dr. E. Frikkee

en de copromotor

dr. ir. K. Kopinga

The work described in this thesis was performed within a cooperation between the Netherlands Energy Research Foundation ECN, Petten, and the group Cooperative Phenomena of the Solid State Division of the Physics Department of the Eindhoven University of Technology.

Contents

1. Introduction	1
1.1 Introduction	1
1.2 Magnetic interactions in DMS	2
1.3 Carrier-concentration-induced ferromagnetism	4
1.4 Low-temperature magnetic properties of $\text{Sn}_{1-x}\text{Mn}_x\text{Te}$	8
1.5 Scope of the thesis	11
References	12
2. Experimental	15
2.1 Crystal growth	15
2.2 The charge carrier concentration	18
2.3 The crystal structure	20
2.4 Neutron diffraction	24
References	31
3. Characterisation of the ferromagnetic state in $\text{Sn}_{1-x}\text{Mn}_x\text{Te}$	33
3.1 Introduction	33
3.2 Experimental results	35
3.2.1 $\text{Sn}_{0.97}\text{Mn}_{0.03}\text{Te}$ with $p = 7 \times 10^{20} \text{ cm}^{-3}$	35
3.2.2 $\text{Sn}_{0.94}\text{Mn}_{0.06}\text{Te}$ with $p = 11 \times 10^{20} \text{ cm}^{-3}$	37
3.2.3 $\text{Sn}_{0.90}\text{Mn}_{0.10}\text{Te}$ with $p = 14 \times 10^{20} \text{ cm}^{-3}$	41
3.3 Discussion	43
References	45
4. Carrier-concentration-induced ferromagnet to spin-glass transition in $\text{Sn}_{0.96}\text{Mn}_{0.04}\text{Te}$	47
4.1 Introduction	47
4.2 Results of the ac susceptibility, magnetisation, and magnetic specific heat measurements	48
4.2.1 ac susceptibility	48
4.2.2 Magnetisation	54
4.2.3 Magnetic specific heat	56
4.2.4 Provisional conclusions	58
4.3 Neutron diffraction	59
4.3.1 Introduction	59

4.3.2	Results for $\text{Sn}_{0.96}\text{Mn}_{0.04}\text{Te}$ with $p = 7 \times 10^{20} \text{ cm}^{-3}$	59
4.3.3	Results for $\text{Sn}_{0.96}\text{Mn}_{0.04}\text{Te}$ with $p = 11 \times 10^{20} \text{ cm}^{-3}$	61
4.3.4	Results for $\text{Sn}_{0.96}\text{Mn}_{0.04}\text{Te}$ with $p = 23 \times 10^{20} \text{ cm}^{-3}$	66
4.4	Discussion	68
	References	71
5.	The three-dimensional (T,x,p) magnetic phase diagram	73
5.1	Introduction	73
5.2	Survey of experimental data	73
5.3	Model calculations on the x-p magnetic phase diagram	79
5.3.1	Introduction	79
5.3.2	Geometrical model	81
5.3.3	Mean Random Field model	83
5.4	Discussion	85
5.5	Suggestions for further research	88
	References	91
	Summary	93
	Samenvatting	95
	Dankwoord	99
	Curriculum Vitae	100

Chapter 1

Introduction

1.1 Introduction

Diluted magnetic semiconductors (DMS) are compound semiconductors, in which a part of the nonmagnetic cations of the host material has been randomly substituted by magnetic ions. DMS are of interest, from the fundamental as well as from the technological point of view, for three reasons¹: their semiconducting properties, their magnetic properties, and the close relationship between those properties. This coupling results from the interaction between the two subsystems, formed by the electronic system of the charge carriers and the diluted magnetic system of the magnetic ions, respectively. The most thoroughly studied class of DMS consists of the semiconducting II-VI compounds diluted with Mn^{2+} -ions, such as $Cd_{1-x}Mn_xTe$ and $Zn_{1-x}Mn_xSe$. Other classes of DMS are formed by the Mn containing II-V compounds, for example $(Cd_{1-x}Mn_x)_2As_3$, and by the Mn containing IV-VI DMS. The magnetic behaviour of the latter compounds, in particular $Sn_{1-x}Mn_xTe$, will be the subject of this thesis. The reason for the interest in especially this DMS will be elucidated in the next sections. First some general properties of DMS will be described briefly. More information can be found in a number of extensive reviews, on both the semiconducting and the magnetic properties of DMS, that have appeared in recent years.^{1,2,3}

The interest in DMS as semiconductors stems from the ternary (or sometimes quaternary) nature of the alloys, which offers the possibility of changing properties such as the energy gap, the effective mass, and the lattice constant, by varying the composition. This tunability of band parameters makes DMS for example suitable candidates for the application in semiconductor superlattices and heterostructures. The magnetic properties of the diluted magnetic systems DMS are of interest in their own right, apart from their interplay with the electronic properties. Among the DMS materials a variety of magnetic behaviour is found, including paramagnetic, ferromagnetic, antiferromagnetic and spin-glass phases. A brief introduction to the magnetic properties of DMS and the underlying exchange mechanisms will be given in the next section.

The interaction between the localised d electrons, associated with the magnetic moments, and the s- and p-like orbitals of the conduction and/or valence band electrons causes the coupling between the magnetic and electronic subsystems. This so-called sp-d exchange

interaction (J_{sp-d}) makes the band structure of DMS much more sensitive to an external magnetic field than is the case in ordinary semiconductors, leading to the effects that are characteristic for DMS. Examples are the giant Faraday rotation in $Cd_{1-x}Mn_xTe$ and the extremely large negative magneto-resistance observed in $Hg_{1-x}Mn_xTe$.⁴ The effect of the $sp-d$ exchange can be considered as an amplification of the Zeeman-splitting of electronic levels, causing a dependence of the electronic properties of a DMS on the macroscopic magnetisation. This offers an extra possibility for tuning the band structure, namely by varying the magnetic field or the temperature.

1.2 Magnetic interactions in DMS

The magnetic behaviour of DMS is determined by the interactions between the magnetic ions (J_{d-d}). Because the direct overlap of the 3d wave functions can be neglected, these interactions can take place only via indirect processes, in which the interactions are mediated by the itinerant charge carriers. As a result J_{d-d} and J_{sp-d} are strongly related. In principle three different indirect exchange mechanisms can be distinguished: the superexchange (SE) mechanism⁵, the Bloembergen-Rowland⁶ (BR) mechanism, and the Rudermann-Kittel-Kasuya-Yosida⁷ (RKKY) mechanism. Each of these can be described in terms of virtual transitions, induced by $sp-d$ exchange and/or $sp-d$ hybridisation, between band electrons or holes and the d electrons of the Mn ions. The processes are illustrated in Fig. 1.1. The superexchange interaction is an intraband mechanism in which two electrons or two holes are involved. The BR process is an interband one hole - one electron mechanism, in which a valence band electron is scattered across the energy gap into the conduction band. The RKKY mechanism is an intraband two-electron or two-hole

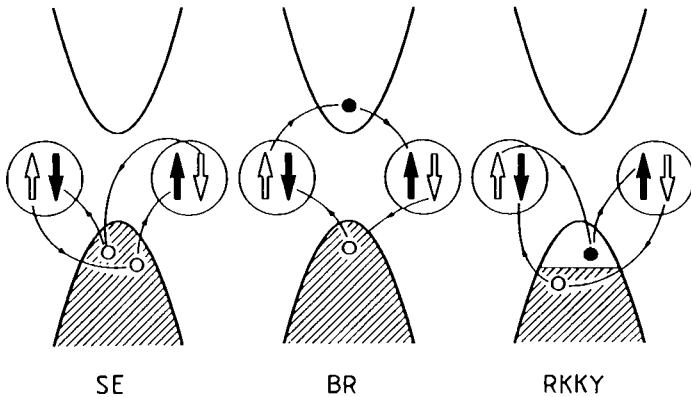


Figure 1.1: Schematic representation of the indirect exchange mechanisms superexchange (SE), Bloembergen-Rowland (BR), and Rudermann-Kittel-Kasuya-Yosida (RKKY). The filled valence bands (shaded), the empty conduction bands and Mn spins in their initial (solid arrow) and final state (open arrow) are shown. Reproduced from Ref. 3.

mechanism, in which only carriers at the Fermi-level are involved. Considering these different mechanisms, the amount at which each of them contributes to the total exchange interaction in a material can be expected to depend on the band structure and on the charge carrier concentration. The superexchange mechanism is dominant for open-gap materials (insulators, semiconductors), the BR mechanism for small-gap materials (semiconductors), and the RKKY interaction for materials with partially filled bands (metals, semimetals). The range of the interactions is the longest for the RKKY mechanism ($J \sim R^{-3}$ for large R), the shortest for the superexchange interaction ($J \sim \exp(-\alpha R^2)$ for large R), and intermediate for the BR mechanism ($J \sim \exp(-\alpha R)$ for large R).

The role of the carrier density in the magnetic behaviour of Mn based DMS is schematically illustrated in Fig. 1.2, where representative examples of DMS are arranged according to their carrier concentrations. On the left-hand side of the diagram the II-VI DMS are located. In all of these compounds long range antiferromagnetic interactions between the Mn ions have been observed, in spite of the wide variety of intrinsic properties such as the band gap and the lattice constant. Depending on the Mn concentration and the temperature range, these interactions can lead to spin-glass phases and antiferromagnetically ordered phases. Larson *et al.*⁸ demonstrated that the major contribution to the exchange interactions, at least for the nearest-neighbour interactions, comes from the superexchange mechanism, whereas the BR interaction accounts for only a few percent. The contribution of the RKKY interaction, which is proportional to the

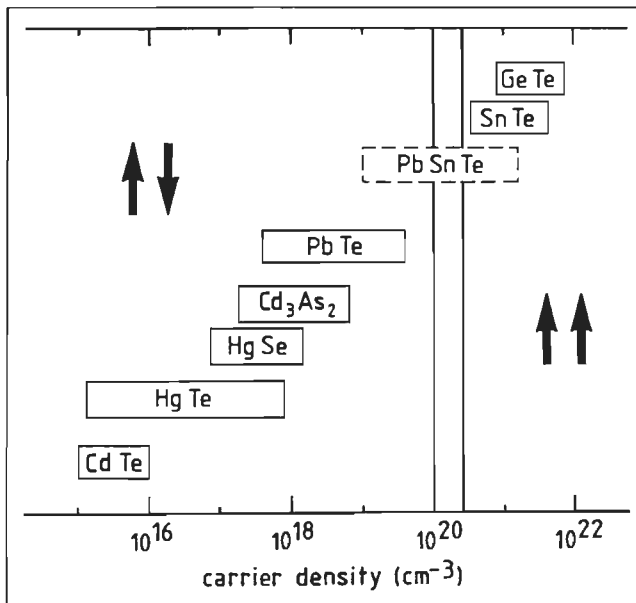


Figure 1.2: Correlation between magnetic interactions and charge carrier concentrations in Mn-based DMS. Antiparallel and parallel arrows indicate antiferromagnetic and ferromagnetic interactions, respectively. After Ref. 3.

carrier concentration, is negligible for this range of carrier densities. De Jonge *et al.*⁹ noted that in these systems nearest-neighbour interactions of the superexchange type alone cannot be responsible for the existence of a spin-glass phase for Mn concentrations below the percolation limit, and hence a long-range tail ($J \sim R^{-7}$) of the interaction must also be present.

On the right-hand side of Fig. 1.2 the IV-VI DMS are situated, which can be divided in two groups, distinguished by the charge carrier concentration. The first group consists of the materials with relatively low carrier concentrations, in the range $10^{17} - 10^{19} \text{ cm}^{-3}$, such as $\text{Pb}_{1-x}\text{Mn}_x\text{Te}$. Their magnetic behaviour closely resembles that of the Mn containing II-VI DMS and can also be attributed to antiferromagnetic interactions of the superexchange type, although the interactions are much weaker than in II-VI DMS.¹⁰ The existence of a spin-glass phase at low temperatures has also been reported for this group of IV-VI DMS, for example for $\text{Pb}_{1-x}\text{Mn}_x\text{Te}$.¹¹ For the second group of IV-VI DMS, consisting of the materials with relatively high charge carrier concentrations, of the order of 10^{21} cm^{-3} , a completely different low-temperature magnetic behaviour is observed. They exhibit ferromagnetic interactions, which can be explained by RKKY interactions, made effective by the high carrier concentration and dominating over the superexchange interactions. Ferromagnetic ordering at low temperatures has been reported in for example $\text{Sn}_{1-x}\text{Mn}_x\text{Te}$ ^{12,13} and $\text{Ge}_{1-x}\text{Mn}_x\text{Te}$.¹⁴

The crucial role of the charge carrier concentration for the magnetic properties of IV-VI DMS becomes especially clear in the intermediate regime, with carrier concentrations of the order $10^{19} - 10^{21} \text{ cm}^{-3}$. This range can be reached either by the preparation of quaternary compounds like $\text{Pb}_{1-x-y}\text{Sn}_y\text{Mn}_x\text{Te}$, or by changing the carrier concentration, which actually originates from slight deviations from stoichiometry, by means of isothermal annealing. The link between the antiferromagnetic interactions, low-carrier-concentration regime and the ferromagnetic interactions, high-carrier-concentration regime in IV-VI DMS was made in 1986 by Story *et al.*¹⁵ by the discovery of the so-called carrier-concentration-induced ferromagnetism in the quaternary compound $\text{Pb}_{0.25}\text{Sn}_{0.72}\text{Mn}_{0.03}\text{Te}$. This phenomenon will be discussed in the next section.

1.3 Carrier-concentration-induced ferromagnetism

Story *et al.*¹⁵ established the existence of a critical carrier concentration $p_c \approx 3 \times 10^{20} \text{ holes/cm}^3$ for the low-temperature magnetic behaviour of $\text{Pb}_{0.25}\text{Sn}_{0.72}\text{Mn}_{0.03}\text{Te}$. In samples with carrier densities below p_c paramagnetic behaviour was observed down to 1.5 K, the lowest temperature covered in their experiments. High-temperature susceptibility measurements on these samples yielded paramagnetic Curie-Weiss temperatures (Θ) equal to $(0.0 \pm 0.2) \text{ K}$. At the critical carrier concentration a step-like increase of the ferromagnetic interactions occurred, probed by a step-like increase in Θ , as can be seen in Fig. 1.3, where the results of Story *et al.*¹⁵ are combined with later results by Swagten *et al.*¹⁶ for other $\text{Pb}_{1-x-y}\text{Sn}_y\text{Mn}_x\text{Te}$ compositions. For $p > p_c$ the ferromagnetic interactions lead to a ferromagnetic ordering at liquid helium temperatures, reflected in characteristic

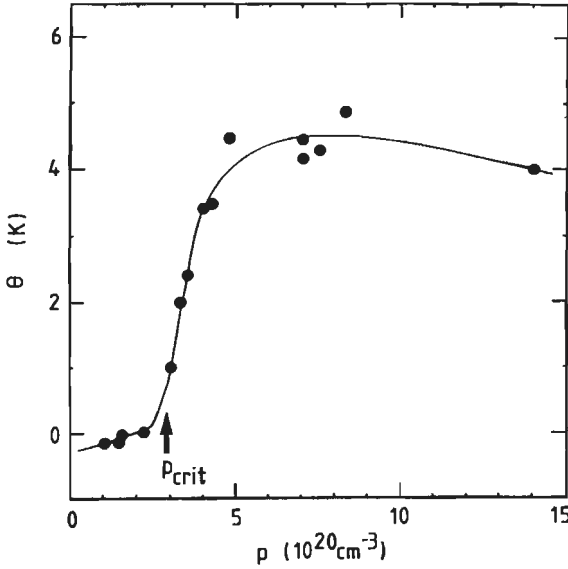


Figure 1.3: Curie-Weiss temperature Θ as a function of the carrier concentration for $\text{Pb}_{0.25}\text{Sn}_{0.72}\text{Mn}_{0.03}\text{Te}$. Data from Refs. 15 and 16 are included. After Ref. 3.

variations of the susceptibility, the magnetisation, and the specific heat. This was the first indication of the fact that, at least for this range of carrier densities, the charge carrier concentration p has to be included as a parameter in the magnetic phase diagram of this group of IV-VI DMS, besides the temperature T and the Mn concentration x . The critical hole concentration p_c can be considered as the boundary between the essentially paramagnetic or weakly antiferromagnetic regime of the low-carrier-concentration materials, such as $\text{Pb}_{1-x}\text{Mn}_x\text{Te}$, and the ferromagnetic regime of the high-carrier-concentration compounds, such as $\text{Ge}_{1-x}\text{Mn}_x\text{Te}$. Story *et al.*¹⁵ suggested that the RKKY interaction would be the only one among the known exchange mechanisms that is sufficiently long ranged and effective in the high-carrier-concentration regime to account for the observed ferromagnetic ordering and the magnitude of the critical temperatures T_c . However, the step-like dependence of Θ on p could not be understood within the framework of the RKKY interaction alone. The results of later experiments¹⁷, in which the shift of T_c under the influence of hydrostatic pressure was studied, suggested that the band structure has also to be taken into consideration to explain the magnetic properties. Doing so, Swagten *et al.*¹⁶ were able to describe the carrier-concentration dependence of Θ displayed in Fig. 1.3 both qualitatively and quantitatively. Since their model will appear to be of interest for the understanding of the magnetic properties of $\text{Sn}_{1-x}\text{Mn}_x\text{Te}$ also, it will be described next.

The general expression for the RKKY interaction between two spins is given by:

$$J(R_{ij}) = \frac{J_{sp-d}^2 (k_F a_0)^6}{64 \pi^3 E_F} F_{RK}(2k_F R_{ij}) \quad (1.1)$$

where J_{sp-d} is the exchange integral between the d electrons associated with the localised moment and the free carriers, a_0 is the lattice constant, k_F is the Fermi wave number, via which $J(R_{ij})$ depends on the carrier concentration ($p \sim k_F^3$), E_F is the Fermi energy, R_{ij} is the distance between the two spins, and

$$F_{RK}(x) = \frac{\sin(x) - x \cos(x)}{x^4} \quad (1.2)$$

is the Rudermann-Kittel function. In Fig. 1.4 $J(R_{ij})$ is sketched for a fixed carrier concentration. The first change of sign of $J(R_{ij})$ occurs for $R_{ij} = R_0$. For $R_{ij} < R_0$ the interaction is positive, implying a ferromagnetic coupling of the spin in the origin to the spins at distances less than R_0 .

The RKKY interaction was originally modelled for metallic materials. The application to the semiconductor $Pb_{1-x}Sn_xMn_xTe$ requires at least two modifications. The first one is the assumption of a finite mean free path (λ) for the itinerant holes, which is introduced by multiplying the right-hand side of Eq. (1.1) with the exponential damping factor $\exp(-R_{ij}/\lambda)$. The second modification embodies the incorporation of the electronic band structure model and is essential in the explanation of the threshold-like dependence of Θ on p . The band structure of the host compound $Pb_{1-y}Sn_yTe$, schematically illustrated

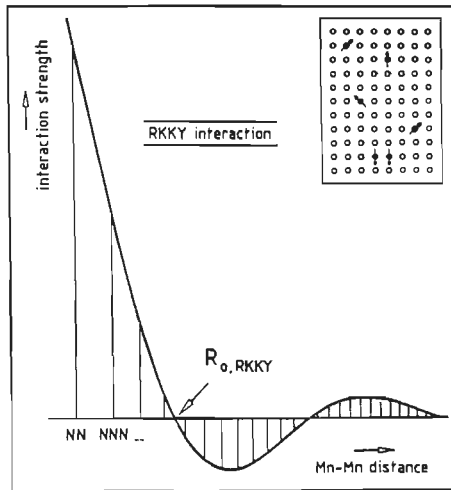


Figure 1.4: Sketch of the RKKY interaction strength as a function of the spin-spin distance at fixed carrier concentration. Vertical lines corresponds to shells of lattice sites, where the randomly distributed (see inset) Mn ions can be located. In this case a spin in the origin is ferromagnetically coupled to spins at sites on the four nearest neighbours shells.

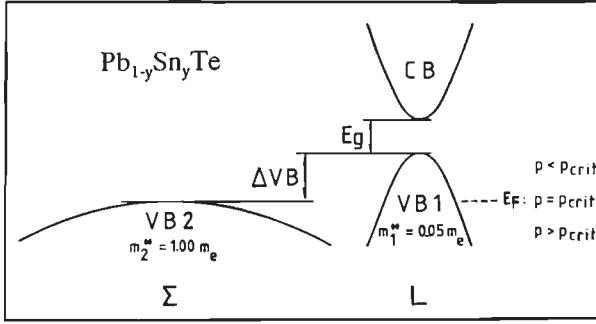


Figure 1.5: Schematic illustration of the band structure of $Pb_{1-y}Sn_yTe$ as it was used in the model calculations of Swagten et al.¹⁶. Reproduced from Ref. 18.

in Fig. 1.5, is assumed to be also appropriate to $Pb_{1-x-y}Sn_yMn_xTe$ for small Mn concentrations. In the present model it is represented by a set of two parabolic valence bands: one located at the L point of the Brillouin-zone (VB1), separated from the conduction band by a direct energy gap E_g , and one located along the Σ axis (VB2). The top of VB2 is lower in energy than the top of VB1 by ΔVB . The carriers in VB1 and VB2 have different effective masses: $m_1^* = 0.05 m_e$ and $m_2^* = 1.00 m_e$.¹⁹ For the calculation of the Curie-Weiss temperature, contributions to the total exchange interaction J_{tot} by carriers from both valence bands have to be taken into account. Using the mean field approximation for the spin system, Θ becomes:

$$\Theta = \frac{2S(S+1)}{3k_B} J_{tot} = \frac{2S(S+1)x}{3k_B} \sum_{i=1}^2 \sum_j z_j J_{VBi}(R_j) \quad (1.3)$$

where k_B is Boltzmann's constant, S is the spin of the Mn ions, x is the concentration of Mn ions, z_j is the number of lattice positions at a distance R_j , and $J_{VBi}(R_j)$ is the contribution to the exchange integral from VB i :

$$J_{VBi}(R_j) = \frac{m_i^* J_i^2 a_0^6}{512 \pi^3 \hbar^2} \frac{\sin(2k_{F,i} R_j) - 2k_{F,i} R_j \cos(2k_{F,i} R_j)}{R_j^4} \exp\left[-\frac{R_j}{\lambda}\right] \quad (1.4)$$

where J_i and $k_{F,i}$ are the sp-d exchange constant and Fermi wave number for VB i , respectively. Eq. (1.4) has been derived from Eq. (1.1) by making use of the parabolicity of the valence bands. In the rocksalt crystal structure of $Pb_{1-x-y}Sn_yMn_xTe$ the Mn ions are located on an fcc sublattice at distances $R_j = a_0(j/2)^{1/2}$ from a reference spin. Figure 1.6 shows the calculated Curie-Weiss temperature Θ_i as a function of the hole concentration for each valence band VB i under the assumption that only that band is occupied. Because J_{VBi} is proportional to m_i^* , Θ_i is always much smaller than Θ_2 for a

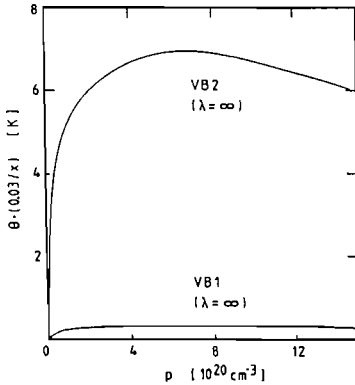


Figure 1.6: Contributions of VB1 and VB2 to the total Curie-Weiss temperature Θ (scaled to $x = 0.03$) as a function of the carrier concentration, under the assumption that only one band is populated. Reproduced from Ref. 18.

fixed hole density. This difference between Θ_1 and Θ_2 is responsible for the steep rise of Θ at p_c (see Fig. 1.3). If E_F is calculated as a function of the charge carrier concentration, p_c appears to be the carrier concentration at which the Fermi-level enters the second valence band and heavy holes begin to contribute to the interaction, causing the steep increase in the ferromagnetic interactions. For $p < p_c$ E_F is located in the top of VB1 and Θ is equal to Θ_1 . For $p > p_c$ the contribution to Θ of the heavy holes in the Σ band dominates, also because the distribution of carriers is strongly shifted towards this band due to the much larger effective mass. Calculations with estimated values for the parameters ($J_1 = J_2 = 0.3$ eV, $\Delta VB = 0.6$ eV, $a_0 = 6.347$ Å, $\lambda \approx 10$ Å) yielded an excellent agreement between the calculated and experimentally observed carrier concentration dependence of Θ . The quantitative agreement was considered to be somewhat fortuitous, because of the rather arbitrarily chosen parameters.¹⁶ The calculated critical density $p_c \approx 2.4 \times 10^{20}$ cm⁻³ is consistent with the value deduced from the magnetic measurements as well as with the value that was deduced from Hall-coefficient measurements on the host compound $Pb_{1-y}Sn_yTe$.¹⁸

The applicability of the two-valence-band model, based on the nonmagnetic host material, to $Pb_{1-x-y}Sn_yMn_xTe$ was experimentally demonstrated more recently by Karczewski *et al.*^{20,21} By means of optical reflectivity measurements they confirmed the existence of heavy carriers in $Pb_{0.25}Sn_{0.72}Mn_{0.03}Te$ and determined the band structure parameters at 77 K, yielding $E_g = (285 \pm 25)$ meV, $\Delta VB = (185 \pm 5)$ meV, and $m_2^* = (1.7 \pm 0.3)m_e$. From the temperature dependence of the Hall-coefficient it was concluded that the Σ band becomes populated at $p = 3 \times 10^{20}$ cm⁻³, in agreement with the critical concentration deduced from the magnetic measurements.^{15,16,21} Story *et al.*²¹ calculated $\Theta(p)$ with the above band structure parameters and $J_{sp-d} = 100$ meV. In their expression for Θ (cf. Eq. (1.3)) they explicitly accounted for the fact that VB1 and VB2 actually consist of four and twelve equivalent valleys, respectively, each of which is an independent channel for the RKKY mechanism. Their results are similar to those of Swagten *et al.*¹⁶, in spite of the different parameters that were used. An antiferromagnetic superexchange contribution between nearest-neighbour spins had to be included to obtain a correct description of the experimental data on $\Theta(p)$ for $p < p_c$ ($J_{AF} = (-0.25 \pm 0.05)$ K, independent of p).

1.4 Low-temperature magnetic properties of $\text{Sn}_{1-x}\text{Mn}_x\text{Te}$

Since $\text{Pb}_{1-x}\text{Mn}_x\text{Te}$ and $\text{Sn}_{1-x}\text{Mn}_x\text{Te}$, which can be considered as limiting cases of the mixed compound $\text{Pb}_{1-x-y}\text{Sn}_y\text{Mn}_x\text{Te}$, have band structures that are qualitatively similar to that of the mixed compound, it is plausible that the difference in their magnetic behaviour is caused by the difference in charge carrier concentration. To verify this conjecture, De Jonge *et al.*²² studied the low-temperature magnetic properties of a number of $\text{Sn}_{1-x}\text{Mn}_x\text{Te}$ samples with $x = 0.03$ and different carrier densities. Previously reported investigations were generally restricted to as-grown samples, i.e. with carrier concentration $p \sim 7 - 11 \times 10^{20} \text{ cm}^{-3}$ (see section 2.2). On basis of the results of a number of experiments, such as measurements of the susceptibility^{12,13,23}, the magnetisation^{12,23}, the specific heat¹³, and the resistivity²⁴, the low-temperature magnetic phase for these carrier concentrations had been characterised as ferromagnetic by several authors. Because of the proportionality of Θ with x , the ferromagnetic interactions were attributed to the RKKY mechanism.¹³ It was suggested²² that, if the two-band model also holds for $\text{Sn}_{1-x}\text{Mn}_x\text{Te}$, a reduction of the carrier concentration below p_c should induce a transformation of the ferromagnetic state into the paramagnetic state. Indeed, positive Curie-Weiss temperatures were found for samples with carrier concentrations $p = 4.5 \times 10^{20} \text{ cm}^{-3}$, $p = 7.0 \times 10^{20} \text{ cm}^{-3}$, and $p = 9.4 \times 10^{20} \text{ cm}^{-3}$, whereas Θ was strongly reduced for a sample with $p = 2.7 \times 10^{20} \text{ cm}^{-3}$, again indicating a critical carrier concentration

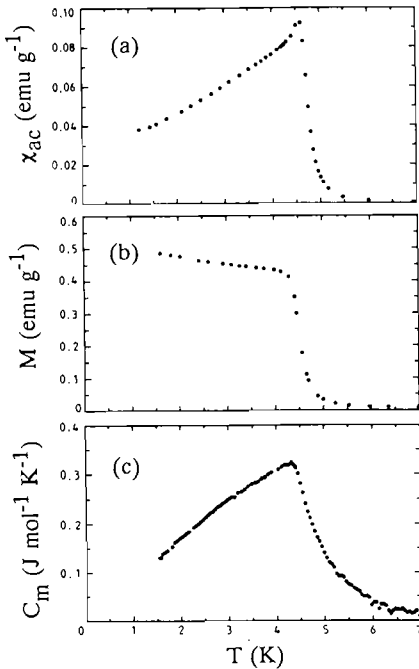


Figure 1.7: (a) *ac* susceptibility, (b) magnetisation ($H = 0.5 \text{ mT}$), and (c) magnetic specific heat of $\text{Sn}_{0.97}\text{Mn}_{0.03}\text{Te}$ with $p > p_c$ ((a), (b) $p = 9.4 \times 10^{20} \text{ cm}^{-3}$, (c) $p = 7.0 \times 10^{20} \text{ cm}^{-3}$). Reproduced from Ref. 22.

$p_c \approx 3 \times 10^{20} \text{ cm}^{-3}$, which is in fair agreement with the value deduced from Hall-effect measurements.²⁵

For samples with $p > p_c$ the ac susceptibility, the magnetisation, and the specific heat showed clearly ferromagnetic-like characteristics, as is illustrated in Fig. 1.7. As was mentioned above, this ferromagnetic behaviour is in agreement with most of the previously reported investigations on the low-temperature magnetic properties of $\text{Sn}_{1-x}\text{Mn}_x\text{Te}$. However, the existence of a spin-glass phase has also been claimed, for example by Hedgcock *et al.*²⁶, who reported a spin-glass transition in a sample with $x = 0.02$ and $p = 4.5 \times 10^{20} \text{ cm}^{-3}$. More extensive studies were reported by Escorne and Mauger and coworkers.^{27,28,29} By means of ac susceptibility and resistivity measurements the (T,x) magnetic phase diagram depicted in Fig. 1.8 was compiled. According to this diagram, for $x \leq 0.03$ a direct transition from the paramagnetic phase to a spin-glass phase occurs, whereas for $0.03 \leq x \leq 0.06$ a double transition occurs: on cooling from the paramagnetic phase an initial transition to a ferromagnetic phase is followed by a transition to a spin-glass phase, which is now called a reentrant spin-glass phase, at lower temperature. For $x \geq 0.06$ the ferromagnetic state should persist down to $T = 0 \text{ K}$. Since the measurements on which Fig. 1.8 is based, were also performed on as-grown samples, i.e. most probably with $p \sim 7 - 11 \times 10^{20} \text{ cm}^{-3}$, these results seem to contradict those indicating a ferromagnetic order and also the predictions of the two-band model used in the description of the carrier-concentration-induced ferromagnetism. These apparent discrepancies were one of the reasons to perform the work described in this thesis.

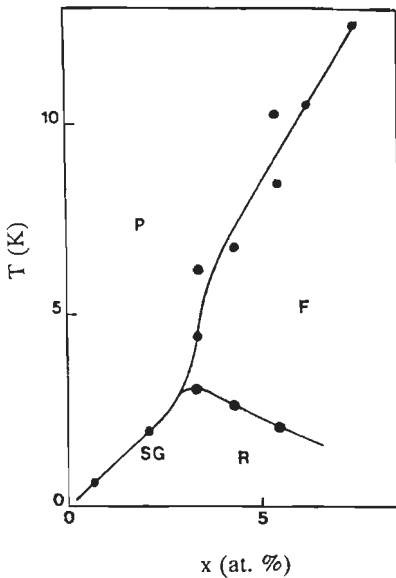


Figure 1.8: (T,x) magnetic phase diagram for $\text{Sn}_{1-x}\text{Mn}_x\text{Te}$. P denotes the paramagnetic phase, S the spin-glass phase, F the ferromagnetic phase, and R the reentrant spin-glass phase. Reproduced from Ref. 29.

1.5 Scope of the thesis

The first aim of the present work is the characterisation of the low-temperature magnetic phase in $\text{Sn}_{1-x}\text{Mn}_x\text{Te}$ with carrier concentrations $p > p_c$, which, as described in the previous section, has earlier been denoted as ferromagnetic as well as (reentrant) spin glass. To determine the actual nature of this phase, single-crystal neutron diffraction experiments were performed. With the aid of neutron diffraction it is possible to gain insight not only in the *nature* of the magnetic correlations, but also in their *range*. Some basic concepts of neutron diffraction will be described in chapter 2 of this thesis, together with a number of experimental aspects, such as the crystal growth, the annealing procedures used to change the carrier concentration of a crystal, and the setup used in the neutron diffraction experiments. Attention will also be paid to the determination of the crystal structure of $\text{Sn}_{1-x}\text{Mn}_x\text{Te}$. Chapter 3 subsequently deals with the determination of the nature of the low-temperature magnetic phase in as-grown, i.e. $p > p_c$, $\text{Sn}_{1-x}\text{Mn}_x\text{Te}$ crystals, with $0.03 \leq x \leq 0.10$, by means of neutron diffraction experiments in combination with measurements of the susceptibility, the magnetisation, and the magnetic specific heat. The second aim of this study is the extension of the three dimensional (T, x, p) magnetic phase diagram of $\text{Sn}_{1-x}\text{Mn}_x\text{Te}$, especially towards higher charge carrier concentrations. Within this framework, the results of an experimental study on the evolution of the magnetic correlations in $\text{Sn}_{0.96}\text{Mn}_{0.04}\text{Te}$ with increasing charge carrier concentration will be presented in chapter 4. In the last chapter a tentative three-dimensional (T, x, p) magnetic phase diagram will be compiled by combining the results presented in chapters 3 and 4 with those on other compositions and charge carrier concentrations. The characteristic features of this diagram will be discussed in the context of the RKKY model described in section 1.3.

References

1. J.K. Furdyna, *J. Appl. Phys.* **64**, R29 (1988).
2. *Diluted Magnetic Semiconductors*, Vol. 25 of *Semiconductors and Semimetals*, J.K. Furdyna and J. Kossut, Eds. (Academic Press, Boston 1988).
3. W.J.M. de Jonge and H.J.M. Swagten, *J. Magn. Magn. Mater.* **100**, 323 (1991).
4. J.K. Furdyna, *J. Appl. Phys.* **53**, 7637 (1982).
5. P.W. Anderson, *Phys. Rev.* **115**, 1 (1959).
6. N. Bloembergen and T.J. Rowland, *Phys. Rev.* **97**, 1679 (1955).
7. M. Rudermann and C. Kittel, *Phys. Rev.* **96**, 99 (1954); T. Kasuya, *Prog. Theor. Phys.* **16**, 45 (1956); K. Yosida, *Phys. Rev.* **106**, 893 (1957).
8. B.E. Larson, K.C. Hass, H. Ehrenreich, and A.E. Carlsson, *Phys. Rev. B* **37**, 4137 (1988).
9. W.J.M. de Jonge, A. Twardowski, and C.J.M. Denissen, in *Diluted Magnetic Semiconductors*, edited by R.L. Aggarwal, J.K. Furdyna, and S. von Molnar, *Mat. Res. Soc. Symp. Proc.* **89**, 153 (1987).
10. G. Bauer, p. 107 in ref. 9.
11. M. Escorne, A. Mauger, J.L. Tholence, and R. Triboulet, *Phys. Rev. B* **29**, 6306 (1984).
12. J. Cohen, A. Globa, P. Mollard, H. Rodot, and M. Rodot, *J. de Phys.* **29** C4, 142 (1968).
13. M. P. Mathur, D.W. Deiss, C.K. Jones, A. Patterson, W.J. Carr, Jr., and R.C. Miller, *J. Appl. Phys.* **41**, 1005 (1970).
14. R.W. Cochrane, F.T. Hedgcock, and J.O. Strom-Olsen, *Phys. Rev. B* **9**, 3013 (1974).
15. T. Story, R.R. Galazka, R.B. Frankel, and P.A. Wolff, *Phys. Rev. Lett.* **56**, 777 (1986).
16. H.J.M. Swagten, W.J.M. de Jonge, R.R. Galazka, P. Warmenbol, and J.T. Devreese, *Phys. Rev. B* **37**, 9907 (1988).
17. T. Suski, J. Igalson, and T. Story, *J. Magn. Magn. Mater.* **66**, 325 (1987).
18. W.J.M. de Jonge, H.J.M. Swagten, R.R. Galazka, P. Warmenbol, and J.T. Devreese, *IEEE Transactions on Magnetics* **24**, 2542 (1988).
19. M. Ocio, *Phys. Rev. B* **10**, 4274 (1974).
20. G. Karczewski, L. Swierkowski, T. Story, A. Sczerbakow, J. Niewodniczanska-Blinowska, and G. Bauer, *Semicond. Sci. Technol.* **5**, 1115 (1990).
21. T. Story, G. Karczewski, L. Swierkowski, and R.R. Galazka, *Phys. Rev. B* **42**, 10477 (1990).
22. W.J.M. de Jonge, H.J.M. Swagten, S.J.E.A. Eltink, and N.M.J. Stoffels, *Semicond. Sci. Technol.* **5**, S131 (1990).
23. U. Sondermann, *J. Magn. Magn. Mater.* **2**, 216 (1976).
24. M. Inoue, M. Tanabe, H. Yagi, T. Tatsukawa, *J. Phys. Soc. Jpn.* **47**, 1879 (1979).
25. R.S. Allgaier and B. Houston, *Phys. Rev. B* **5**, 2186 (1972).
26. F. Hedgcock, P.C. Sullivan, K. Kadowaki, and S.B. Woods, *J. Magn. Magn. Mater.*

-
- 54-57, 1293 (1986).
27. M. Godinho, J.L. Tholence, A. Mauger, M. Escorne, and A. Katty, in *Proc. 17th Int. Conf. Low. Temp. Phys.* (Elsevier, Amsterdam, 1984) p. 647.
 28. M. Escorne, M. Godinho, J.L. Tholence, and A. Mauger, *J. Appl. Phys.* **57**, 3424 (1985).
 29. A. Mauger and M. Escorne, *Phys. Rev. B* **35**, 1902 (1987).

Chapter 2

Experimental

2.1 Crystal growth

The availability of high-quality single crystals is essential for neutron diffraction experiments. Since a phase diagram for the ternary SnMnTe system is not available, the conditions for growing $\text{Sn}_{1-x}\text{Mn}_x\text{Te}$ crystals must be estimated from the phase diagram of SnTe, shown in Fig. 2.1. Fortunately, the presence of Mn has not been reported to drastically alter the characteristic temperatures indicated in Fig. 2.1. Several authors reported the growth of $\text{Sn}_{1-x}\text{Mn}_x\text{Te}$ single crystals containing up to 19 % Mn.² Sondermann³ even claims to have grown homogeneous polycrystalline material with 40 % Mn. Figure 2.1 shows that the $\text{Sn}_{1-y}\text{Te}_y$ stability region near $y = 0.5$ is extremely narrow.

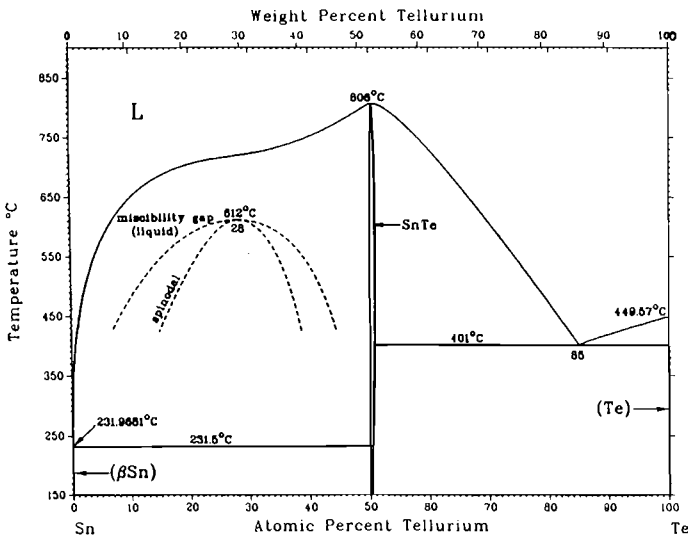


Figure 2.1: Temperature-composition phase diagram of the binary alloy $\text{Sn}_{1-y}\text{Te}_y$, reproduced from Ref. 1.

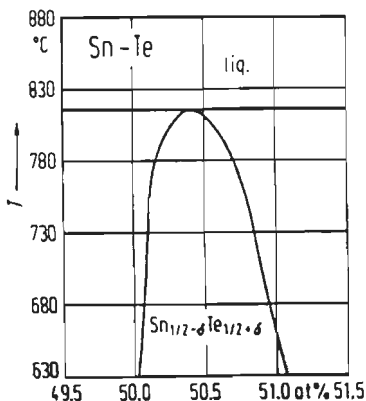


Figure 2.2: Temperature-composition phase diagram of $\text{Sn}_{1-y}\text{Te}_y$, near $y = 0.500$, after Ref. 4.

Fig. 2.2 a more detailed diagram, compiled by Brebick⁴, is presented. The figure shows that the stability area is located completely at the Te rich side and limited to compositions $\text{Sn}_{1-y}\text{Te}_y$ with roughly $0.501 \leq y \leq 0.511$, corresponding with Sn : Te ratios 0.996 : 1 and 0.957 : 1, respectively. Because the melting temperature is maximal, 806 °C, for $y = 0.504$, i.e. Sn : Te = 0.984 : 1, this cation:anion ratio is used for the starting materials.

All crystals used for the experiments described in this thesis were grown by the conventional Bridgman-technique, which is the most commonly used technique for the preparation of DMS crystals.⁵ The Bridgman-setup is illustrated in Fig. 2.3. An ampoule with the molten constituents is slowly moved downwards through a negative temperature gradient in a furnace. As soon as the sharp tip of the ampoule reaches the point in the furnace where the temperature is equal to the melting temperature of the $\text{Sn}_{1-x}\text{Mn}_x\text{Te}$ material to be grown, the growth of a single crystal starts from there. While the ampoule is lowered further, this crystal can in principle grow throughout the ampoule.

The starting materials used are Sn and Te (both 99.999 % pure) and MnTe_2 (99.9 % pure). They are contained in a 13 mm diameter quartz ampoule, which is coated with a carbon layer to prevent chemical reactions of the quartz with the molten constituents. The ampoule is slowly (2.5 °C/min) heated to 860 °C, i.e. approximately 50 °C above the SnTe melting temperature. During the heating process the temperature is kept constant for one hour at the melting temperatures of Sn and Te, 232 °C and 450 °C, respectively. When the temperature has reached 860 °C, it is kept constant for a day. Subsequently the ampoule is shaken during 8 hours to guarantee a homogeneous mixture of the constituents in the melt and to prevent vapour inclusions. After the shaking the ampoule is moved downward at 1 - 2 mm/h and the actual growth of the crystal starts. Crystals with more Mn appear to require a slower lowering. Depending on the lowering rate, it lasts 7 to 14 days before the ampoule reaches the bottom of the furnace, where the temperature is at least 50 °C below the melting temperature. Then the temperature is lowered to 400 °C at 0.5 °C/min, after which the furnace is switched off. Faster cooling increases the risk of cracking of the ampoule. The ampoule remains in the furnace until it is at room temperature.

With 40 g of starting materials the growth results in a batch of approximately 8 cm height

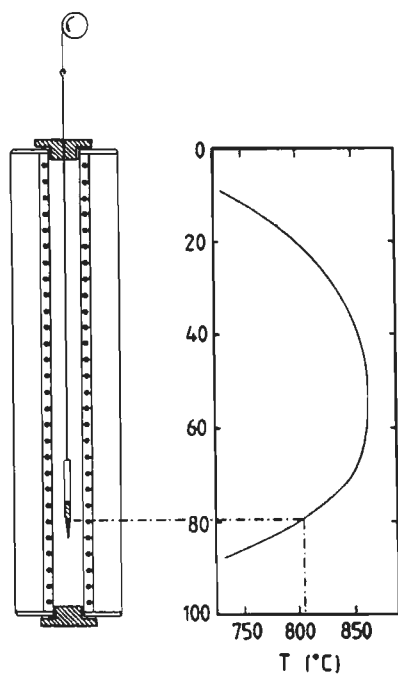


Figure 2.3: Bridgman equipment for the growth of single crystals. The ampoule with the molten constituents is lowered through a furnace (left) with a negative temperature gradient (right). Crystal growth takes place at the point where the temperature in the furnace is equal to the melting temperature of $\text{Sn}_{1-x}\text{Mn}_x\text{Te}$.

in the ampoule. In practice, this batch does not contain one large single crystal, but a number of smaller single crystals with dimensions up to 0.5 cm^3 . Both the size and the quality of these single crystals are sufficient for the use in neutron diffraction experiments. The failure to grow one large single crystal is probably caused by the simultaneous growth of crystals at different places in the ampoule. The crystal growth not only takes place at the interface between the melt and the solidified material, but may start also at the wall of the ampoule. The presence of a temperature gradient in the ampoule in the radial direction might result in crystal-growth nucleation at different points of the solidus-liquidus interface. Minute movements of the ampoule in the radial direction can have the same effect. Apart from this, during the cooling after the growth the contraction of the ampoule can possibly damage the crystal. A reduction of the rate at which the ampoule is lowered through the furnace might increase the size of the formed single crystals.

Neutron- and X-ray powder diffraction measurements have revealed that the prepared $\text{Sn}_{1-x}\text{Mn}_x\text{Te}$ material is single phase. At least 10 % Mn can be incorporated in the SnTe lattice without a reduction of the quality of the crystals. With the aid of electron probe micro analysis (EPMA) it has been checked that there are no variations in composition in the grown batch, neither in the radial, nor in the longitudinal direction. The actual composition is within 10 % equal to the nominal composition. For use in the measurements transverse slices with a typical thickness of 1 to 2 mm are cut from the batch.

2.2 The charge carrier concentration

The charge carrier concentration in IV-VI semiconductors is mainly determined by the number of metal- and nonmetal-vacancies, which create holes and electrons, respectively. Since in the phase diagram the $\text{Sn}_{1-y}\text{Te}_y$ stability region is completely located at the Te rich side (see Fig. 2.2), only p-type conductivity is observed.⁶ From measurements of the partial pressure of $\text{Te}_2(\text{g})$ in equilibrium with $\text{Sn}_{1-y}\text{Te}_y(\text{s})$ Brebick *et al.*⁷ concluded that each Sn vacancy is doubly-ionized and thus contributes two holes. However, when the apparent charge carrier concentration p^* , calculated from measurements of the low-field Hall coefficient R_H as $p^* = 1/R_H e$, is compared to the number of Sn vacancies, a number of holes per Sn vacancy between 2.6 and 3.8 results.⁸ This discrepancy can be explained⁹ by assuming that the actual carrier concentration p is smaller than p^* by a factor r , i.e. $p = r \cdot p^*$. This so-called Hall factor r is a correction factor for an anisotropic Fermi surface and nonparabolic energy bands.¹⁰ For isotropic, parabolic bands r is equal to 1. For $\text{Sn}_{1-y}\text{Te}_y$ the value $r = 0.63 \pm 0.06$ was reported^{8,9}, independent of the carrier concentration for $2 \times 10^{20} \text{ cm}^{-3} \leq p^* \leq 20 \times 10^{20} \text{ cm}^{-3}$. This seems to be in contradiction with later results by Ocio¹¹ and Story *et al.*¹², who reported a carrier-concentration dependent correction factor for the related compound $\text{Pb}_{1-x-y}\text{Sn}_y\text{Mn}_x\text{Te}$, which has a band structure similar to that of $\text{Sn}_{1-y}\text{Te}_y$. The dependence is determined by the distribution of the charge carriers over the two valence bands (see chapter 1), which have different Hall-factors. Considering the similarity in band structure it is more likely that r is p-dependent in $\text{Sn}_{1-y}\text{Te}_y$ also. Because the exact dependence of r on p is not yet known, no correction factor will be used in this thesis. The reported charge carrier concentrations are apparent charge carrier concentrations and will be denoted by the symbol p .

The translation of the temperature vs. composition (T,y) phase diagram of Fig. 2.2 to a temperature vs. carrier concentration (T,p) phase diagram is shown in Fig. 2.4. The deviation from stoichiometry, in this case expressed as the Sn deficiency z in Sn_{1-z}Te , is indicated along the upper horizontal axis. The boundaries in Fig. 2.3, approximately 50.1 % Te and 51.1 % Te, correspond to carrier densities of roughly $2 \times 10^{20} \text{ cm}^{-3}$ and $22 \times 10^{20} \text{ cm}^{-3}$, respectively. Fig. 2.4 indicates that the cation:anion ratio of 0.984, used in the growth of our samples, results in typical as-grown charge carrier concentrations $8 - 10 \times 10^{20} \text{ cm}^{-3}$.

To change the carrier concentration of the samples after the growth, essentially the same isothermal annealing methods are used as for the compilation of the phase diagrams in Figs. 2.2 and 2.4. The sample is metal- or nonmetal-saturated by equilibrating it through the vapour phase with a source material with a known metal-rich or nonmetal-rich composition outside the stability area. In this way the number of Sn vacancies and hence the carrier concentration is changed. Sample and source material are heated to 700 °C in an ampoule, which is filled with 280 mbar Ar to guarantee a homogeneous temperature distribution. Because the source material can be (partly) molten at the annealing temperature, it is physically separated from the sample. Annealing treatments last typically 72 hours and are followed by quenching to room temperature to maintain the equilibrium achieved at 700 °C. To increase the carrier concentration of a sample, the relatively Te

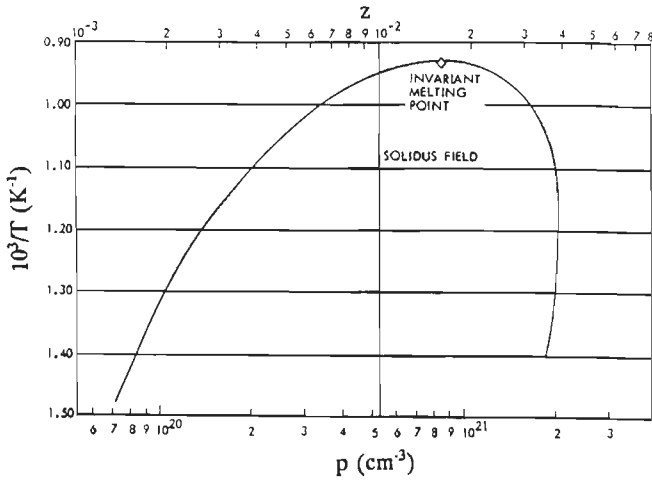


Figure 2.4: Temperature vs. carrier concentration phase diagram of Sn_{1-x}Te . The Sn deficiency z is indicated along the upper horizontal axis.

rich $\text{Sn}_{0.89}\text{Te}$ is used as source material¹⁰, yielding carrier concentrations of typically $20 \times 10^{20} \text{ cm}^{-3}$, which is within the range that may be expected according to Fig. 2.4. The use of pure Te appeared to have a destructive effect on the sample to be annealed. Pure Sn is used as source material to decrease the charge carrier concentration to typically $5 \times 10^{20} \text{ cm}^{-3}$. This is somewhat higher than reported by Brebick⁶ and Savage *et al.*¹³ According to Fig. 2.4, Sn annealing at lower temperatures, for example at 600°C , should result in a lower carrier concentration. However, because of the slower diffusion of the Sn atoms at lower temperatures, this would demand unacceptable long annealing times. Lower carrier concentrations, below the critical value $p_c = 3 \times 10^{20} \text{ cm}^{-3}$, can also be reached by using another source material. Inoue *et al.*¹⁴ reduced the carrier concentration in $\text{Sn}_{1-x}\text{Mn}_x\text{Te}$ crystals with $x \leq 0.022$ to values below $1 \times 10^{20} \text{ cm}^{-3}$ by annealing under Zn vapour at 600°C for two days. We have employed their method on crystals with up to 4 % Mn and succeeded in reducing the carrier density below the critical value. Swagten¹⁵ suggests that this reduction can be ascribed to the more covalent character of the Zn-Te bond compared to the Sn-Te bond. Zn annealing not only leads to the occupation of metal vacancies by Zn, but even to a segregation of Sn. This segregation results in an anomaly in the susceptibility and the magnetisation, caused by the transition to the superconducting state in segregated Sn. From the magnetisation data the number of segregated Sn atoms is estimated to be $(8 \pm 1) \times 10^{19} \text{ cm}^{-3}$, i.e. of the same order of magnitude as the number of metal vacancies.

Investigation of the annealed samples by EPMA showed that the Mn concentration was not changed by the annealing. After the annealing process the quality of the crystals was still sufficient for use in the neutron diffraction experiments.

Carrier concentrations were measured by the Hall effect, using the ac Van der Pauw method. In principle the equipment can be used at liquid-helium temperatures as well

as liquid-nitrogen temperatures. However, since p appears to be independent of temperature below 100 K^{10,13}, in most cases it was measured at 77 K only. To these values will be referred in the rest of this thesis.

2.3 The crystal structure

As will be elucidated in the next section, a detailed knowledge of the low-temperature crystal structure of $\text{Sn}_{1-x}\text{Mn}_x\text{Te}$ is indispensable for the study of the magnetic behaviour by means of single-crystal neutron diffraction experiments. To determine this structure powder neutron diffraction experiments have been performed, the results of which will be discussed at the end of this section. First a survey of the literature on the structure of SnTe will be given.

Several investigations on the low-temperature crystal structure of SnTe have been reported, but no unanimous conclusion has been reached. There is agreement that at room temperature the compound has the NaCl or rocksalt structure, for which the unit cell is depicted in Fig. 2.5. The NaCl structure consists of two fcc sublattices, displaced with respect to each other by one-half of the body diagonal of the unit cell. One of the sublattices is occupied by the metal ions, the other one by the nonmetal ions. For SnTe the room temperature lattice constant decreases with increasing carrier concentration.¹⁶ The controversy about the low-temperature structure concerns the question whether or not SnTe undergoes a structural phase transition from the cubic NaCl structure to a rhombohedrally distorted structure upon cooling from room temperature to 0 K. The related IV-VI semiconductor GeTe is known to undergo such transition^{17,18} with a transition temperature around 670 K. The low-temperature GeTe structure can be viewed¹⁸ as a distorted NaCl structure, in which the Ge sublattice is displaced with respect to the Te sublattice along the $[111]$ direction, and with the lattice expanded along the same direction so that the interaxial angle equals 88.2° at 300 K instead of 90° . Bierly *et al.*¹⁷ studied the structure of the mixed series $\text{Ge}_{1-y}\text{Sn}_y\text{Te}$ by X-ray powder diffraction and found the

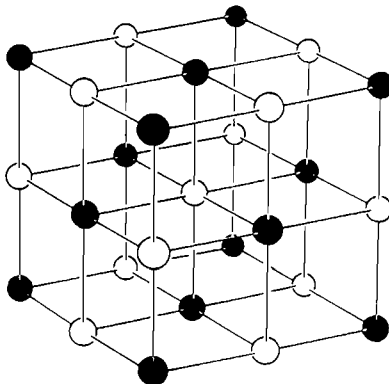


Figure 2.5: NaCl structure. Metal ions and nonmetal ions are alternately arranged at the lattice points of a simple cubic lattice. The metal- and nonmetal sublattices are face centered cubic.

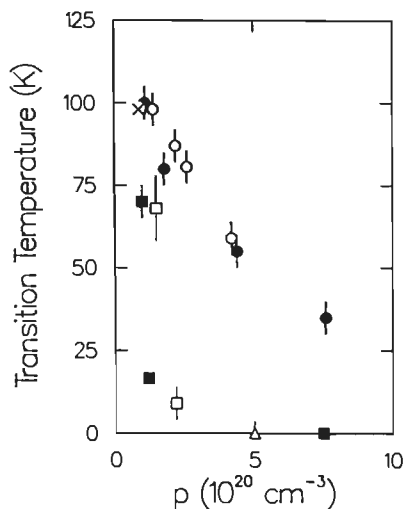


Figure 2.6: Cubic-to-rhombohedral transition temperature in SnTe as a function of charge carrier concentration, determined by means of: (x) elastic neutron scattering²², (\square) Raman-scattering²¹, (\blacksquare) X-ray diffraction²⁰, (\bullet) resistivity measurements²², (\circ) Raman-scattering and resistivity measurements²⁴, and (Δ) inelastic neutron scattering¹⁹.

transition temperature decreasing almost linearly to 0 K with increasing Sn content, but they did not include SnTe in their studies. Later experiments on SnTe yielded contradictory results. There is consensus that the transition temperature depends on the carrier concentration, but there is no agreement on the exact dependence. A few of the experiments will be discussed below. The results are collected in Fig. 2.6.

Pawley *et al.*¹⁹ measured the phonon dispersion relation in an as-grown SnTe sample at several temperatures between 6 K and 300 K by inelastic neutron diffraction. From the temperature dependence of the square of the frequency of the transverse optic phonon at small wave vector it was concluded that in their SnTe sample a structural phase transition, of ferroelectric nature, was only *foreshadowed* in the experiments: it did not actually occur, meaning that the cubic structure remained just stable at 0 K. Muldrew²⁰ studied the splitting of X-ray diffraction lines as a function of temperature for SnTe with different carrier concentrations. A splitting is signalling a distortion of the cubic structure. Samples with $p = 8.4 \times 10^{20} \text{ cm}^{-3}$ and $p = 10 \times 10^{20} \text{ cm}^{-3}$ remained cubic down to 5 K. A sample with $p = 1.0 \times 10^{20} \text{ cm}^{-3}$ transformed from cubic to rhombohedral near 70 K. On cooling from 70 K to 5 K the rhombohedral angle decreased from 90° to 89.895° . By means of Raman-scattering experiments on SnTe single crystals Brillson *et al.*²¹ determined transition temperatures for samples with $p = 1.5 \times 10^{20} \text{ cm}^{-3}$ ($68 \pm 10 \text{ K}$) and $p = 2.2 \times 10^{20} \text{ cm}^{-3}$ ($9 \pm 5 \text{ K}$). They suggested an upper limit for the transformation to occur slightly above $p = 2.2 \times 10^{20} \text{ cm}^{-3}$. Iizumi *et al.*²² investigated a sample with $p = 0.9 \times 10^{20} \text{ cm}^{-3}$ by single-crystal neutron diffraction. They showed that a transition to a rhombohedral phase with the aforementioned sublattice shift gives rise to a strong increase of the intensity of the reflections with odd indices (hkl). The origin of this effect will be clarified in the next section. For their sample the (333) intensity indeed increased (by a factor 40) between 98 K, the transition temperature, and 10 K, accompanied by a 10 % increase of the width of the reflection caused by the splitting of the peak.

All references cited above are in fair agreement with each other. Kobayashi *et al.*²³, however, determined completely different transition temperatures from resistivity measurements on samples with $p = (1.2 - 7.7) \times 10^{20} \text{ cm}^{-3}$. A kink in the resistivity vs. temperature curve was associated with the structural transformation, leading to transition temperatures between 100 K ($p = 1.2 \times 10^{20} \text{ cm}^{-3}$) and 35 K ($p = 7.7 \times 10^{20} \text{ cm}^{-3}$). Sugai *et al.*²⁴ found transition temperatures in the same range, both from resistivity measurements and from Raman-scattering experiments. The Raman-scattering results are in strong contradiction with those obtained by Brillson *et al.*²¹ using the same technique, but no explanation for this obvious discrepancy is given.

Little has been reported about the influence of the substitution of a small fraction of the Sn ions by Mn ions on the crystal structure of SnTe. Sondermann³ reported that at room temperature the NaCl structure is maintained in $\text{Sn}_{1-x}\text{Mn}_x\text{Te}$ up to at least $x = 0.40$, with the lattice constant decreasing almost linearly with increasing Mn content. Yeoh *et al.*²⁵ reported an increase of the lattice constant after Zn annealing, in agreement with the carrier concentration dependence observed for SnTe. The X-ray powder diffraction measurements on our samples confirmed the NaCl structure at room temperature.

Concerning the low-temperature structure of $\text{Sn}_{1-x}\text{Mn}_x\text{Te}$, a transition from the cubic structure to the rhombohedral structure cannot be excluded considering the literature on SnTe. To investigate the occurrence of such a transition we performed neutron diffraction experiments on a powder prepared from an as-grown $\text{Sn}_{0.975}\text{Mn}_{0.025}\text{Te}$ sample at room temperature and at 1.3 K. Fig. 2.7 shows the diffractogram collected at 1.3 K. The data were analysed twice with a Rietveld profile refinement procedure, once using the cubic space group Fm3m and once using the rhombohedral space group R3m. The quality of the refinements is measured by the conventional goodness-of-fit parameter χ^2 and the reliability factor R, defined as:

$$R = \frac{100 \cdot \sqrt{\sum (I_{obs} - \frac{1}{c} I_{calc})^2}}{\sum I_{obs}} \quad (2.1)$$

where c is the scaling factor between the observed and calculated intensities I_{obs} and I_{calc} . The refinements yielded no indication for deviations from the cubic structure. Both at 293 K and at 1.3 K the refinement using Fm3m resulted in lower values for R and χ^2 , see Table I. The deviations from the cubic structure were introduced in the starting parameters of the refinement using R3m as a shift of the Te sublattice relative to the metal sublattice along the [111] direction. Refinement resulted in atomic positions that were within the standard deviation equal to the ideal positions in the cubic structure. Moreover, the diffractogram at 1.3 K showed no split or broadened lines, contrary to what was reported for a SnTe sample with a rhombohedrally distorted structure.²²

As an extra check, an experiment like the one by Iizumi²² described above was performed on a $\text{Sn}_{0.97}\text{Mn}_{0.03}\text{Te}$ crystal with $p = 7 \times 10^{20} \text{ cm}^{-3}$. The (111) intensity appeared to be independent of temperature between 10 K and 100 K, confirming the persistence of the cubic structure down to low temperatures. In the single-crystal neutron diffraction experi-

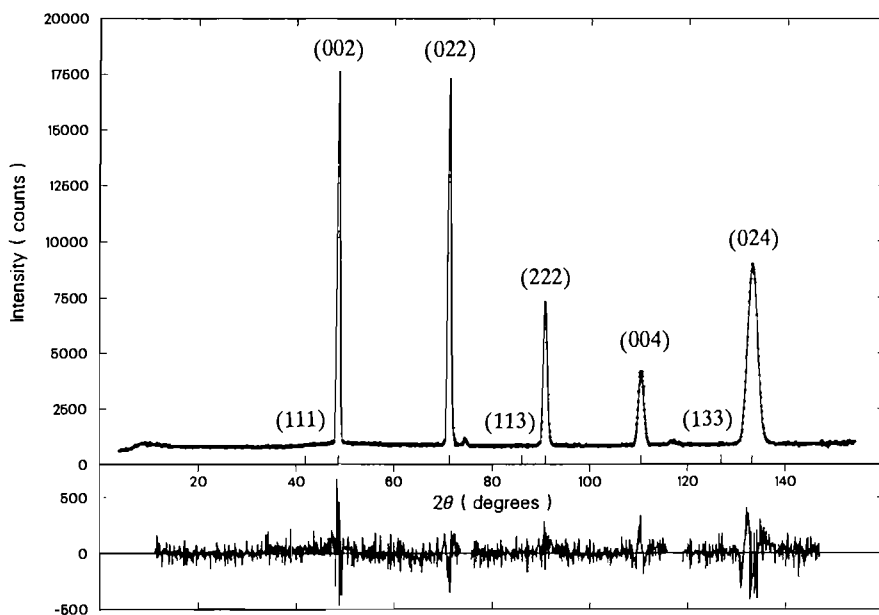


Figure 2.7: Measured (dots) and calculated (full curve) powder diffraction pattern of $\text{Sn}_{0.975}\text{Mn}_{0.025}\text{Te}$, $T = 1.3$ K. The calculated pattern is the result of the refinement using space group $Fm\bar{3}m$. Ticks on the horizontal axis denote the calculated positions of reflections (hkl) indicated in the diagram. The extra peaks near 73° and 117° are due to the vanadium sample-holder. The lower part shows the difference between the observed and the calculated profile.

		$Fm\bar{3}m$	$R\bar{3}m$
T = 293 K	R	0.43	3.82
	χ^2	5.19	10.50
T = 1.3 K	R	0.49	2.96
	χ^2	3.78	4.51

Table 2.1: Quality-of-fit parameters of Rietveld profile refinements of the neutron powder diffraction pattern of $\text{Sn}_{0.975}\text{Mn}_{0.025}\text{Te}$. Refinements were performed using space groups $Fm\bar{3}m$ and $R\bar{3}m$.

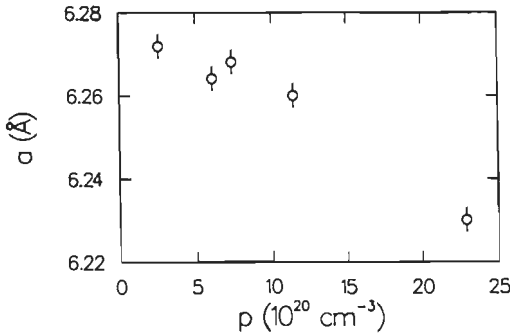


Figure 2.8: Lattice constant of $\text{Sn}_{0.96}\text{Mn}_{0.04}\text{Te}$ at liquid helium temperatures versus charge carrier concentration.

ments to be discussed in the next chapters this conclusion was corroborated: for none of the studied combinations of Mn content and charge carrier concentration indications for deviations from the cubic NaCl structure were found. It is beyond the scope of this thesis to investigate whether this is due to the particular carrier concentrations, which are all above the critical value $2.2 \times 10^{20} \text{ cm}^{-3}$ suggested by Brillson *et al.*²¹, or to the presence of the Mn ions. However, considering the relatively small fraction of Mn, our results seem to refute those of Kobayashi *et al.*²³ and Sugai *et al.*²⁴

In the next section it will be clarified that the study of magnetic ordering phenomena in $\text{Sn}_{1-x}\text{Mn}_x\text{Te}$ by means of single-crystal neutron diffraction is very much facilitated by the cubic crystal structure. To conclude this section the lattice constant of $\text{Sn}_{0.96}\text{Mn}_{0.04}\text{Te}$ at liquid helium temperatures, determined by single-crystal neutron diffraction, is displayed versus the carrier concentration in Fig. 2.8. As is the case for SnTe, the lattice constant decreases with increasing carrier concentration. At a fixed carrier concentration the lattice constant decreases with increasing Mn content, in agreement with the room temperature data.³

2.4 Neutron diffraction

In this section the theory of neutron scattering will be treated as far as necessary for the interpretation of the experiments. First the general expressions for the nuclear and magnetic scattering cross sections for a crystal will be given, and next it will be demonstrated that, in spite of the relatively small number of magnetic atoms, it is possible to observe magnetic scattering in $\text{Sn}_{1-x}\text{Mn}_x\text{Te}$. For a more elaborate review of the theory of neutron scattering from condensed matter the reader is referred to the textbook by Lovesey.²⁶

A single neutron with velocity v can be characterised by a plane wave with wavelength λ , wave vector $k = m_n v / \hbar$ with $|k| = 2\pi/\lambda$, and kinetic energy $E = \hbar k^2 / 2m_n$. In a scattering process the wave vector and the energy of the incoming neutron are changed. If the initial and final wave vectors and energies are denoted by k_i, k_f and E_i, E_f , respectively,

the transfer of wave vector and energy to the crystal can be written as:

$$\mathbf{Q} = \mathbf{k}_f - \mathbf{k}_i \quad (2.2)$$

where \mathbf{Q} is called the scattering vector, and

$$\hbar\omega = E_f - E_i = \frac{\hbar^2}{2m_n} (k_f^2 - k_i^2) \quad (2.3)$$

We consider the scattering of neutrons by a rigid crystal, consisting of N unit cells, each filled with n atoms. The unit cell is defined in terms of three basic vectors \mathbf{a} , \mathbf{b} , and \mathbf{c} , and has a volume $V_0 = \mathbf{a} \cdot (\mathbf{b} \times \mathbf{c})$. The positions of the atoms in the unit cell are denoted by the position vectors $\mathbf{r}_j = x_j\mathbf{a} + y_j\mathbf{b} + z_j\mathbf{c}$, where (x_j, y_j, z_j) are the fractional coordinates of atom j . The translation symmetry of the crystal in real space can be represented by a unit cell in reciprocal space, which is defined by the reciprocal basic vectors \mathbf{a}^* , \mathbf{b}^* , and \mathbf{c}^* , given by $\mathbf{a}^* = 2\pi(\mathbf{b} \times \mathbf{c})/V_0$ etc.. A lattice vector $\boldsymbol{\tau}$ in reciprocal space is denoted as $\boldsymbol{\tau} = h\mathbf{a}^* + k\mathbf{b}^* + l\mathbf{c}^*$, where h, k, l are called the Miller-indices.

The differential cross section $d\sigma/d\Omega$ for elastic (i.e. $E_f = E_i$), coherent nuclear scattering by such crystal into a solid angle $d\Omega$ is given by:

$$\left(\frac{d\sigma}{d\Omega} \right) = N \frac{(2\pi)^3}{V_0} \sum_{\boldsymbol{\tau}} \delta(\mathbf{Q} - \boldsymbol{\tau}) |F_N(\boldsymbol{\tau})|^2 \quad (2.4)$$

$F_N(\boldsymbol{\tau})$ is the nuclear structure factor of the crystallographic unit cell, defined as:

$$F_N(\boldsymbol{\tau}) = \sum_{j=1}^n \langle b_j \rangle \exp(i\boldsymbol{\tau} \cdot \mathbf{r}_j) \quad (2.5)$$

where $\langle b_j \rangle$ denotes the average nuclear scattering length of the atoms at position \mathbf{r}_j . Eq. (2.4) implies that no coherent elastic nuclear scattering occurs from a perfect crystal lattice, unless \mathbf{Q} coincides with a reciprocal lattice vector, which can be shown to correspond to Bragg's law

$$2 d_{hkl} \sin\theta = n\lambda \quad (2.6)$$

where 2θ is the scattering angle and d_{hkl} is the distance between the lattice planes corresponding to the reflection with Miller-indices (hkl) .

The analogue of Eq. (2.4) for elastic coherent magnetic scattering by an ordered array of spins is:

$$\left(\frac{d\sigma}{d\Omega}\right) = N \frac{(2\pi)^3}{V_0} \sum_{\tau} \delta(\mathbf{Q} - \tau) \sin^2\alpha |\mathbf{F}_M(\tau)|^2 \quad (2.7)$$

α is the angle between the scattering vector \mathbf{Q} and the alignment direction of the spins. Only spin components perpendicular to the scattering vector contribute to the magnetic scattering. $\mathbf{F}_M(\tau)$ is the structure factor of the magnetic unit cell and is actually a vector, defined as:

$$\mathbf{F}_M(\tau) = \sum_{j=1}^n \langle \mathbf{p}_j \rangle \exp(i\tau \cdot \mathbf{r}_j) \quad (2.8)$$

$\langle \mathbf{p}_j \rangle$ denotes the average magnetic scattering length of the ions at position \mathbf{r}_j and is defined as:

$$\langle \mathbf{p}_j \rangle = \frac{\gamma e^2}{m_e c^2} \langle \mathbf{S}_j \rangle f_j(\tau) \quad (2.9)$$

where γ is the neutron gyromagnetic ratio ($\gamma = -1.913$), e and m_e are the charge and the mass of the electron, respectively, and c is the speed of light. The factor $\gamma e^2/m_e c^2$ is equal to -5.39 fm, which is of the same order of magnitude as the nuclear scattering lengths. $\langle \mathbf{S}_j \rangle$ denotes the average spin of the ions located at \mathbf{r}_j . The magnetic form factor $f_j(\tau)$ is associated with the magnetic ions and accounts for the fact that the moment is not concentrated at \mathbf{r}_j but is characterised by a spin density distribution around \mathbf{r}_j . The form factor decreases with increasing $|\tau|$.

In the case of ferromagnetic order the magnetic unit cell is the same as the crystallographic unit cell. From Eq. (2.7) it can be seen that in this case the magnetic Bragg-scattering occurs at the same reciprocal lattice points as the nuclear scattering and hence the magnetic and nuclear diffraction peaks are superimposed. The ratio of the magnetic contribution I_{magn} to the nuclear contribution I_{nuc} for any Bragg-peak is determined from Eqs. (2.4) and (2.7) as:

$$I_{\text{magn}} : I_{\text{nuc}} = \langle \sin^2\alpha \rangle \cdot \frac{F_M^2}{F_N^2} \quad (2.10)$$

where $\sin^2\alpha$ has to be averaged over all possible domain orientations.

We will now show that the particular combination of crystal structure and nuclear scattering lengths in $\text{Sn}_{1-x}\text{Mn}_x\text{Te}$ allows the observation of magnetic scattering, in spite

of the small number of magnetic ions.

The unit cell of the NaCl structure (see Fig. 2.5) contains four formula units. The metal ions are located at $(0,0,0)$, $(1/2,1/2,0)$, $(1/2,0,1/2)$, and $(0,1/2,1/2)$, the Te ions at $(1/2,1/2,1/2)$, $(0,0,1/2)$, $(0,1/2,0)$, and $(1/2,0,0)$. When these positions are inserted in the expression for the nuclear structure factor $F_N(\tau)$ (Eq. (2.5)), it turns out that $F_N(\tau) = 0$, unless the indices h,k,l are all even or all odd. Assuming a stoichiometric composition, the respective structure factors are:

$$F_N = 4[b_{Te} + (1-x)b_{Sn} + xb_{Mn}] \quad h,k,l = 2n \quad (2.11a)$$

$$F_N = 4[b_{Te} - (1-x)b_{Sn} - xb_{Mn}] \quad h,k,l = 2n + 1 \quad (2.11b)$$

Insertion of the appropriate scattering lengths ($b_{Te} = 5.80$ fm, $b_{Sn} = 6.23$ fm, $b_{Mn} = -3.73$ fm) shows that for the latter subset of reflections the nuclear structure factor can be reduced to zero by choosing $x = 0.043$. There is no composition for which the first subset of reflections is suppressed. Obviously the subset with odd indices is the most favourable one for the study of ferromagnetic ordering phenomena and, because the magnetic form factor decreases with increasing $|\tau|$, especially the (111) reflection. The compositions we studied ($0.03 \leq x \leq 0.10$) are close enough to $x = 0.043$ to reduce the nuclear contribution to the reflections with odd indices almost to zero. This is also illustrated by the powder diffractogram in Fig. 2.7, where only the reflections with even indices are visible.

As described in the previous section, a rhombohedral distortion of the cubic structure can be viewed as a small displacement of the metal- and nonmetal-ions from the ideal cubic positions along the [111] direction. This shift in position induces a strong increase of the nuclear structure factor for the reflections with odd (hkl). Using Eq. (2.5) it can be shown that a shift (δ, δ, δ) results in a ratio between the nuclear (111) intensities in the rhombohedral and the cubic structure, I_R and I_C , respectively, equal to:

$$I_R : I_C = \cos^2(6\pi\delta) + \frac{((1-x)b_{Sn} + xb_{Mn} + b_{Te})^2}{((1-x)b_{Sn} + xb_{Mn} - b_{Te})^2} \sin^2(6\pi\delta) \quad (2.12)$$

Using this relation Iizumi *et al.*²² proved that the crystal structure of the SnTe crystal they studied was rhombohedrally distorted, with $\delta = 0.004$ at 10 K. For the sample with $x = 0.03$, for which we found that the nuclear (111) intensity was temperature independent between 10 K and 100 K, the effect of a rhombohedral distortion would have been even stronger.

Only the Mn^{2+} ions contribute to the magnetic structure factor. For a multi-domain single crystal the ratio between the magnetic and nuclear (111) intensities becomes:

$$I_{\text{magn}} : I_{\text{nucl}} = \frac{2}{3} \left(\frac{\gamma e^2}{m_e c^2} \right)^2 \langle S \rangle^2 f^2(111) \frac{1}{(b_{\text{Te}} - (1-x)b_{\text{Sn}} - xb_{\text{Mn}})^2} \quad (2.13)$$

The factor $2/3$ results from averaging of the $\sin^2\alpha$ term in Eq. (2.7) over equivalent magnetisation directions in a cubic structure, assuming that equivalent domain types contain equal numbers of spins. The magnetic form factor of the Mn^{2+} ion has the value²⁷ $f(111) = 0.815$. $\langle S \rangle$ is the average spin of the ions at the Sn/Mn lattice sites. Inserting $\langle S \rangle = x \cdot 5/2$ in Eq. (2.13) yields the maximum ratio of the magnetic to the nuclear intensity for a multi-domain ferromagnet at zero temperature, i.e. with full alignment of the Mn^{2+} spins within each domain. Fig. 2.9 shows the dependence of this ratio on the Mn concentration.

The single-crystal diffraction experiments were performed on the HB3 triple-axis spectrometer at the HFR Petten, depicted schematically in Fig. 2.10. The wavelength of the incident neutrons was 0.1428 nm. Two 30° Soller-collimators were placed between the reactor and the C(002) monochromator and between the sample and the C(002) analyser, respectively. To suppress second order contamination of the incoming beam, a tuned pyrolytic graphite filter was installed between the monochromator and the sample. With a pair of Helmholtz-coils, mounted outside the variable temperature liquid He cryostat, a magnetic field up to 5.0 mT could be applied perpendicular to the horizontal scattering plane. The lowest temperature reached in the experiments on HB3 was approximately 1.7 K.

For all crystals the profile of the (111) reflection was studied as a function of temperature, by scans either along the [110] or along the [001] direction. Measurements were performed both with and without the analyser to examine the presence of inelastic scattering.

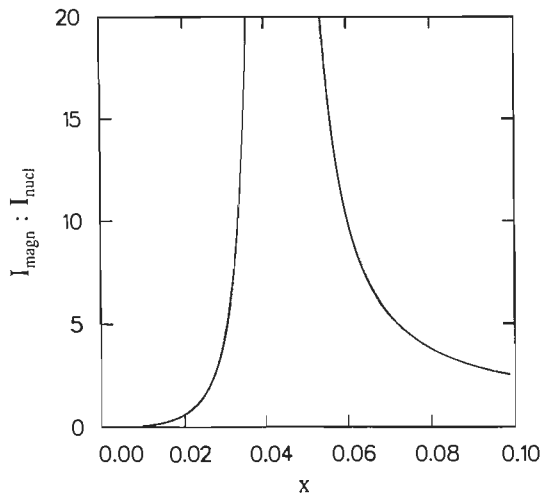


Figure 2.9: Ratio of the magnetic (111) intensity to the nuclear (111) intensity versus the Mn concentration x in $\text{Sn}_{1-x}\text{Mn}_x\text{Te}$. The ratio has been calculated assuming perfect stoichiometry.

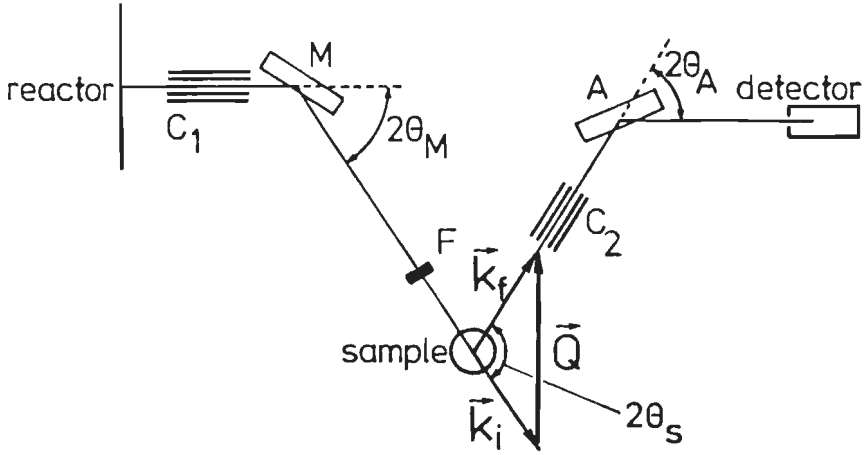


Figure 2.10: Schematic drawing of the triple-axis spectrometer HB3 at the HFR Petten. C_1 and C_2 are Soller-collimators, M and A are the monochromator and analyser crystals, respectively, and F is the filter.

Moreover, by the installation of the analyser the contribution of the second order (222) reflection to the scattered intensity at the (111) position was further reduced. Besides the (111) reflection, the (222) reflection was also measured at a few temperatures for each crystal. The purpose of these measurements was twofold. First, it could be checked whether intensity variations of the (111) reflection were indeed of magnetic origin, and not due to any structural changes, and, second an absolute value for the magnetisation could be deduced from the relation between the integrated magnetic (111) intensity $I_{\text{magn}}(111)$ and the integrated nuclear (222) intensity $I_{\text{nuc}}(222)$. With the aid of Eqs. (2.4) and (2.7), and under the same assumptions that were made in the derivation of Eq. (2.13), this relation can be written as:

$$I_{\text{magn}}(111) = \frac{2}{3} \left(\frac{\gamma e^2}{m_e c^2} \right)^2 \langle S \rangle^2 f^2(111) \frac{\sin 2\theta(222)}{\sin 2\theta(111)} \times \frac{1}{b_{\text{Te}} + (1-x)b_{\text{Sn}} + xb_{\text{Mn}}} I_{\text{nuc}}(111) \quad (2.14)$$

The $\sin 2\theta$ factors in this equation result from the proportionality of the scattered intensity for a given reflection with the so called Lorentz-factor, which is a geometrical factor, equal to $1/\sin 2\theta$ for single-crystal diffraction.

Integrated intensities of measured reflection profiles were generally determined in two ways. In the first method the integrated intensity is determined by fitting the measured profile with a Gaussian peak shape and a constant background:

$$I = B + I_0 \exp \left[-4 \ln 2 \frac{q^2}{(FWHM)^2} \right] \quad (2.15)$$

Here B is the background intensity, I_0 is the scattered intensity in the centre of the peak, and $FWHM$ is the full width at half maximum of the peak. q is the distance between the reciprocal lattice points Q ($= (Q_x, Q_x, 1)$ or $(1, 1, Q_z)$) and $(1, 1, 1)$. $FWHM$ and q are expressed in reciprocal lattice units. For a cubic lattice $1 \text{ r.l.u.} = 2\pi/a$. In the case of $\text{Sn}_{1-x}\text{Mn}_x\text{Te}$ $1 \text{ r.l.u.} \approx 1 \text{ \AA}^{-1}$. Of course, this method to determine the integrated intensity can only be applied if the observed profile has a Gaussian shape. The second method consists of a point-by-point summation over the measured profile. It has the advantage that it can be used regardless of the precise shape of the profile, but yields no estimate for the background intensity.

Besides the analysis of the composite, i.e. nuclear plus magnetic, (111) profile, a detailed study of the separated (111) magnetic profile was performed. The details of this analysis will be presented in the sections where the experimental results will be discussed.

References

1. *Binary Alloy Phase Diagrams*, T.B. Massalski, Ed. (American Society for Metals, Metals Park, Ohio 1986); K.C. Hsieh, M.S. Wei, and Y.A. Chang, *Z. Metallkde.* **74**, 330 (1983).
2. See for example M. Escorne and A. Mauger, *J. Phys. (Paris)* **40**, 347 (1979); M. Inoue, M. Tanabe, H. Yagi, and T. Tatsukawa, *J. Phys. Soc. Jpn.* **47**, 1879 (1979).
3. U. Sondermann, *J. Magn. Magn. Mater.* **2**, 216 (1976).
4. R.F. Brebick, *Prog. Solid State Chem.* **3**, 213 (1966).
5. W. Giriat and J.K. Furdyna in *Diluted Magnetic Semiconductors*, Vol. 25 of *Semiconductors and Semimetals*, J.K. Furdyna and J. Kossut, Eds. (Academic Press, Boston 1988).
6. R.F. Brebick, *J. Phys. Chem. Solids* **24**, 27 (1963).
7. R.F. Brebick and A.J. Strauss, *J. Chem. Phys.* **41**, 197 (1964).
8. R.F. Brebick, *J. Phys. Chem. Solids* **32**, 551 (1971).
9. B.B. Houston, R.S. Allgaier, J. Babiskin, and P.G. Siebenmann, *Bull Am. Phys. Soc.* **9**, 60 (1964).
10. C.R. Hewes, M.S. Adler, and S.D. Senturia, *J. Appl. Phys.* **44**, 1327 (1973).
11. M. Ocio, *Phys. Rev. B* **10**, 4274 (1974).
12. T. Story, G. Karczewski, L. Swierkowski, and R.R. Galazka, *Phys. Rev. B* **42**, 10477 (1990).
13. H.T. Savage, B. Houston, and J.R. Burke, Jr., *Phys. Rev. B* **6**, 2292 (1972).
14. M. Inoue, H. Yagi, T. Muratani, and T. Tatsukawa, *J. Phys. Soc. Jpn.* **40**, 458 (1976).
15. H.J.M. Swagten, Ph. D. thesis, Eindhoven University of Technology 1990.
16. R.F. Bis and J.R. Dixon, *J. Appl. Phys.* **40**, 1919 (1969).
17. J.N. Bierly, L. Muldawer, and O. Beckman, *Acta. Met.* **11**, 447 (1963).
18. J. Goldak, C.S. Barrett, D. Innes, and W. Youdelis, *J. Chem. Phys.* **44**, 3323 (1966).
19. G.S. Pawley, W. Cochran, R.A. Cowley, and G. Dolling, *Phys. Rev. Lett.* **17**, 753 (1966).
20. L. Muldawer, *J. Nonmetals* **1**, 177 (1973).
21. L.J. Brillson, E. Burstein, and L. Muldawer, *Phys. Rev. B* **9**, 1547 (1974).
22. M. Iizumi, Y. Hamaguchi, K.F. Komatsubara, and Y. Kato, *J. Phys. Soc. Jpn.* **38**, 443 (1975).
23. K.L.I. Kobayashi, Y. Kato, Y. Katayama, and K.F. Komatsubara, *Phys. Rev. Lett.* **37**, 772 (1976).
24. S. Sugai, K. Murase, S. Katayama, S. Takaoka, S. Nishi and H. Kawamura, *Solid State Commun.* **24**, 407 (1977).
25. T.S. Yeoh, S.G. Teoh, and H.K. Fun, *J. Phys. Soc. Jpn.* **57**, 3820 (1988).
26. S.W. Lovesey, *Theory of Neutron Scattering from Condensed Matter* (Clarendon Press, Oxford, 1984).
27. R.E. Watson and A.J. Freeman, *Acta. Cryst.* **14**, 27 (1961).

Chapter 3

Characterisation of the ferromagnetic state in $\text{Sn}_{1-x}\text{Mn}_x\text{Te}$

3.1 Introduction

In section 1.4 a survey was given of the literature on the low-temperature magnetic properties of $\text{Sn}_{1-x}\text{Mn}_x\text{Te}$. Investigations by several authors, generally on samples with as-grown carrier concentrations, i.e. $p \sim 10 \times 10^{20} \text{ cm}^{-3}$, yielded apparently contradictory results. In most cases the low-temperature magnetic phase was reported to be ferromagnetic, but the existence of a (reentrant) spin-glass phase at low temperatures was also reported (see the magnetic phase diagram in Fig. 1.8). De Jonge *et al.*¹ demonstrated that a carrier-concentration-induced transition to a 'ferromagnetic-like' state, as was reported for $\text{Pb}_{1-x}\text{Sn}_y\text{Mn}_x\text{Te}$, also occurs in $\text{Sn}_{1-x}\text{Mn}_x\text{Te}$. However, their measurements of the ac susceptibility, the magnetisation, and the magnetic specific heat could not supply definite evidence on the nature of the low-temperature magnetic phase for carrier concentrations $p > p_c$. Especially the observed differences between the field-cooled and zero-field-cooled magnetisation and the field dependence of the ac susceptibility caused confusion, because these features could be related to a (reentrant) spin-glass transition as well as a ferromagnetic domain structure. As described in section 1.5, one of the aims of the work described in this thesis was to remove this ambiguity and determine the actual nature of the magnetic ordering at low temperatures in $\text{Sn}_{1-x}\text{Mn}_x\text{Te}$ samples with as-grown, i.e. $p > p_c$, carrier concentrations. For this purpose single-crystal neutron diffraction experiments have been performed on samples with $x = 0.03$, $x = 0.06$, and $x = 0.10$. According to the magnetic phase diagram of Mauger and Escorne² (see Fig. 1.8) the $x = 0.03$ crystal should be on the edge between a direct transition from the paramagnetic phase to a spin-glass phase and a reentrant spin-glass transition, i.e. via an intermediate ferromagnetic phase. The crystal with $x = 0.06$ should display a double transition on cooling from the paramagnetic phase: a first transition to a ferromagnetic phase near 10 K and a second one to a reentrant spin-glass phase near 2 K. For the crystal with $x = 0.10$ the ferromagnetic phase is expected to persist down to $T = 0$ K. In the diffraction experiments a ferromagnetic ordering will result in magnetic Bragg intensity superimposed on the nuclear Bragg-reflections below the transition temperature T_c , as was elucidated

in section 2.4. In the case of a reentrant spin-glass, the para- to ferromagnet transition will lead to an increase of the Bragg intensity with decreasing temperature, until the transition temperature to the spin-glass phase is reached, below which the intensity will fall off again. Such behaviour has for example been observed in $\text{Eu}_{1-x}\text{Sr}_x\text{S}$.³ Because in the spin-glass phase the magnetic moments are frozen in random directions, no increase of the Bragg-intensity should be observed if a direct transition to a spin-glass phase takes place.

For all samples measurements were performed both in double- and in triple-axis mode, with the analyser set at zero energy transfer in the latter case. The diffraction experiments were combined with measurements of the ac susceptibility, the magnetisation, and the magnetic specific heat. The ac susceptibility was measured with a mutual inductance bridge, using a 1.6 μT , 913 Hz driving ac field. For the magnetisation measurements a fluxgate magnetometer was used. The specific heat was measured with a heat pulse calorimeter. The magnetic part of the specific heat was obtained by subtracting the lattice specific heat, i.e. the specific heat of the host material SnTe, from the raw $\text{Sn}_{1-x}\text{Mn}_x\text{Te}$ data.

In the next section the experimental results for $x = 0.03$, $x = 0.06$, and $x = 0.10$ will subsequently be discussed. To finish this section, the carrier concentrations and the experimentally determined Mn concentrations of the samples are listed in Table 3.1. The Mn concentrations were not only checked with EPMA, but they were also determined by fitting high-temperature susceptibility and magnetisation data to a Curie-Weiss law, using $S = 5/2$ and $g = 2$. For the $x = 0.03$ and $x = 0.06$ samples the experimentally determined values are in good agreement with the nominal values. For the sample with nominally $x = 0.10$ the experimentally determined values indicate that the actual concentration is somewhat lower: $x \approx 0.094$.

x (%) (nominal)	p (10^{20} cm^{-3})	x (%) (EPMA)	x (%) (H.T. χ)	Θ (K) (H.T. χ)	x (%) (H.T. M)	Θ (K) (H.T. M)
3.0	7.0 ± 0.3	3.0 ± 0.3	2.9 ± 0.1	5.5 ± 0.2	---	---
6.0	11.0 ± 0.3	6.5 ± 0.3	6.3 ± 0.1	11.5 ± 0.2	5.8 ± 0.2	10.9 ± 0.2
10.0	13.6 ± 0.4	9.5 ± 0.3	9.2 ± 0.1	15.9 ± 0.2	9.4 ± 0.2	16.3 ± 0.2

Table 3.1: Properties of the samples used in the experiments described in section 3.2. Mn concentrations are expressed in % Mn. The charge carrier concentrations were measured at 77 K. Θ and x were determined from high-temperature susceptibility (H.T. χ) and high-temperature magnetisation measurements (H.T. M).

3.2 Experimental results

3.2.1 $\text{Sn}_{0.97}\text{Mn}_{0.03}\text{Te}$ with $p = 7 \times 10^{20} \text{ cm}^{-3}$

The $x = 0.03$ sample used in the neutron diffraction experiments was the same as the one used in the specific heat measurements by De Jonge *et al.*¹, the results of which are reproduced in Fig. 1.7. In Fig. 3.1a the integrated intensity of Gauss-fits to the (111) profile, observed in triple-axis configuration, is presented as a function of temperature. The behaviour in double-axis mode was qualitatively similar. The data in Fig. 3.1a indicate a transition to a ferromagnetically ordered phase, in agreement with the measurements of the ac susceptibility and the magnetic specific heat, presented in Figs. 3.1b and 3.1c, respectively. From the neutron diffraction data the transition temperature T_c is determined as the temperature where the intensity starts to increase, in this case $T_c = 4.9 \pm 0.2 \text{ K}$. This value is in fair agreement with the (more accurately determinable) value from the susceptibility measurements, $T_c = 4.6 \pm 0.1 \text{ K}$, i.e. the temperature where dx/dT is maximal. From the specific heat data T_c is usually determined as the temperature where C_m has its maximum, in this case $T_c = 4.3 \pm 0.1 \text{ K}$, which is somewhat lower than the value determined from the susceptibility experiments.

The magnetic intensity in Fig. 3.1a is superimposed on the temperature independent nuclear (111) intensity and $\lambda/2$ (222) intensity. The curve in Fig. 3.1a is based on a mean-field calculation of the temperature dependence of the square of the magnetisation for a three-dimensional (3d) ferromagnet with $S = 5/2$ and $T_c = 4.9 \text{ K}$. The good agreement between the data and the curve suggests a qualitatively perfect mean-field-like behaviour of the magnetisation. To obtain quantitative agreement the calculated curve was scaled along the intensity axis, which actually means a scaling of the Mn concentration. The quantitative agreement can be evaluated on basis of the measured (002), (220), and (222) intensities, from which a 'theoretical' value for the maximum magnetic (111) intensity can be calculated using Eq. (2.14). Assuming a multi domain single crystal with the nominal $x = 0.03$, the observed maximum magnetic intensity amounts to a fraction of (0.95 ± 0.27) of the calculated value. The large error is caused by a discrepancy between the value calculated from the (002) intensity on the one hand and those from the (220) and (222) intensities on the other hand. The observed fraction (0.95 ± 0.27) corresponds to a magnetisation of (0.98 ± 0.14) of the saturation value, suggesting a complete alignment of the spins within the domains and thus a ferromagnetic ordering. For the scaling of the mean-field curve in Fig. 3.1a this fraction 0.95 was used.

Because of the low Mn concentration, a detailed analysis of the shape of the separated magnetic (111) reflection, obtained by subtracting the (111) profile observed at $T > T_c$ from those observed below T_c , is not possible in this case. However, within the experimental accuracy the full width at half maximum (FWHM) of the magnetic reflections is equal to the experimental resolution, even immediately below T_c . This implies that the ferromagnetic order is long ranged.

The susceptibility data plotted in Fig. 3.1b were already included in Fig. 2 of Ref. 1. They show the characteristic features of a ferromagnetic transition. First, there are sharp

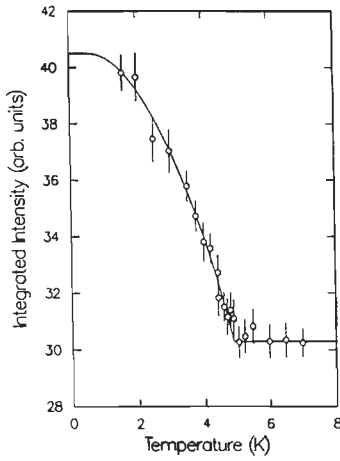
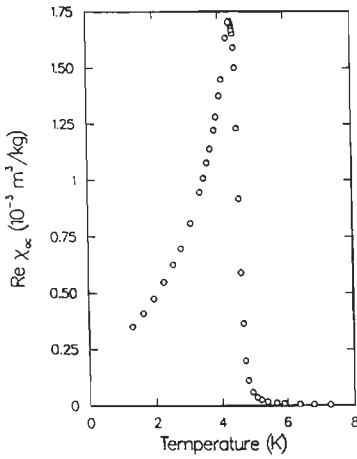
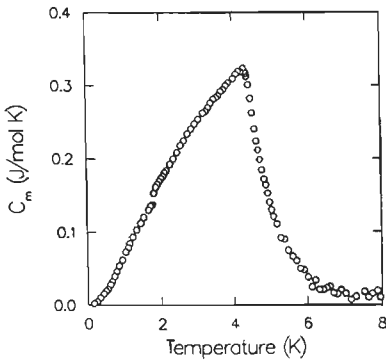


Figure 3.1: $\text{Sn}_{0.97}\text{Mn}_{0.03}\text{Te}$, $\rho = 7 \times 10^{20} \text{ cm}^{-3}$.

a: Temperature dependence of the integrated (111) intensity, triple-axis mode. Full curve: mean-field approximation for $S = 5/2$ and $T_c = 4.9 \text{ K}$, scaled along the intensity axis to obtain quantitative agreement with the data.



b: Real component of the ac susceptibility versus temperature.



c: Magnetic specific heat versus temperature.

transitions in both the real and the imaginary (not shown) component, at the same T_c as the increase of the intensity in Fig. 3.1a occurs. Second, the maximum value of the real component of the susceptibility is of the order of $1/N$, where N is the demagnetising factor of the sample. Apart from this, T_c is approximately equal to the Curie-Weiss temperature Θ obtained from the high-temperature susceptibility data.

Mean-field characteristics are not only observed in the neutron diffraction data, but also in the magnetic specific heat plotted in Fig. 3.1c. The data for $T > 1.5$ K are the same as in Fig. 1.7c. New data have been included in the range $0.2 \text{ K} < T < 1.5 \text{ K}$. The raw data in this temperature range have been corrected for the nuclear hyperfine contribution of the Mn ions. Subtraction of this term ($\sim 1/T^2$, see for example references 4 and 5) results in a smooth decrease down to $C_m = 0 \text{ J/molK}$ for $T = 0 \text{ K}$, which is in agreement with the mean-field theory for a ferromagnet, in which C_m is proportional to MdM/dT . The shape of the C_m versus T curve resembles the lambda shape predicted by mean-field theory. An analysis of the magnetic entropy S_m shows that 85 % of the theoretical value $S_m = xR \ln(2S + 1)$ is recovered in the temperature range up to 10 K. This reduced value might be caused by subtraction of a too large lattice specific heat. Possibly in this temperature range the lattice specific heat of SnTe is reduced by substitution of a few percent Mn. Approximately 84 % of the experimental entropy (i.e. 71 % of the theoretical entropy) is recovered below $T = 4.3 \text{ K}$, the temperature where C_m has its maximum, which is in good agreement with the theoretical value for a 3d fcc Heisenberg ferromagnet (83 %).⁶ A calculation of the entropy gained below 4.6 K, the T_c determined from the susceptibility experiments, yields that 89 % of the experimental entropy (76 % of the theoretical entropy) is gained below this temperature.

Summarizing, the experimental data for the $x = 0.03$, $p = 7 \times 10^{20} \text{ cm}^{-3}$ sample indicate that its low-temperature magnetic phase is long-range-ordered ferromagnetic. Contrary to what is indicated by the phase diagram of Mauger and Escorne² in Fig. 1.8, no evidence is found for the existence of a (reentrant) spin-glass phase for this combination of Mn concentration and charge carrier concentration.

3.2.2 $\text{Sn}_{0.94}\text{Mn}_{0.06}\text{Te}$ with $p = 11 \times 10^{20} \text{ cm}^{-3}$

In Fig. 3.2a the integrated intensity of Gauss-fits to the (111) reflection is displayed versus temperature for the sample with $x = 0.06$ and $p = 11 \times 10^{20} \text{ cm}^{-3}$. The data in the figure are obtained from the triple-axis measurements, but the behaviour in double-axis mode was qualitatively the same. Similar to the sample with $x = 0.03$, on cooling the intensity remains constant until the transition temperature to the ferromagnetically ordered phase is reached. In this case $T_c = 9.3 \pm 0.2 \text{ K}$, which is confirmed by the results of the susceptibility ($T_c = 9.2 \pm 0.1 \text{ K}$) and specific heat measurements ($T_c = 9.0 \pm 0.1 \text{ K}$), shown in Figs. 3.2b and c, respectively. The curve in Fig. 3.2a represents the mean-field approximation for a 3d ferromagnet with $S = 5/2$ and $T_c = 9.3 \text{ K}$, again scaled along the intensity axis to obtain quantitative agreement with the data. In the specific heat measurements about 95 % of the theoretical entropy is recovered in the temperature range

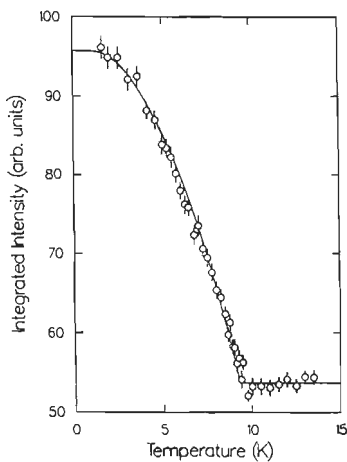
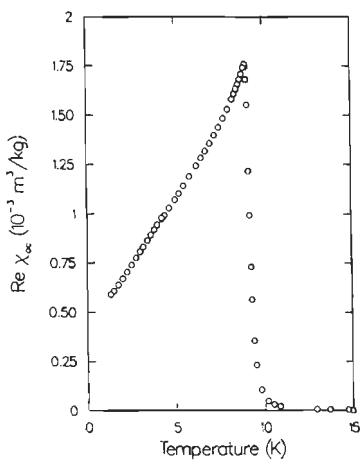
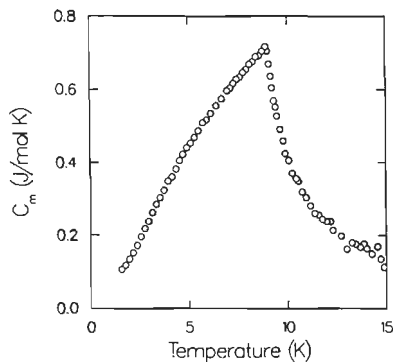


Figure 3.2: $\text{Sn}_{0.94}\text{Mn}_{0.06}\text{Te}$, $\rho = 11 \times 10^{20} \text{ cm}^{-3}$.

a: Temperature dependence of the integrated (111) intensity, triple-axis mode. Full curve: mean-field approximation for $S = 5/2$ and $T_c = 9.3 \text{ K}$, scaled along the intensity axis to obtain quantitative agreement with the data.



b: Real component of the ac susceptibility versus temperature.



c: Magnetic specific heat versus temperature.

up to 20 K. Below $T = 9.0$ K, the temperature where C_m has its maximum, 79 % of this experimental entropy (75 % of the theoretical entropy) is recovered. This 79 % is in good agreement with the theoretically predicted value (83 %) for a 3d fcc Heisenberg ferromagnet.⁶ The results in Fig. 3.2 indicate that the $x = 0.06$, $p = 11 \times 10^{20} \text{ cm}^{-3}$ crystal displays a ferromagnetic ordering at low temperatures, just like the sample with $x = 0.03$ and $p = 7 \times 10^{20} \text{ cm}^{-3}$. However, a few comments must be made in the present case. The first comment concerns the magnetisation calculated from the neutron diffraction data. The maximum observed magnetic (111) intensity amounts to only (0.57 ± 0.03) of the value calculated from the strong nuclear reflections, corresponding to a magnetisation of only (0.75 ± 0.02) of the maximum value expected for the nominal Mn concentration and $S = 5/2$. This is illustrated in Fig. 3.3, where the magnetisation calculated from the neutron diffraction data in Fig. 3.2a is presented as a function of temperature. This magnetisation has been calculated by separating the magnetic (111) intensity from the total observed intensity by subtracting the temperature independent intensity observed for $T > T_c$, subsequently scaling this magnetic intensity to the maximum magnetic (111) intensity calculated from the nuclear reflections and then taking the square root. The curves in Fig. 3.3 are the results of a mean-field calculation for a 3d ferromagnet with $S = 5/2$ and $T_c = 9.3$ K. The dashed curve is based on the maximum value calculated from the strong nuclear reflections and the solid curve is obtained by scaling the dashed line to the experimental data by multiplying with a factor 0.75 along the vertical axis. To gain insight in the cause of this reduction of the magnetisation, high-field magnetisation measurements have been performed. The magnetisation was measured as a function of

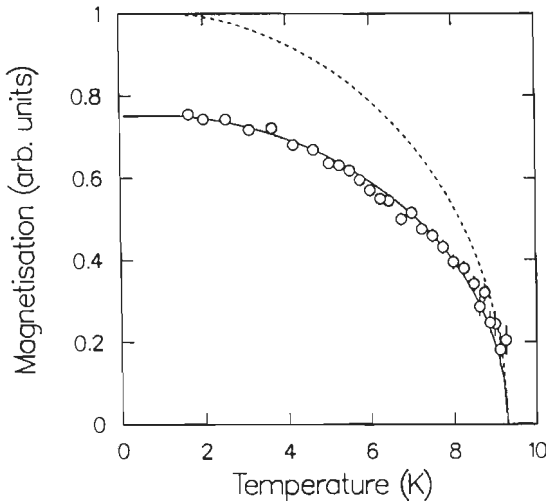


Figure 3.3: $\text{Sn}_{0.94}\text{Mn}_{0.06}\text{Te}$, $p = 11 \times 10^{20} \text{ cm}^{-3}$. Temperature dependence of the magnetisation deduced from the magnetic (111) intensity, scaled to the theoretical maximum value calculated from the nuclear (222) intensity. Dashed curve: mean-field approximation with $S = 5/2$ and $T_c = 9.3$ K, based on the theoretical maximum value. Full curve: same as the dashed curve, but scaled to the experimental data.

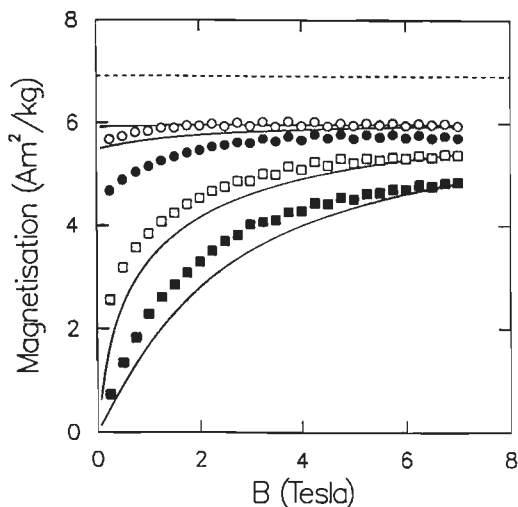


Figure 3.4: $\text{Sn}_{0.94}\text{Mn}_{0.06}\text{Te}$, $p = 11 \times 10^{20} \text{ cm}^{-3}$. Magnetisation as a function of the magnetic field at $T = 2.0 \text{ K}$ (\circ), $T = 4.0 \text{ K}$ (\bullet), $T = 10.0 \text{ K}$ (\square), and $T = 14.0 \text{ K}$ (\blacksquare). Full curves: mean-field approximations for $S = 5/2$, $T_c = 9.3 \text{ K}$, and $x = 0.052$. Dashed line: theoretical saturation magnetisation for $x = 0.06$ and $S = 5/2$.

the field up to $B = 7 \text{ T}$ at a number of temperatures. The results of these measurements are displayed in Fig. 3.4. At $T = 2.0 \text{ K}$ the magnetisation saturates at a field of approximately 2 T , but the observed saturation value amounts to only 86% of the theoretical value for $x = 0.06$ and $S = 5/2$. This theoretical saturation value is indicated by the dashed line in Fig. 3.4. The solid lines are the results of mean-field calculations with $T_c = 9.3 \text{ K}$ and $S = 5/2$, which have been scaled to $x = 0.052$, on basis of the measurement at 2.0 K . The overall agreement with the data is reasonable. At measurement temperatures below T_c the saturation is slower than predicted by the mean-field approximation, which is probably related to the fact that domain effects are neglected in the mean-field approximation. Although the observed magnetisation is somewhat higher than the value deduced from the neutron diffraction experiments, where 75% of the theoretical magnetisation was observed, yet it is significantly below the theoretical saturation value. Possible origins of this reduced magnetisation will be discussed in section 3.3.

The second comment on the ferromagnetically ordered phase concerns the analysis of the separate magnetic (111) profiles. In Fig. 3.5 the FWHM of Gauss-fits to these magnetic profiles is displayed versus temperature for both the double- and the triple-axis measurements. In the latter case the magnetic FWHM is within the experimental accuracy equal to the experimental resolution, determined as the FWHM of the nuclear (111) reflection immediately below 9 K , suggesting that the ferromagnetic order is already long ranged just below 9 K . In double-axis configuration, however, the width of the magnetic profile is significantly larger than the experimental resolution between 7 K and 9 K . This difference between the results with and those without analyser indicates

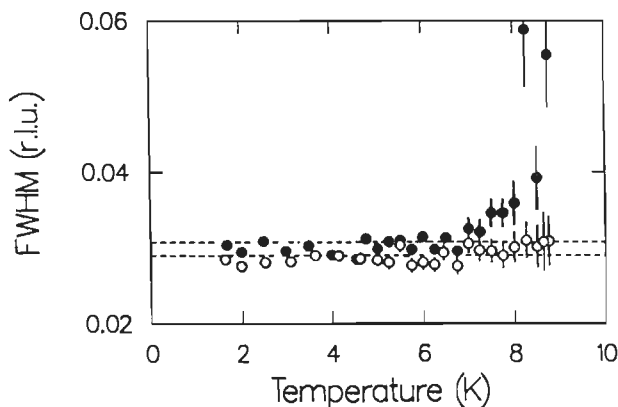


Figure 3.5: $\text{Sn}_{0.94}\text{Mn}_{0.06}\text{Te}$, $p = 11 \times 10^{20} \text{ cm}^{-3}$. Full width at half maximum of Gauss-fits to the magnetic (111) reflection versus temperature. (\circ) triple-axis mode, (\bullet) double-axis mode. Dashed lines: experimental resolution in triple- (lower) and double-axis mode (upper).

that in a region of a few K just below T_c there are spins or spin-components that are fluctuating and not yet long-range correlated. Only below 7 K the magnetic order has become entirely long ranged.

Despite the above comments, the continuously increasing intensity with decreasing temperature, in combination with the susceptibility and specific heat results, leads to the conclusion that the low-temperature magnetic phase in the crystal with $x = 0.06$ and $p = 11 \times 10^{20} \text{ cm}^{-3}$ is ferromagnetically ordered. In the temperature range covered in the present experiments no indications are found for (reentrant) spin-glass behaviour.

3.2.3 $\text{Sn}_{0.90}\text{Mn}_{0.10}\text{Te}$ with $p = 14 \times 10^{20} \text{ cm}^{-3}$

The integrated (111) intensity in triple-axis mode and the ac susceptibility of the crystal with $x = 0.10$ and $p = 14 \times 10^{20} \text{ cm}^{-3}$ are presented as a function of temperature in Figs. 3.6a and 3.6b, respectively. Again, the integrated intensity in double-axis mode showed a qualitatively similar temperature dependence. Similar to the data for the samples with $x = 0.03$, $p = 7 \times 10^{20} \text{ cm}^{-3}$ and $x = 0.06$, $p = 11 \times 10^{20} \text{ cm}^{-3}$ samples, the results displayed in Fig. 3.6 indicate a transition to a ferromagnetically ordered phase. In this case the critical temperature is determined as $T_c = 14.2 \pm 0.2 \text{ K}$ from the neutron diffraction experiments and as $T_c = 14.1 \pm 0.1 \text{ K}$ is from the susceptibility experiments. The curve is again the result of a mean-field calculation with $S = 5/2$ and in this case $T_c = 14.2 \text{ K}$ and has been scaled along the vertical axis.

The FWHM of the magnetic (111) reflection is equal to the experimental resolution immediately below T_c , both in double- and in triple-axis mode, which implies that the ferromagnetic order is long ranged. However, the magnetisation calculated by scaling the observed magnetic intensity to the nuclear (002), (220), and (222) intensities yields

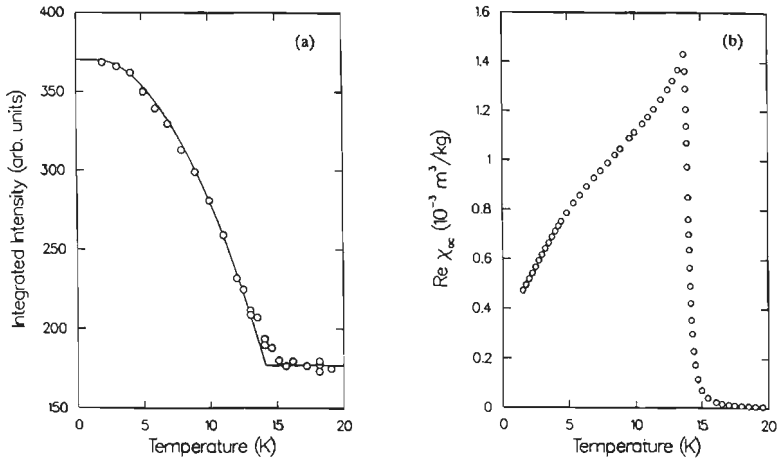


Figure 3.6: $\text{Sn}_{0.90}\text{Mn}_{0.10}\text{Te}$, $p = 14 \times 10^{20} \text{ cm}^{-3}$.

a: Temperature dependence of the integrated (111) intensity, triple-axis mode. Full curve: mean-field approximation for $S = 5/2$ and $T_c = 14.2 \text{ K}$, scaled along the intensity axis to obtain quantitative agreement with the data.

b: Real component of the ac susceptibility versus temperature.

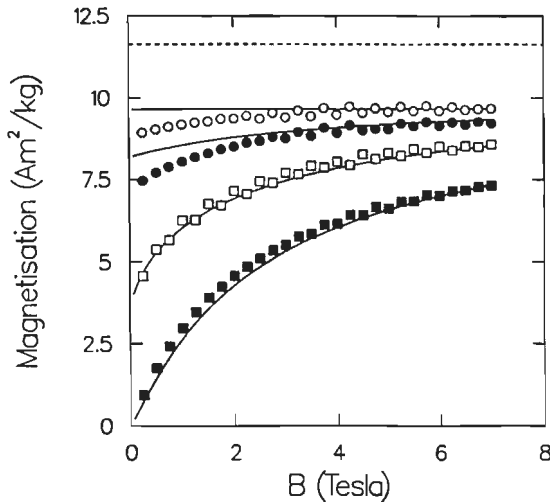


Figure 3.7: $\text{Sn}_{0.90}\text{Mn}_{0.10}\text{Te}$, $p = 14 \times 10^{20} \text{ cm}^{-3}$. Magnetisation as a function of the magnetic field at $T = 2.0 \text{ K}$ (\circ), $T = 8.5 \text{ K}$ (\bullet), $T = 14.0 \text{ K}$ (\square), and $T = 20.0 \text{ K}$ (\blacksquare). Full curves: mean-field approximations for $S = 5/2$, $T_c = 14.2 \text{ K}$, and $x = 0.082$. Dashed line: theoretical saturation magnetisation for $x = 0.10$ and $S = 5/2$.

a value of (0.79 ± 0.02) of the theoretical saturation value. This may partially be due to an actual Mn concentration below the nominal $x = 0.10$, as indicated by the values in Table 3.1, but the reduction is too large to be ascribed to a reduced Mn concentration alone. High-field magnetisation measurements, presented in Fig. 3.7, confirm this reduction of the magnetisation. Only about 82 % of the expected saturation magnetisation (dashed line) for $x = 0.10$ and $S = 5/2$ is observed, in good agreement with the neutron diffraction data. The solid curves are mean-field approximations with $x = 0.082$ and are in fair agreement with the data. In the next section we will come back to this reduced magnetisation.

Concluding, we state that the low-temperature magnetic phase of this sample is a long-range ordered ferromagnetic phase, albeit with a reduced magnetisation. This ferromagnetic ordering is in agreement with the phase diagram in Fig. 1.8.

3.3 Discussion

The results of the neutron diffraction experiments, combined with those of measurements of the ac susceptibility and the magnetic specific heat, lead to the conclusion that the low-temperature magnetic phase in the studied as-grown, $p > p_c$, $\text{Sn}_{1-x}\text{Mn}_x\text{Te}$ crystals is a long-range ordered ferromagnetic phase. The experimentally determined values for T_c and Θ suggest a linear dependence of these parameters on the Mn concentration (see Table 3.1). As far as Θ is concerned this is in agreement with the RKKY model used for the description of the carrier-concentration-induced ferromagnetism in section 1.3. For the present combinations of Mn concentrations and charge carrier concentrations no indications for the existence of a (reentrant) spin-glass phase were found, in contradiction to the magnetic phase diagram reported by Mauger and Escorne² (Fig. 1.8). In the samples with $x = 0.06$ and $x = 0.10$ the saturation magnetisation, both that determined from the neutron diffraction experiments and that inferred from high-field magnetisation measurements, was below the value expected for the nominal Mn concentrations and $S = 5/2$. The saturation magnetisation is determined by the product of the Landé factor g , the number of magnetic ions, and the spin S of each ion. Electron spin resonance on ferromagnetic samples of the related compound $\text{Pb}_{1-x}\text{Sn}_y\text{Mn}_x\text{Te}$, with $x \leq 0.04$, yielded no indications for deviations from $g = 2$.⁷ An obvious explanation for the reduction of the observed saturation magnetisation would be that the actual Mn concentrations are below the nominal values. To explain the reduction observed in the high-field magnetisation measurements Mn concentrations of $x = 0.052$ and $x = 0.082$, respectively, would be required. However, the experimentally determined values, listed in Table 3.1, exclude this possibility. The second possible explanation is found in a reduction of the moment of each individual Mn ion to $4.25 \mu_B$ in the $x = 0.06$ sample and to $4.10 \mu_B$ in the $x = 0.10$ sample. The results from the high-temperature susceptibility and especially those from the high-temperature magnetisation measurements also exclude this possibility. We like to note that in the latter case the magnetisation was measured between 20 K and 200 K with the same equipment as the low-temperature high-field

measurements in Figs. 3.4 and 3.7. The Mn concentrations listed in Table 3.1 were determined from Curie-Weiss fits to these data substituting $S = 5/2$ and $g = 2$. If the moment of each Mn ion would have been reduced to the aforementioned values a calculation with $S = 5/2$ and $g = 2$ would have led to unrealistic Mn concentrations of, respectively, $x = 0.078$ and $x = 0.140$. The fact that with $S = 5/2$ Mn concentrations approximately equal to the nominal values result, indicate that the moment of each individual Mn ion is not reduced, at least not in the paramagnetic temperature range. Other explanations were put forward by Escorne *et al.*⁸, who reported reduced saturation magnetisations for as-grown $\text{Sn}_{1-x}\text{Mn}_x\text{Te}$ samples with $x = 0.03$ ($4.6 \mu_B$ per Mn ion) and $x = 0.077$ ($3.8 \mu_B$ per Mn ion). Because of the observed decrease of the magnetisation per Mn ion with increasing x , they suggested that the reduction of the magnetisation might be caused by the presence of Mn-Mn pairs coupled by short-range antiferromagnetic interactions. This explanation implies that not all Mn ions take part in the low-temperature ferromagnetic ordering, but groups of antiferromagnetically coupled Mn ions persist down to $T = 0$ K. In the present data the trend of a reduction of the moment per Mn ion with increasing x is confirmed if the value from the neutron diffraction experiments on the $x = 0.03$ sample is compared to the data for $x = 0.06$ and $x = 0.10$, but not by the comparison between the latter two compositions. The other possible cause of the reduction of the saturation magnetisation suggested by Escorne *et al.*⁸ was a canting of the Mn spins, comparable to what is observed in a canted ferromagnet, such as for example AuFe with 19 % Fe⁹. This canting can be considered as a slight random deviation of the spins with respect to the direction of the ferromagnetic alignment. In this explanation all Mn ions take part in the ferromagnetic ordering, but they maintain a component that is not ferromagnetically aligned, causing the reduction of the saturation magnetisation. For AuFe with 19 % Fe this mechanism was deduced from Mössbauer experiments⁹, which showed that the canting process started at a canting temperature significantly below the transition temperature to the ferromagnetic phase and that the degree of canting increased continuously with decreasing temperature. Above the canting temperature the behaviour was essentially ferromagnetic, below it the ferromagnetic structure was broken down gradually. This latter behaviour is in agreement with previous results of Coles *et al.*¹⁰, who reported that AuFe with 19 % Fe is a reentrant spin glass. This reentrant spin-glass character was for example reflected in the results of susceptibility measurements. Because for the present $\text{Sn}_{1-x}\text{Mn}_x\text{Te}$ samples no indications for reentrant spin-glass behaviour were found in the temperature range covered in the experiments discussed in section 3.2, the hypothesis of a canting of the Mn spins does not seem to apply for these samples. Summarizing, on basis of the present data no conclusion can be drawn with respect to the appropriate explanation for the observed reduction of the saturation magnetisation in the samples with ($x = 0.06$, $p = 11 \times 10^{20} \text{ cm}^{-3}$) and ($x = 0.10$, $p = 14 \times 10^{20} \text{ cm}^{-3}$). In chapter 5, where more data for other combinations of x and p will be available, we will come back to the subject of the missing magnetisation.

References

1. W.J.M. de Jonge, H.J.M Swagten, S.J.E.A. Eltink, and N.M.J. Stoffels, *Semicond. Sci. Technol.* **5**, S131 (1990).
2. A. Mauger and M. Escorne, *Phys. Rev. B* **35**, 1902 (1987).
3. H. Maletta and P. Convert, *Phys. Rev. Lett.* **42**, 108 (1979).
4. A.J. Henderson Jr., G.R. Brown, T.B. Reed, and H. Meyer, *J. Appl. Phys.* **41**, 946 (1970).
5. D.L. Martin, *Phys. Rev. B* **20**, 368 (1979).
6. B.M. Boerstael, J.J. Zwart, and J. Hansen, *Physica* **57**, 397 (1972).
7. T. Story, P.J.T. Eggenkamp, C.H.W. Swüste, H.J.M. Swagten, W.J.M. de Jonge, and A. Szczerbakow, *Phys. Rev. B* **47**, 227 (1993).
8. M. Escorne, M. Godinho, J.L. Tholence, and A. Mauger, *J. Appl. Phys.* **57**, 3424 (1985).
9. F. Varret, A. Hamzic, and I.A. Campbell, *Phys. Rev. B* **26**, 5285 (1982).
10. B.R. Coles, B.V.B. Sarkissian, and R.H. Taylor, *Philos. Mag. B* **37**, 489 (1978).

Chapter 4

Carrier-concentration-induced ferromagnet to spin-glass transition in $\text{Sn}_{0.96}\text{Mn}_{0.04}\text{Te}$

4.1 Introduction

In the preceding chapter the characterisation of the low-temperature magnetic phase in as-grown, $p > p_c$, $\text{Sn}_{1-x}\text{Mn}_x\text{Te}$ crystals was described. In this chapter we will focus on the second aim of the present work: the extension of the magnetic (T, x, p) phase diagram, especially towards higher charge carrier concentrations. De Jonge *et al.*¹ reported preliminary measurements on samples of $\text{Sn}_{0.97}\text{Mn}_{0.03}\text{Te}$ with $p = 5.3 \times 10^{20} \text{ cm}^{-3}$ and $p = 23 \times 10^{20} \text{ cm}^{-3}$. Their results are reproduced in Fig. 4.1. For the sample with the lower carrier concentration ferromagnetic features were observed, in agreement with the data for the $x = 0.03$ sample with $p = 7.0 \times 10^{20} \text{ cm}^{-3}$, displayed in Fig. 3.1. The data for the sample with $p = 23 \times 10^{20} \text{ cm}^{-3}$, on the contrary, indicated that for this carrier

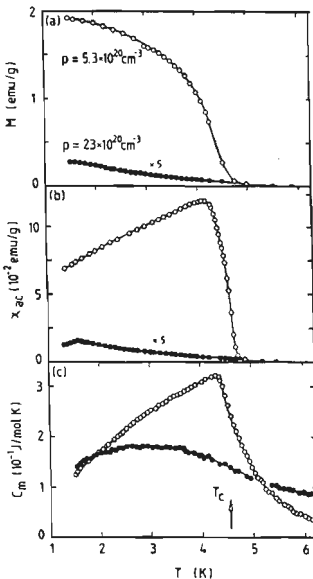


Figure 4.1: $\text{Sn}_{0.97}\text{Mn}_{0.03}\text{Te}$ with $p = 5.3 \times 10^{20} \text{ cm}^{-3}$ (open circles) and $p = 23 \times 10^{20} \text{ cm}^{-3}$ (closed circles) (a) Field-cooled magnetisation ($B = 0.2 \text{ mT}$), (b) ac susceptibility, and (c) magnetic specific heat Reproduced from Ref. 1.

treatment	p (10^{20} cm^{-3})	x (%) (EPMA)	x (%) (H.T. χ)	Θ (K) (H.T. χ)
Sn annealed	7.4 ± 0.3		4.4 ± 0.1	7.1 ± 0.1
as-grown	11.4 ± 0.3	4.0	4.0 ± 0.1	7.2 ± 0.1
$\text{Sn}_{0.47}\text{Te}_{0.53}$ annealed	23 ± 1		4.1 ± 0.1	7.0 ± 0.1

Table 4.1: Properties of the samples used in the experiments described in this chapter. The Mn concentrations x are expressed in % Mn. Charge carrier concentrations were measured at 77 K. Θ (H.T. χ) and x (H.T. χ) were determined from the high temperature susceptibility measurements described in section 4.2.1. Except for the as-grown $p = 11 \times 10^{20} \text{ cm}^{-3}$ sample, the same samples were used for the neutron scattering experiments.

concentration the ferromagnetically ordered phase had changed into a spin-glass-like phase. This was the first observation of a breakdown of a ferromagnetically ordered state induced by an increase of the charge carrier concentration, illustrating the decisive role of the charge carrier concentration in the magnetic (T,x,p) phase diagram of $\text{Sn}_{1-x}\text{Mn}_x\text{Te}$. In this chapter the evolution of the magnetic correlations with increasing carrier concentration will be studied for $\text{Sn}_{0.96}\text{Mn}_{0.04}\text{Te}$ by means of experiments on samples with $p = 7, 11,$ and $23 \times 10^{20} \text{ cm}^{-3}$. In section 4.2 the results of measurements of the ac susceptibility (including the frequency dependence), the magnetisation (both low- and high-field measurements), and the magnetic specific heat will be presented. Subsequently, the results of single-crystal neutron diffraction experiments will be presented in section 4.3. In the last section the results will be discussed briefly.

All samples used in the measurements described in this chapter were taken from the same Bridgman batch. Carrier concentrations $p = 7 \times 10^{20} \text{ cm}^{-3}$ and $p = 23 \times 10^{20} \text{ cm}^{-3}$ were achieved by annealing as-grown samples according to the recipes described in section 2.2. In Table 4.1 the carrier concentrations and Mn concentrations, determined from high-temperature susceptibility measurements, are listed. For the as-grown sample the composition was double checked with electron probe micro analysis, yielding a perfect agreement with the nominal Mn concentration.

4.2 Results of the ac susceptibility, magnetisation, and magnetic specific heat experiments

4.2.1 ac susceptibility

The ac susceptibility has been measured using a mutual inductance bridge. The standard frequency of the 1.6 μT driving ac field was 913 Hz. For all three samples the minimum temperature in the measurements was 1.3 K, whereas the maximum temperature was

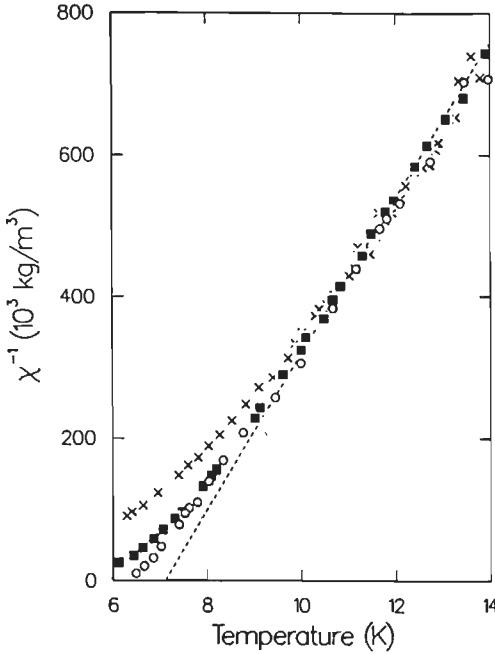


Figure 4.2: Temperature dependence of the reciprocal real part of the susceptibility of $\text{Sn}_{0.96}\text{Mn}_{0.04}\text{Te}$ with $p = 7 \times 10^{20} \text{ cm}^{-3}$ (\circ), $p = 11 \times 10^{20} \text{ cm}^{-3}$ (\blacksquare), and $p = 23 \times 10^{20} \text{ cm}^{-3}$ (\times). Dashed line: Curie-Weiss fit to the data for the sample with $p = 11 \times 10^{20} \text{ cm}^{-3}$. Driving ac field: $1.6 \mu\text{T}$, 913 Hz.

50 K for the sample with $p = 7 \times 10^{20} \text{ cm}^{-3}$, 25 K for $p = 11 \times 10^{20} \text{ cm}^{-3}$, and 20 K for $p = 23 \times 10^{20} \text{ cm}^{-3}$. In Fig. 4.2 the inverse of the real part of the susceptibility in the temperature range from $T = 6 \text{ K}$ to $T = 14 \text{ K}$ is displayed for the three samples. In all cases the data for $T > 10 \text{ K}$ have been fitted to a Curie-Weiss law, yielding the Curie-Weiss temperatures Θ and the Mn-concentrations x listed in Table 4.1. In the fits the values $S = 5/2$ and $g = 2$ were used. As an illustration the resulting line for the sample with $p = 11 \times 10^{20} \text{ cm}^{-3}$ is included in Fig. 4.2. All samples have a Curie-Weiss temperature of approximately 7 K. This positive value of Θ indicates that the sum of the exchange interactions, ΣJ_{ij} , is ferromagnetic. When the carrier concentration increases, deviations from Curie-Weiss behaviour occur at higher temperatures: for the sample with $p = 23 \times 10^{20} \text{ cm}^{-3}$ deviations start at circa 11 K, for $p = 11 \times 10^{20} \text{ cm}^{-3}$ at 9 K, whereas in the $p = 7 \times 10^{20} \text{ cm}^{-3}$ sample Curie-Weiss behaviour is maintained until just above $T = \Theta$.

Figures 4.3a and 4.3b respectively show the real (χ') and imaginary (χ'') part of the ac susceptibility in the low-temperature region for all three samples. The data for the sample with $p = 7 \times 10^{20} \text{ cm}^{-3}$ show the characteristic features of a ferromagnetic transition, just like the samples discussed in chapter 3. First, there is a sharp transition in both χ' and χ'' with a critical or Curie-temperature $T_c \approx 6.3 \text{ K}$, which is approximately equal to the

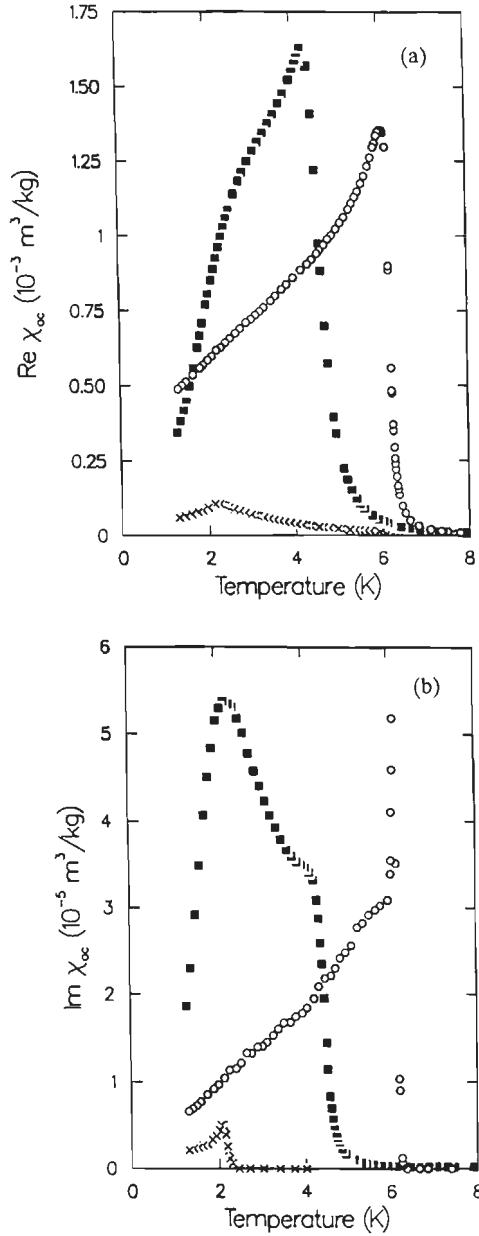


Figure 4.3: Temperature dependence of (a) the real and (b) the imaginary component of the ac susceptibility of $\text{Sn}_{0.96}\text{Mn}_{0.04}\text{Te}$ samples with $p = 7 \times 10^{20} \text{ cm}^{-3}$ (\circ), $p = 11 \times 10^{20} \text{ cm}^{-3}$ (\blacksquare), and $p = 23 \times 10^{20} \text{ cm}^{-3}$ (\times). Driving ac field: $1.6 \mu\text{T}$, 913 Hz.

Curie-Weiss temperature Θ , and, second, the maximum value of χ' is of the order of $1/N$, where N is the demagnetising factor of the sample.

For the as-grown sample, with $p = 11 \times 10^{20} \text{ cm}^{-3}$, the real part of the susceptibility shows a gradual increase below 6.5 K, smoothly transforming into a steep rise towards a maximum at 4.3 K. The imaginary part displays a shoulder around this temperature, but continues to increase until a maximum is reached at 2.3 K. In the real component a change of slope is seen around the same temperature. A similar behaviour has been reported for a diversity of reentrant spin-glass systems, such as $\text{Eu}_x\text{Sr}_{1-x}\text{S}^2$, $(\text{Pd}_{0.9965}\text{Fe}_{0.0035})_{1-x}\text{Mn}_x^3$, NiMn^4 , and a number of amorphous Fe-Mn and Fe-Ni alloys.⁵ In these systems the sharp increase of χ' is interpreted as a transition to a ferromagnetically ordered phase, followed by a second transition to a spin-glass phase at a lower temperature, denoted by the maximum of χ'' . The higher maximum in χ' for the sample with $p = 11 \times 10^{20} \text{ cm}^{-3}$ compared to that with $p = 7 \times 10^{20} \text{ cm}^{-3}$ is probably related to the different shape of the samples.

The real component of the ac susceptibility of the $p = 23 \times 10^{20}$ sample shows a cusp-like maximum at 2.2 K, i.e. far below the Curie-Weiss temperature $\Theta = 7.0 \text{ K}$, accompanied by a somewhat steeper increase of the imaginary part at the same temperature. The height of the maximum of χ' does not exceed 10 % of the demagnetising limit. Both the height and the shape of the maximum of χ' indicate that the sample undergoes a transition to a spin-glass state at the freezing temperature $T_f \approx 2.2 \text{ K}$.⁶ The aforementioned deviations from Curie-Weiss behaviour at temperatures as high as $5 T_f$ (see Fig. 4.2), that were also reported⁷ for the canonical spin glass CuMn , support this conclusion. Concerning the values of T_f and Θ , it must be noted that $T_f < \Theta$, in contrast to the metallic RKKY spin glasses⁸, for which $\Theta \ll T_f$, but in agreement with the observations for the insulating spin glass $\text{Eu}_x\text{Sr}_{1-x}\text{S}$ with $x \leq 0.40$, where $\Theta \approx 4T_f$.⁹

The frequency dependence of the ac susceptibility was studied for frequencies between 9.13 Hz and 9130 Hz. For $p = 7 \times 10^{20} \text{ cm}^{-3}$ no significant dependence on the frequency was observed, in agreement with what might be expected for a ferromagnet.¹⁰ The results for the samples with $p = 23 \times 10^{20} \text{ cm}^{-3}$ and $p = 11 \times 10^{20} \text{ cm}^{-3}$ are presented in Figs. 4.4 and 4.5, respectively. In the former case the maximum of both the real and the imaginary component shifts towards higher temperature with increasing frequency. For the maximum of χ' this shift is accompanied by a decrease in absolute value (Fig. 4.4a). For χ'' no clear tendency in the absolute value of the maximum can be detected because of the inaccuracy in the raw data for lower frequencies (the measured χ'' signal is proportional to the measurement frequency). The phenomenon of a frequency dependent freezing temperature is also observed in CuMn ¹¹ and is generally considered to be a characteristic feature of spin glasses.¹² This dependence can be characterised by the quantity $R = \Delta T_f / (T_f \Delta \log \nu)$, the relative shift of T_f per decade of frequency (ν). In this case $R = 0.027$, which is of the same order of magnitude ($0.005 < R < 0.11$) that is generally observed for spin-glass systems.¹³

For $p = 11 \times 10^{20} \text{ cm}^{-3}$ the aforementioned change of slope in χ' at about 2.5 K shifts towards higher temperatures with increasing frequency, accompanied by a decrease in the absolute value (Fig. 4.5a). This behaviour suggests that also at this carrier concentration a transition to a spin-glass like state occurs at low temperatures. The

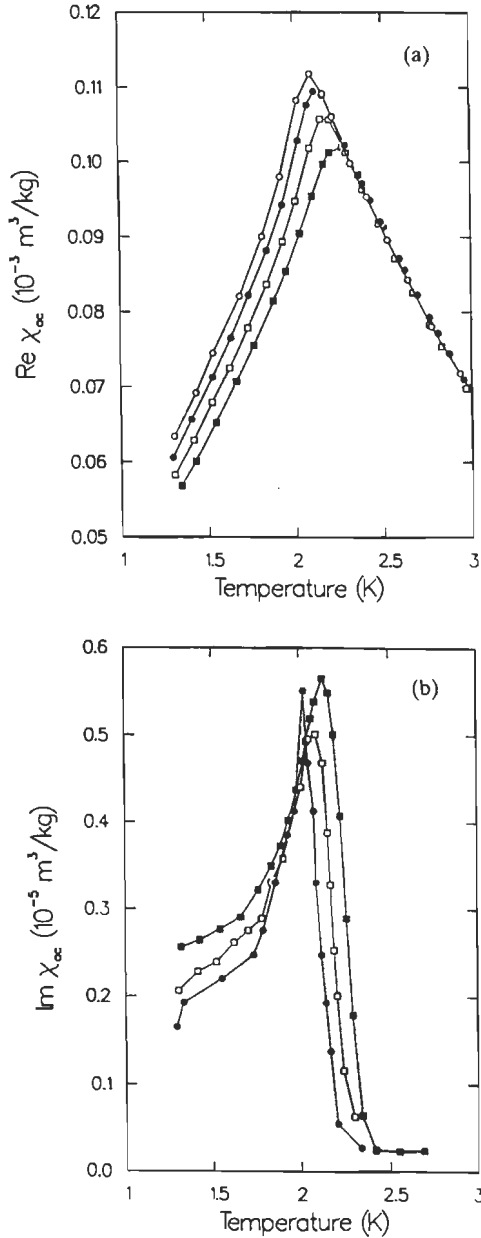


Figure 4.4: $\text{Sn}_{0.96}\text{Mn}_{0.04}\text{Te}$, $p = 23 \times 10^{20} \text{ cm}^{-3}$: temperature dependence of (a) the real and (b) the imaginary component of the ac susceptibility at frequencies of 9.13 Hz (\circ), 91.3 Hz (\bullet), 913 Hz (\square), and 9130 Hz (\blacksquare). The χ'' signal at 9.13 Hz was too small to be detected. Lines are guides to the eye.

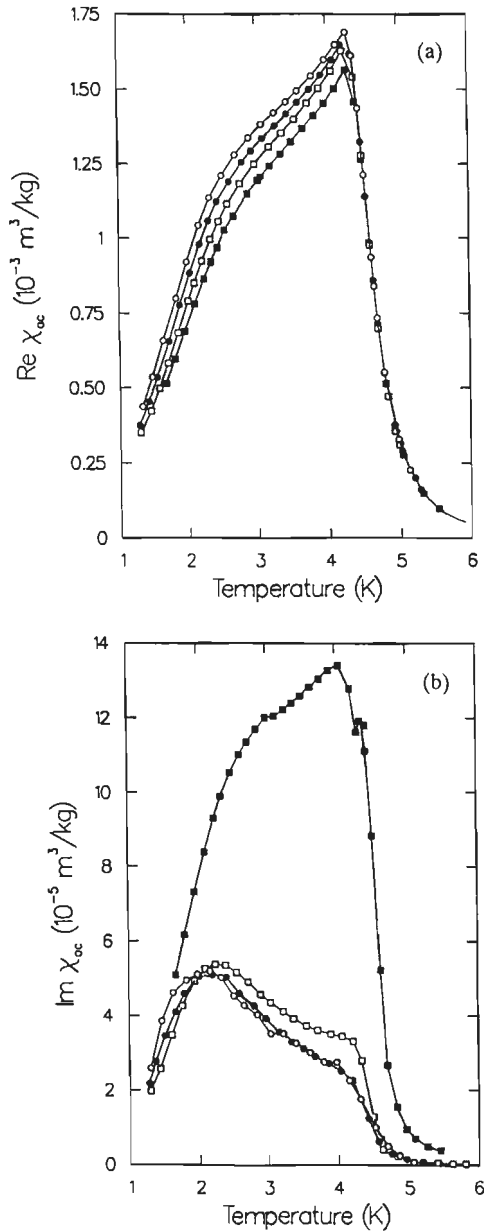


Figure 4.5: $\text{Sn}_{0.96}\text{Mn}_{0.04}\text{Te}$, $p = 11 \times 10^{20} \text{ cm}^{-3}$: temperature dependence of (a) the real and (b) the imaginary component of the ac susceptibility at frequencies of 9.13 Hz (\circ), 91.3 Hz (\bullet), 913 Hz (\square), and 9130 Hz (\blacksquare). Lines are guides to the eye.

imaginary component (Fig. 4.5b) shows a quite peculiar tendency with increasing frequency. For the lower three frequencies the maximum tends to move to higher temperatures as the frequency increases. At the highest frequency, however, the shape of the χ'' curve has changed drastically and resembles that of the χ' curves plotted in Fig. 4.5a. The shoulder occurring at about 4 K at lower frequencies has split into two maxima at 9130 Hz, whereas the maximum near 2.3 K at lower frequencies has developed into a shoulder. Besides the change in the shape of the curve, there is also a remarkable increase of the absolute value of χ'' and hence of the energy absorbed by the sample from the ac field. The origin of this behaviour is not yet clear. Measurements at other frequencies, both between 913 and 9130 Hz and above 9130 Hz, are necessary to study the evolution of χ'' with frequency in more detail.

4.2.2 Magnetisation

We measured the field-cooled magnetisation of the same three samples in a 2.0 mT field, using a standard vibrating sample magnetometer. The results are shown in Fig. 4.6. The magnetisation of the sample with $p = 7 \times 10^{20} \text{ cm}^{-3}$ rises sharply at 6.3 K, the same temperature where the ac susceptibility has its maximum slope. The shape of the curve confirms the ferromagnetic nature of the phase transition suggested by the susceptibility measurements. In the sample with $p = 23 \times 10^{20} \text{ cm}^{-3}$ the magnetisation increases more gradually with decreasing temperature and its magnitude is strongly suppressed. Of course, this behaviour does not prove the existence of a spin-glass state, but it certainly reveals the collapse of the ferromagnetic state that is observed for $p = 7 \times 10^{20} \text{ cm}^{-3}$. The magnetisation of the sample with $p = 11 \times 10^{20} \text{ cm}^{-3}$ displays a temperature dependence which is neither ferromagnetic nor spin-glass like. Below 6 K the magnetisation increases, but less sharp than for $p = 7 \times 10^{20} \text{ cm}^{-3}$. With further decreasing temperature the magnetisation continues to increase, until a broad maximum is reached near 2.35 K, approximately the same temperature at which the imaginary part of the susceptibility has its maximum at frequencies up to 913 Hz (2.3 ± 0.1 K). Below this temperature the magnetisation decreases. A similar behaviour of the field-cooled magnetisation has previously been reported¹⁴ for the magnetic alloys FeAl, CrFe and AuFe in the reentrant spin-glass concentration range.

With the same vibrating sample magnetometer also high-field magnetisation measurements were performed on the same samples with $p = 7 \times 10^{20} \text{ cm}^{-3}$, $p = 11 \times 10^{20} \text{ cm}^{-3}$, and $p = 23 \times 10^{20} \text{ cm}^{-3}$. For each carrier concentration the magnetisation was measured as a function of the magnetic field between 0 T and 6 T at temperatures between 1.9 and 6.0 K. In Fig. 4.7 the data at $T = 1.9$ K are presented. The differences between the results for the three carrier concentrations are most pronounced at low fields. The rate at which the magnetisation at the lowest fields increases with field decreases with increasing carrier concentration, confirming the deterioration of the ferromagnetic order with increasing carrier concentration. At the other temperatures the same trend was observed. For fields above $B = 1$ T some care must be taken in the interpretation of the data, because the raw data for the samples with $p = 7 \times 10^{20} \text{ cm}^{-3}$ and $p = 23 \times 10^{20} \text{ cm}^{-3}$ had to be corrected

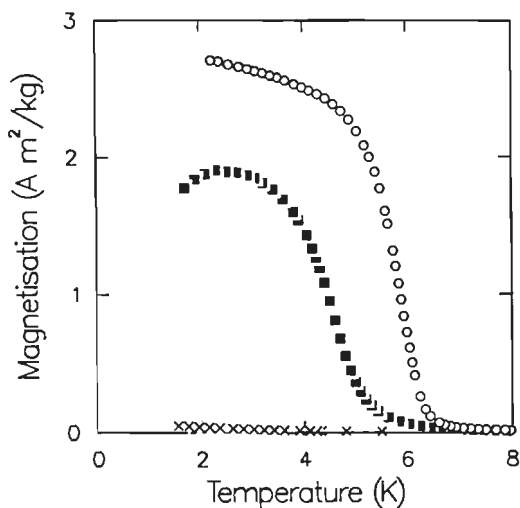


Figure 4.6: Temperature dependence of the field-cooled magnetisation of $\text{Sn}_{0.96}\text{Mn}_{0.04}\text{Te}$ with $p = 7 \times 10^{20} \text{ cm}^{-3}$ (\circ), $p = 11 \times 10^{20} \text{ cm}^{-3}$ (\blacksquare), and $p = 23 \times 10^{20} \text{ cm}^{-3}$ (\times). $B = 2.0 \text{ mT}$.

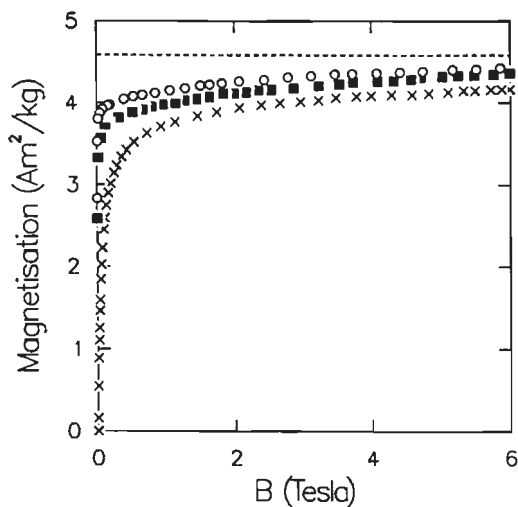


Figure 4.7: Magnetisation versus magnetic field at $T = 1.9 \text{ K}$ for $\text{Sn}_{0.96}\text{Mn}_{0.04}\text{Te}$ samples with $p = 7 \times 10^{20} \text{ cm}^{-3}$ (\circ), $p = 11 \times 10^{20} \text{ cm}^{-3}$ (\blacksquare), and $p = 23 \times 10^{20} \text{ cm}^{-3}$ (\times). Dashed line: theoretical saturation magnetisation for $x = 0.04$ and $S = 5/2$.

for a diamagnetic contribution from the sample holder. This correction causes a relatively large inaccuracy (ca. 4 % at 6 T) in the magnetisation values. Because of this correction it is hard to judge whether the magnetisation actually saturates in fields up to $B = 6$ T for the individual samples. The maximal observed magnetisation for the sample with $p = 7 \times 10^{20} \text{ cm}^{-3}$ amounts to (97 ± 4) % of the theoretical saturation value for $x = 0.04$, $S = 5/2$, and $g = 2$, indicated by the dashed line in Fig. 4.7. For the $p = 11 \times 10^{20} \text{ cm}^{-3}$ and $p = 23 \times 10^{20} \text{ cm}^{-3}$ samples the maximal observed magnetisation amounts to respectively (95 ± 1) % and (91 ± 4) % of the theoretical saturation value. In all cases this is significantly closer to saturation than for the ferromagnetic samples with $x = 0.06$, $p = 11 \times 10^{20} \text{ cm}^{-3}$ and with $x = 0.10$, $p = 14 \times 10^{20} \text{ cm}^{-3}$, discussed in chapter 3, in spite of the non-ferromagnetic character of the low-temperature state in the present $x = 0.04$ samples with $p = 11 \times 10^{20} \text{ cm}^{-3}$ and $23 \times 10^{20} \text{ cm}^{-3}$.

4.2.3 Specific heat

In Fig. 4.8a the magnetic specific heat, measured with a heat pulse calorimeter, is displayed for samples with $p = 7 \times 10^{20} \text{ cm}^{-3}$, $p = 11 \times 10^{20} \text{ cm}^{-3}$, and $p = 23 \times 10^{20} \text{ cm}^{-3}$. The magnetic part of the specific heat was obtained by subtracting the lattice specific heat, i.e. the measured specific heat of the host material SnTe, from the raw $\text{Sn}_{1-x}\text{Mn}_x\text{Te}$ data. For the $p = 7 \times 10^{20} \text{ cm}^{-3}$ sample a lambda anomaly, characteristic for a second-order transition, is observed at the critical temperature. With increasing charge carrier concentration this anomaly gradually transforms into a broad maximum for the sample with $p = 23 \times 10^{20} \text{ cm}^{-3}$. The curve for the sample with $p = 11 \times 10^{20} \text{ cm}^{-3}$ still has a distinct maximum near the temperature at which the real part of the susceptibility has a maximum, but for $p = 23 \times 10^{20} \text{ cm}^{-3}$ no special feature is observed at the freezing temperature $T_f = 2.2$ K, at which the cusp in the ac susceptibility occurs. Such a smooth temperature dependence of the magnetic specific heat, without a distinct anomaly at T_f , is also observed for archetypical spin glasses like CuMn .¹⁵

Another indication for the existence of a spin-glass state at low temperatures for this range of carrier concentrations and Mn concentrations is found in magnetic specific heat measurements on $\text{Sn}_{1-x}\text{Mn}_x\text{Te}$ with $x = 0.03$ and $p = 23 \times 10^{20} \text{ cm}^{-3}$, the results of which are presented in Fig. 4.8b. The data for temperatures above 1.5 K were already included in Fig. 4.1.¹ They display a qualitatively similar behaviour as those on the 4 % Mn sample with $p = 23 \times 10^{20} \text{ cm}^{-3}$ in Fig. 4.8a. The data in the temperature range from 1.5 K down to 0.2 K, which have been corrected for the nuclear hyperfine contribution of the Mn ions (cf. section 3.2.1), were recently obtained. They show an approximately linear temperature dependence of the magnetic specific heat, extrapolating to an intersection of the temperature axis at 0.17 ± 0.02 K. This positive intersection as well as the linear temperature dependence are considered to be typical spin-glass features.¹⁶ For the lowest temperatures C_m deviates from the linear behaviour and approaches $T = 0$ K with a smaller slope, in agreement with the results of Martin on canonical spin glasses.¹⁷

An analysis of the magnetic entropy shows that for the samples with $p = 7 \times 10^{20} \text{ cm}^{-3}$

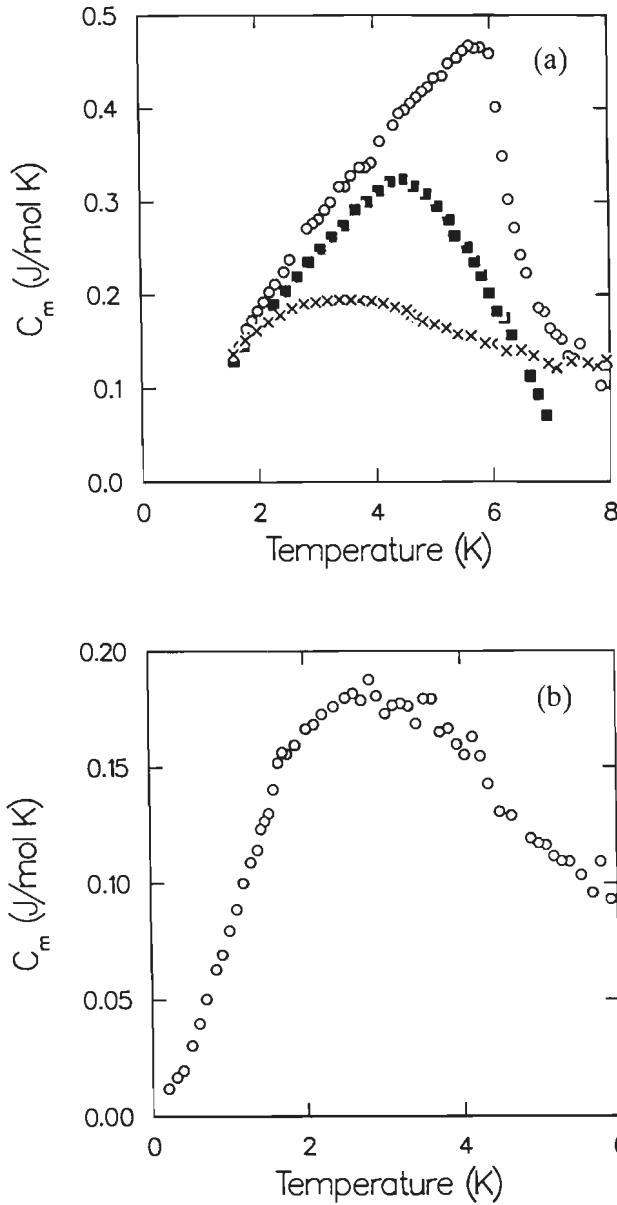


Figure 4.8: Temperature dependence of the magnetic specific heat of (a) $\text{Sn}_{0.96}\text{Mn}_{0.04}\text{Te}$ with $p = 7 \times 10^{20} \text{ cm}^{-3}$ (O), $p = 11 \times 10^{20} \text{ cm}^{-3}$ (■), and $p = 23 \times 10^{20} \text{ cm}^{-3}$ (x), and (b) of $\text{Sn}_{0.97}\text{Mn}_{0.03}\text{Te}$ with $p = 23 \times 10^{20} \text{ cm}^{-3}$.

and $p = 23 \times 10^{20} \text{ cm}^{-3}$ the total magnetic entropy S_m that is recovered in the temperature range up to 10 K, is approximately equal to the theoretical value $S_m = xR \ln(2S + 1)$, with $x = 0.04$ and $S = 5/2$. In the sample with $p = 11 \times 10^{20} \text{ cm}^{-3}$ the experimentally observed entropy could not be determined, because no reliable data are available for $T > 7 \text{ K}$. When the entropy recovered below the temperatures at which the real component of the susceptibility shows a maximum is compared to the total theoretical entropy, it appears that 83 % is gained below 6.1 K in the sample with $p = 7 \times 10^{20} \text{ cm}^{-3}$, in excellent agreement with the theoretical value for a 3d fcc Heisenberg ferromagnet¹⁸, which is 83 %. In the $p = 23 \times 10^{20} \text{ cm}^{-3}$ sample only about 35 % of the theoretical entropy is recovered below 2.2 K. This latter result is in good agreement with that of Wenger and Keesom¹⁹ for the spin glass CuMn .

4.2.4 Provisional conclusions

The results of the measurements of the ac susceptibility, the magnetisation, and the magnetic specific heat on the $\text{Sn}_{0.96}\text{Mn}_{0.04}\text{Te}$ samples with $p = 7, 11,$ and $23 \times 10^{20} \text{ cm}^{-3}$ strongly suggest a charge-carrier-concentration-induced breakdown of a ferromagnetic state to a spin-glass state. For the sample with the lowest carrier concentration a transition to a ferromagnetically ordered state at $T_c = 6.3 \text{ K}$ is indicated by the sharp increase in the susceptibility, the behaviour of the spontaneous magnetisation deduced from the low-field magnetisation measurements, and the lambda anomaly in the specific heat. For the intermediate carrier concentration $p = 11 \times 10^{20} \text{ cm}^{-3}$ the results suggest the existence of a reentrant spin-glass phase. With lowering temperature initially a transition to a ferromagnetic state occurs at 4.5 K, indicated by the increase of both the real part of the ac susceptibility and the spontaneous magnetisation. A second transition, to a spin-glass phase, takes place at 2.3 K, signalled by the maximum in the imaginary part of the ac susceptibility and the decrease of the spontaneous magnetisation. The data for the sample with $p = 23 \times 10^{20} \text{ cm}^{-3}$ strongly suggest a transition to a spin-glass state at a freezing temperature $T_f = 2.2 \text{ K}$, identified by the cusp in the ac susceptibility, in combination with the absence of a spontaneous magnetisation, and the smooth temperature dependence of the specific heat. The observed frequency dependence of the ac susceptibility of the samples with $p = 11 \times 10^{20} \text{ cm}^{-3}$ and $p = 23 \times 10^{20} \text{ cm}^{-3}$ is also an indication for the presence of a spin-glass-like phase at low temperatures for these carrier concentrations. Although strongly suggestive, most of the evidence presented above is somewhat circumstantial. To obtain more direct information on the conjectured collapse of the ferromagnetic state with increasing charge carrier concentration, neutron scattering experiments were performed. With the aid of neutron diffraction it is not only possible to gain insight in the *nature* of the magnetic ordering, but also in the *range* of the magnetic correlations. For each carrier concentration these correlations were monitored as a function of temperature. The details of this study will be discussed extensively in the next section.

4.3 Neutron diffraction

4.3.1 Introduction

As was already described in section 3.1, in neutron diffraction experiments ferromagnetic ordering will result in magnetic Bragg-scattering superimposed on the nuclear Bragg-reflections below the transition temperature T_c . For a reentrant spin glass the ferromagnetic ordering will also result in increasing Bragg-scattering with decreasing temperature, until the transition temperature to the spin-glass state is reached, below which the intensity of the magnetic Bragg reflection will decrease.^{2,19} In the case of an ideal spin-glass state the spins are frozen in random directions, so no increase of the Bragg-intensity will be observed below the freezing temperature T_f . All neutron diffraction experiments were performed on $\text{Sn}_{0.96}\text{Mn}_{0.04}\text{Te}$ single crystals. Except for the as-grown, $p = 11 \times 10^{20} \text{ cm}^{-3}$ crystal, the samples were the same ones that were used in the measurements of the susceptibility and the magnetisation. The $p = 11 \times 10^{20} \text{ cm}^{-3}$ crystal was from the same Bridgman-batch as the other crystals and identical in composition to the sample used for the susceptibility and magnetisation measurements. The experiments were performed on the HB3 triple-axis spectrometer at the HFR Petten. For all samples the profile of the (111) reflection along the [110] direction was studied as a function of temperature. Measurements were performed both with and without the analyser. With a pair of external Helmholtz-coils a magnetic field up to 5.0 mT could be applied perpendicular to the horizontal scattering plane. The lowest temperature that could be reached in the experiments was approximately 1.7 K.

4.3.2 Results for $\text{Sn}_{0.96}\text{Mn}_{0.04}\text{Te}$ with $p = 7 \times 10^{20} \text{ cm}^{-3}$

For the Sn-annealed $p = 7 \times 10^{20} \text{ cm}^{-3}$ sample the integrated intensity of Gauss-fits to the (111) profile, observed in triple-axis configuration with the analyser set at zero energy transfer, is presented as a function of temperature in Fig. 4.9. The variation of the intensity with temperature in double-axis mode is qualitatively similar. In agreement with the results of the ac susceptibility, the magnetisation, and the magnetic specific heat, the diffraction data indicate a transition to a ferromagnetically ordered phase with a transition temperature $T_c = 6.2 \pm 0.1 \text{ K}$. Below T_c the magnetic intensity is superposed on the temperature independent nuclear (111) and second order (222) intensity. The full curve in Fig. 4.9 represents the result of a mean-field calculation for a 3-dimensional ferromagnet with $T_c = 6.2 \text{ K}$ and $S = 5/2$, scaled along the intensity axis to obtain the excellent agreement with the data. The same mean-field-like temperature dependence of the integrated (111) intensity was found previously for samples of $\text{Sn}_{0.97}\text{Mn}_{0.03}\text{Te}$ with $p = 7 \times 10^{20} \text{ cm}^{-3}$ and $\text{Sn}_{0.94}\text{Mn}_{0.06}\text{Te}$ with $p = 11 \times 10^{20} \text{ cm}^{-3}$ (see section 3.2).

With Eq. (2.14) a "theoretical" value for the maximum integrated magnetic (111) intensity can be calculated from the measured integrated nuclear (222) intensity. Assuming that the actual Mn-concentration is equal to the nominal value $x = 0.04$, the observed magnetic

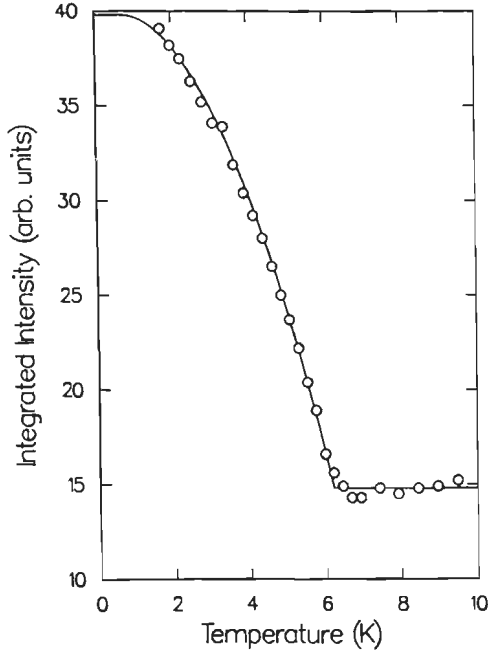


Figure 4.9: Temperature dependence of the integrated (111) intensity for $\text{Sn}_{0.96}\text{Mn}_{0.04}\text{Te}$ with $p = 7 \times 10^{20} \text{ cm}^{-3}$, triple-axis mode, $B = 0.0 \text{ mT}$. Full curve: mean-field approximation with $S = 5/2$ and $T_c = 6.2 \text{ K}$, scaled along the intensity axis.

(111) intensity (extrapolated to $T = 0 \text{ K}$) amounts to (0.87 ± 0.03) of the calculated value, corresponding to a magnetisation of (0.93 ± 0.02) of the theoretical value. This is the same range as the value deduced from the neutron diffraction experiments for the sample with $x = 0.03$ and $p = 7 \times 10^{20} \text{ cm}^{-3}$ (0.98 ± 0.14) and significantly closer to the theoretical saturation magnetisation than the values deduced for the ferromagnetic samples with $x = 0.06$, $p = 11 \times 10^{20} \text{ cm}^{-3}$ (0.75 ± 0.02) and $x = 0.10$, $p = 14 \times 10^{20} \text{ cm}^{-3}$ (0.79 ± 0.02) (see section 3.2). By the application of a magnetic field while cooling through T_c the observed magnetic intensity increases: fields of 2.5 and 5.0 mT yield magnetisations of 1.00 and 1.05 times the theoretical value, respectively. This increase must be attributed to the fact that domains with a magnetisation component along the field are favoured when the domains are formed, meaning that crystallographically equivalent domains do no longer contain an equal number of spins.

The separate magnetic (111) reflection was obtained by subtracting the nuclear (111) profile, measured above the transition temperature T_c , from the composite profile observed at temperatures below T_c . At all temperatures below T_c the magnetic (111) reflection can be fitted to a Gaussian profile with a linewidth that is within the experimental accuracy equal to the experimental resolution as determined by the FWHM of the nuclear (111) reflection. This indicates that the ferromagnetic order below the critical temperature is

truly long range, and confirms the ferromagnetic character of the low-temperature phase for this carrier concentration.

4.3.3 Results for $\text{Sn}_{0.96}\text{Mn}_{0.04}\text{Te}$ with $p = 11 \times 10^{20} \text{ cm}^{-3}$

Figure 4.10 shows the integrated intensity of the (111) reflection as a function of temperature for the as-grown $p = 11 \times 10^{20} \text{ cm}^{-3}$ crystal in fields of 0.0 mT, 2.5 mT, and 5.0 mT. For reasons that will become clear below, in this case the integrated intensity has not been determined by fitting a Gaussian profile to the (111) reflection, but by a point-by-point summation over the measured profile. The data in the figure are obtained from the triple-axis experiments with zero energy transfer. Because the measurements in two-axis configuration yielded similar results, they will not be discussed here. It is obvious that, unlike the sample with $p = 7 \times 10^{20} \text{ cm}^{-3}$, the temperature dependence of the magnetic intensity in zero field cannot be described with a mean-field prediction. With decreasing temperature the intensity starts to rise at approximately 6.5 K, indicating a transition to a ferromagnetic state, but the increase is more gradual than for the sample with $p = 7 \times 10^{20} \text{ cm}^{-3}$. The most striking departure from mean-field behaviour occurs just above 2 K, where the intensity reaches a maximum at 2.1 K and then decreases with decreasing temperature. The magnetisation derived from the maximum observed magnetic

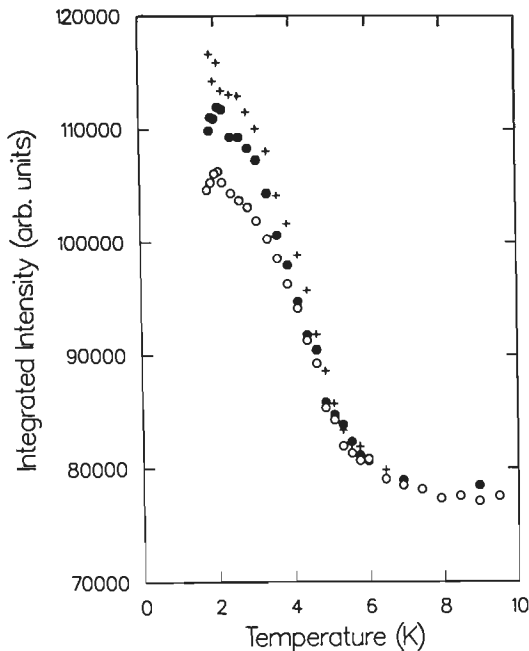


Figure 4.10: Temperature dependence of the integrated (111) intensity for $\text{Sn}_{0.96}\text{Mn}_{0.04}\text{Te}$ with $p = 11 \times 10^{20} \text{ cm}^{-3}$, triple-axis mode, $B = 0.0 \text{ mT}$ (○), $B = 2.5 \text{ mT}$ (●), and $B = 5.0 \text{ mT}$ (+).

intensity in zero field amounts to (0.70 ± 0.02) of the theoretical value calculated from the integrated nuclear (222) intensity, assuming the nominal Mn-concentration and inserting $\langle S \rangle = x \cdot 5/2$ in Eq. (2.14). Applying a 2.5 mT field increases the maximum observed intensity to a value corresponding to a magnetisation of (0.76 ± 0.02) times the theoretical value, but, as can be seen in Fig. 4.10, does not remove the decrease of the intensity below 2.1 K. In a 5.0 mT field no decrease of the magnetic intensity with decreasing temperature is observed in the range down to 1.8 K. The observed magnetic intensity at 1.8 K corresponds to a fraction of (0.80 ± 0.02) of the theoretical magnetisation.

We now turn to the analysis of the separate magnetic (111) profile, again obtained by subtraction of the nuclear (111) profile, measured at temperatures above 6.5 K, from the composite profiles observed below this temperature. Above 5.5 K the magnetic profiles could not be determined accurately enough to perform meaningful fits. Whereas the nuclear reflection can well be described by the Gaussian profile, this is not the case for all magnetic profiles, except those observed at temperatures below 4 K in the 5.0 mT field. For this reason the integrated intensities plotted in Fig. 4.10 were not determined by Gauss-fits to the composite (111) profile, but by point-to-point summation. All magnetic reflections observed in zero field and in the 2.5 mT field and those observed at temperatures above 4 K in the 5.0 mT field are significantly broader than the nuclear ones and display non-Gaussian wings that are not present in the nuclear reflections. As an example, Fig. 4.11 shows the magnetic profile observed at 1.8 K in zero field, together with a Gaussian profile with the same amplitude and with the FWHM of the nuclear (111) reflection. The broad, non-Gaussian profile of the magnetic reflection implies that ferromagnetic order, that sets in below 6.5 K as indicated by the data in Fig. 4.10, is *not* long ranged. Only in the measurements in 5.0 mT below 4 K the magnetic order cannot be distinguished from true long-range order. In the fields of 0.0 and 2.5 mT long-range order is not established in the temperature range down to 1.8 K.

An alternative description of magnetic intensity profiles resulting from short- or intermediate-range order is the Lorentzian form

$$I = B + \frac{I_0}{q^2 + \kappa^2} \quad (4.1)$$

where κ is the half width at half maximum (HWHM). This Lorentzian profile can be attributed to scattering by finite magnetic clusters characterised by a correlation length $1/\kappa$, assuming a correlation damping function $D(R)$ of the form²⁰:

$$D(R) = \frac{1}{R} \exp[-\kappa R] \quad (4.2)$$

The function $D(R)$ describes the decrease of the correlations between two spins with increasing distance between them. The experimentally observed profile in case of scattering

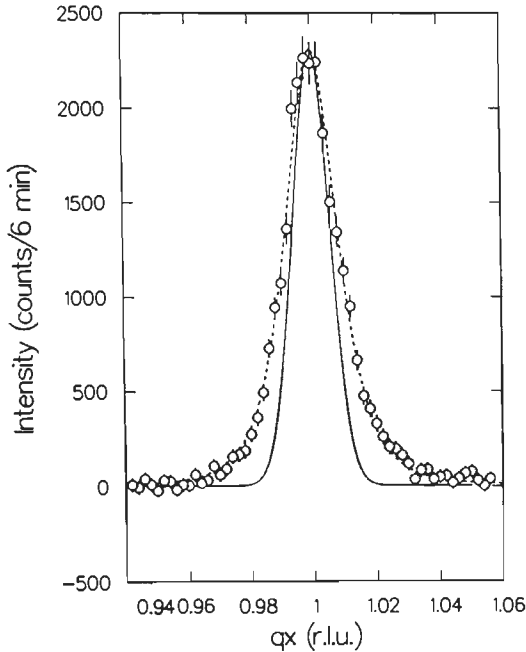


Figure 4.11: $\text{Sn}_{0.98}\text{Mn}_{0.04}\text{Te}$, $p = 11 \times 10^{20} \text{ cm}^{-3}$, triple-axis mode, $T = 1.8 \text{ K}$, $B = 0.0 \text{ mT}$: the magnetic (111) profile along the [110] direction. Dashed curve: fit to a Lorentzian, convoluted with the Gaussian experimental resolution function. Full curve: Gaussian with the width of the experimental resolution function.

with an intrinsic Lorentzian character is determined by the convolution of the Lorentzian with the Gaussian experimental resolution function. Where possible, we fitted the magnetic (111) reflections with a lineshape resulting from such convolution. In these fits the FWHM of the Gaussian was fixed at the value determined from the nuclear (111) reflection. This lineshape appeared to give a good description of the experimental data, as can be seen in Fig. 4.11 for the data at 1.8 K in zero field. Figure 4.12 displays the inverse correlation length κ deduced from these fits as a function of temperature, where κ is expressed in reciprocal lattice units ($1 \text{ r.l.u.} = 2\pi/a_0 \approx 1 \text{ \AA}^{-1}$). No data are shown for the 5.0 mT field below 4.8 K, because in this temperature range the Lorentzian has become too narrow ($\kappa < 0.002 \text{ r.l.u.}$, i.e. a correlation length $> 500 \text{ \AA}$) to perform a successful deconvolution. However, only below 4 K the width of the observed magnetic profile is equal to the experimental resolution, corresponding to $\kappa \equiv 0$ and implying long-range order. In zero-field as well as in fields of 2.5 mT and 5.0 mT κ initially decreases when the temperature is lowered, until it becomes constant near 4 K. In 0.0 mT and 2.5 mT κ remains finite below 4 K, in 5.0 mT it equals zero. The decrease of κ reflects the increase of the ferromagnetic correlation length, i.e. the growth of ferromagnetically ordered clusters, with decreasing temperature. The fact that at a fixed temperature the value of

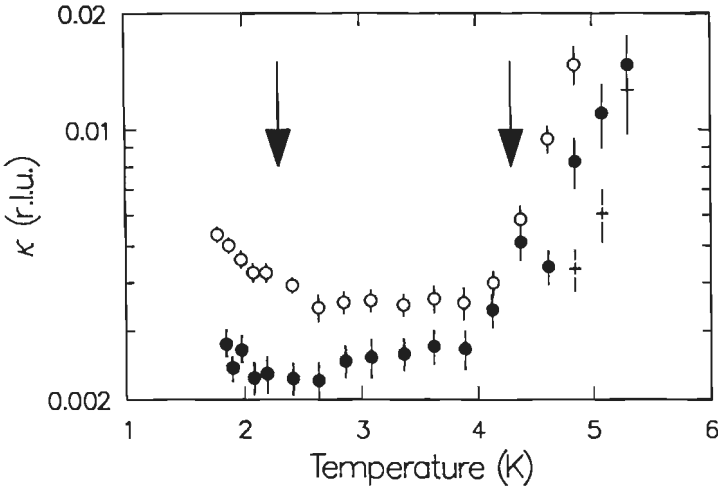


Figure 4.12: $\text{Sn}_{0.96}\text{Mn}_{0.04}\text{Te}$, $\rho = 11 \times 10^{20} \text{ cm}^{-3}$, triple-axis mode: temperature dependence of the inverse correlation length κ , $B = 0.0 \text{ mT}$ (\circ), $B = 2.5 \text{ mT}$ (\bullet), and $B = 5.0 \text{ mT}$ ($+$). Arrows denote the temperatures at which the real (right arrow) and imaginary (left arrow) component of the ac susceptibility have their maximum at frequencies up to 913 Hz (cf. Fig. 4.5).

κ significantly decreases with increasing field, implies that the correlations are drastically enhanced by the application of a field. Below 4 K a field of 5.0 mT appears to be sufficient for the formation of a magnetic cluster of apparently infinite size. In zero field the constant value of κ below 4 K corresponds to a ferromagnetic correlation length of approximately $275 \pm 25 \text{ \AA}$, which is equal to roughly twenty times the average Mn-Mn distance for this Mn concentration.

In the case of the zero field measurements κ increases with decreasing temperature below 2.5 K. This occurs in the temperature range where the integrated magnetic intensity reaches its maximum. The increasing width of the magnetic reflection implies a decrease of the ferromagnetic correlation length and suggests a transition from a (restricted-range) ferromagnetic order to a spin-glass-like state. Obviously a field as small as 2.5 mT is sufficient to suppress this effect: in this field κ remains more or less constant at the value reached near $T = 4 \text{ K}$, although also in this case the integrated intensity decreases below 2 K. An increase of κ at lower temperatures can therefore not be excluded. The broadening of the distribution of the magnetic intensity in reciprocal space in zero field at temperatures below 2.5 K is not only reflected in the increase of κ , but also in the temperature dependence of the intensity observed at the reciprocal lattice point (1.00,1.00,1.00). The integrated intensity of a reflection is proportional to the product of its width and its peak intensity. The decreasing integrated intensity below 2.5 K (cf. Fig. 4.10), in combination with the increase of κ , therefore implies a more pronounced decrease of the peak intensity. This is illustrated in Fig. 4.13, where this peak intensity is plotted versus temperature for $B = 0.0 \text{ mT}$ and $B = 5.0 \text{ mT}$. Similarly, the effect of the magnetic field on the peak intensity is relatively larger than on the integrated intensity.

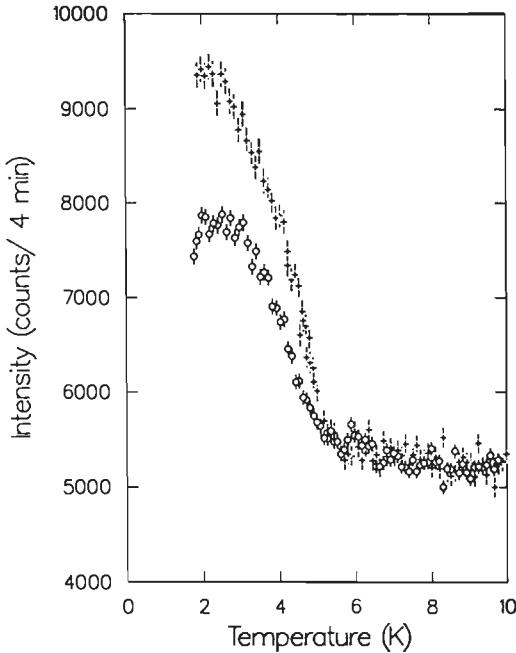


Figure 4.13: $\text{Sn}_{0.96}\text{Mn}_{0.04}\text{Te}$, $p = 11 \times 10^{20} \text{ cm}^{-3}$, triple-axis mode: temperature dependence of the intensity in the reciprocal lattice point $(1.00, 1.00, 1.00)$, $B = 0.0 \text{ mT}$ (\circ) and $B = 5.0 \text{ mT}$ ($+$).

This is in agreement with the data in Figs. 4.10 and 4.12: in 5.0 mT the integrated intensity is always larger than in 0.0 mT, whereas κ is always smaller.

The same temperature dependence of the inverse correlation length as that observed in zero field, also in combination with a decrease of intensity at low temperatures, was found by Maletta *et al.*² in their experiments on $\text{Eu}_x\text{Sr}_{1-x}\text{S}$ reentrant spin glasses. This corroborates the conclusion from our susceptibility and magnetisation experiments that $\text{Sn}_{0.96}\text{Mn}_{0.04}\text{Te}$ with $p = 11 \times 10^{20} \text{ cm}^{-3}$ is a reentrant spin glass. With decreasing temperature first a phase with a limited-range ferromagnetic order is gradually formed between 6.5 and 4 K, followed by a transition to a spin-glass phase between 2.5 and 2.0 K. This interpretation is supported by the agreement between the characteristic temperatures in the behaviour of κ in zero field and those in the susceptibility, displayed in Fig. 4.3. The latter temperatures are indicated by the arrows in Fig. 4.12. The real part of the susceptibility goes through a maximum in the temperature range where κ becomes constant when the temperature is lowered, indicating a ferromagnetic transition, whereas the imaginary part (for frequencies up to 913 Hz) has its maximum near the temperature where κ starts to increase, indicating the transition to the spin-glass state.

4.3.4 Results for $\text{Sn}_{0.96}\text{Mn}_{0.04}\text{Te}$ with $p = 23 \times 10^{20} \text{ cm}^{-3}$

In Fig. 4.14 the scaled integrated intensity of the (111) reflection, obtained by point-by-point summation, is displayed versus temperature for the $\text{Sn}_{0.96}\text{Mn}_{0.04}\text{Te}$ single crystal with $p = 23 \times 10^{20} \text{ cm}^{-3}$, together with the corresponding data for the other two samples. The data in the figure are from the triple-axis measurements, with zero energy transfer, but the temperature dependence of the integrated intensity in double-axis mode was qualitatively similar. To enable a fair comparison, the intensity has been normalised by subtracting the nuclear scattering observed at temperatures above 6 K and subsequent scaling to the maximum magnetic intensity calculated from the observed nuclear (222) intensity with Eq. (2.14). The figure shows that below 6 K some magnetic (111) intensity is present for the crystal with $p = 23 \times 10^{20} \text{ cm}^{-3}$, but that it is much smaller than for the other two samples. The maximum observed magnetic intensity in triple-axis mode amounts to roughly 10 % of the value expected from Eq. (2.14), corresponding to a magnetisation of ~ 0.32 of the theoretical value for $x = 0.04$ and $\langle S \rangle = x \cdot 5/2$. The application of a magnetic field of 5.0 mT had no effect on the observed intensity.

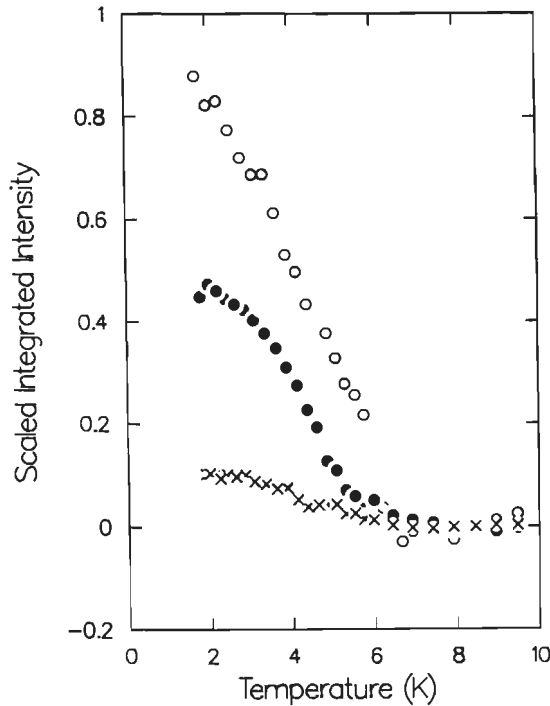


Figure 4.14: Temperature dependence of the magnetic (111) intensity, scaled on the maximum magnetic (111) intensity calculated from the nuclear (222) intensity, for $\text{Sn}_{0.96}\text{Mn}_{0.04}\text{Te}$ samples with $p = 7 \times 10^{20} \text{ cm}^{-3}$ (O), $p = 11 \times 10^{20} \text{ cm}^{-3}$ (■), and $p = 23 \times 10^{20} \text{ cm}^{-3}$ (x). Triple-axis mode, $B = 0.0 \text{ mT}$.

The magnetic intensity is so small that the subtraction procedure to separate the magnetic and the nuclear (111) profiles could not be applied at each individual temperature. As an alternative the magnetic profile at low temperatures was obtained by subtracting the sum of five scans performed between 8 and 10 K from the sum of the five scans performed below 2.2 K. Figures 4.15a and 4.15b show the results for the double- and triple-axis measurements, respectively. Besides the statistical errors in the intensities resulting from the addition and subtraction procedures, which are represented by the error bars in Fig. 4.15, there is an additional uncertainty in the data. This uncertainty results from minute differences in the sample orientation between measurements at different temperatures, which cause a shift of the centre of the observed peak. Although this shift is generally small (typically smaller than 0.005 r.l.u.), subtraction of peaks with different centre positions can, especially in the case of small magnetic intensities, lead to the large jumps in intensity from one point to another, which are visible in Figs. 4.15a and 4.15b. A comparison between the Figs. 4.15a and 4.15b indicates that for this sample there is a significant difference between the double- and triple-axis magnetic profiles. In both double- and triple-axis mode the magnetic profile does not have a Gaussian form, in contrast to the nuclear (111) Bragg-reflection, of which the FWHM is indicated in the figure, but the profile observed in triple-axis configuration appears to be much more diffuse than that from the double-axis measurements. In the latter case there obviously is a considerable contribution to the scattered intensity from inelastic processes, which

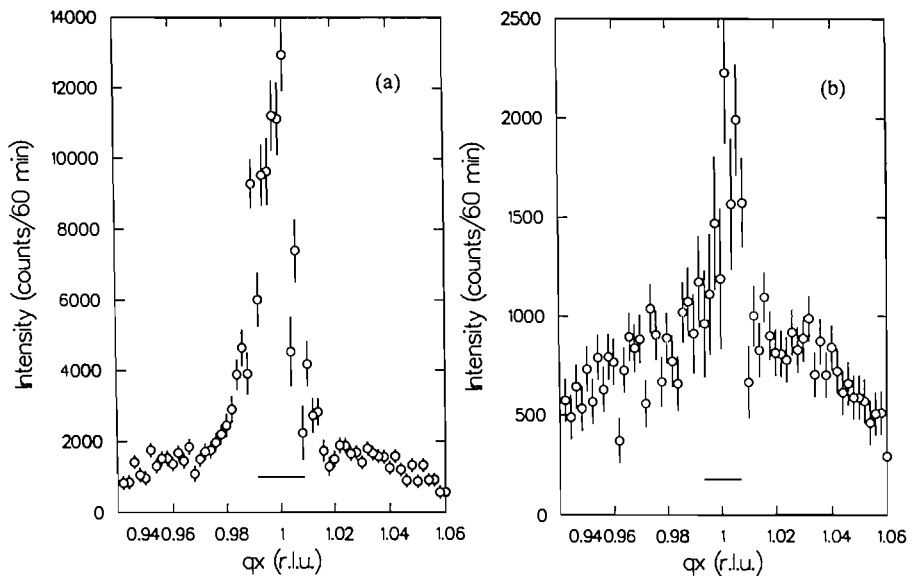


Figure 4.15: $\text{Sn}_{0.96}\text{Mn}_{0.04}\text{Te}$, $p = 23 \times 10^{20} \text{ cm}^{-3}$: magnetic (111) profile along the [110] direction at $T = 2 \text{ K}$, (a) double-axis mode, (b) triple-axis mode. Horizontal lines represent the respective experimental resolutions (FWHM).

cause the sharp peak superposed on the very broad distribution from (quasi-)elastic processes. By the installation of the analyser, which allows the observation of neutrons scattered with an energy-change $\Delta E < 1.5$ meV only, this contribution is removed. An attempt to determine a characteristic energy of the inelastic processes did not succeed. Although the diffuse character of the magnetic scattering is somewhat less pronounced in the double-axis measurements, both in the double- and in the triple-axis mode the distribution in Q-space of the magnetic (111) scattering is more diffuse than that of the nuclear (111) scattering. This implies that the ferromagnetic correlations in real space have a short-range character. They are gradually built up below 6 K, resulting in the increase in intensity depicted in Fig. 4.14. Because of this short-range character, we believe that the observation of magnetic intensity in zero field at the nuclear (111) Bragg-position does not violate the conclusion from the measurements of the susceptibility, the magnetisation, and the specific heat that the low-temperature phase for this combination of Mn concentration and charge carrier concentration is a spin-glass phase. In fact, in a real spin glass, containing a few percent solute magnetic atoms, the presence of short-range magnetic correlations is inevitable, even if the positional randomness of the magnetic and non-magnetic atoms is complete.²¹

The temperature below which the scattered intensity increases, approximately 6 K, may be regarded as the freezing temperature corresponding to the particular time constant ($\sim 3 \times 10^{-12}$ s) determined by the energy window $\Delta E = 1.5$ meV. Spins which are not frozen, but are involved in a relaxation process with a time constant $\tau > 3 \times 10^{-12}$ s, contribute to the quasi-elastic scattering and are indistinguishable from frozen spins, for which $\tau \rightarrow \infty$. Because of the different time constant ($\sim 10^{-3}$ s,) the susceptibility measurements yield a different freezing temperature ($T_f \approx 2.2$ K). A similar dependence of the apparent freezing temperature on the characteristic time constant of the measurement was reported by Murani and Heidemann²¹ for a CuMn spin glass.

4.4 Discussion

Experimental evidence has been presented for the existence of a transition from a ferromagnetic phase into a spin-glass phase in the diluted magnetic semiconductor $\text{Sn}_{0.96}\text{Mn}_{0.04}\text{Te}$, induced by an increase in the charge carrier concentration alone. The breakdown of the long-range ferromagnetically ordered phase is a gradual process. In the sample with $p = 7 \times 10^{20} \text{ cm}^{-3}$ a long-range-ordered ferromagnetic state is observed. In the sample with $p = 11 \times 10^{20} \text{ cm}^{-3}$ initially a limited-range ferromagnetic order is established with decreasing temperature, but when the temperature is lowered further this ferromagnetic order collapses and a reentrant spin-glass phase is entered. For the sample with $p = 23 \times 10^{20} \text{ cm}^{-3}$ a direct transition from the paramagnetic phase into a spin-glass phase occurs. It must be stressed that the transition from the ferromagnetic regime to the spin-glass regime with increasing charge carrier concentration occurs at fixed Mn concentration. This is in contrast with systems such as $\text{Eu}_x\text{Sr}_{1-x}\text{S}^{22}$, AgFe^{14} , AuFe^{14} , and $(\text{Fe}_x\text{Mn}_{1-x})_5\text{P}_{16}\text{B}_6\text{Al}_3^{23}$, in which a similar transition, also with an intermediate

reentrant spin-glass regime, was observed. For all these materials, however, the transitions between the different magnetic regimes were induced by a change of the concentration of magnetic ions.

Because the Curie-Weiss temperature Θ remains constant when the charge carrier concentration is increased, the breakdown of the ferromagnetic state is apparently not caused by a change of the total interaction strength. In that respect this transition is different from that occurring at $p_c = 3 \times 10^{20} \text{ cm}^{-3}$, where the ferromagnetism is so to say switched on.²⁴ Both the rise of Θ at p_c and the p -independence of Θ observed for $p \geq 7 \times 10^{20} \text{ cm}^{-3}$ are in agreement with recent calculations by Story *et al.*²⁵ on basis of the RKKY model described in section 1.3. In these calculations the anisotropy and the many-valley structure of the heavy hole Σ band were incorporated in the original model of Swagten *et al.*²⁶

The experiments discussed in this chapter have revealed that the condition $p > p_c$ does not necessarily imply that a ferromagnetically ordered phase is formed at low temperatures. Actually, the present data show that only in a limited range of charge carrier concentrations above p_c a ferromagnetic phase is formed and that the ferromagnetism collapses as the carrier concentration is further increased. This sheds a new light on the magnetic (T, x) phase diagram reported by Mauger and Escorne²⁷ (Fig. 1.8), who predict a reentrant spin-glass phase for $x = 0.04$, and also on the data reported in chapter 3. Obviously, the low-temperature magnetic behaviour for $p > p_c$ is not determined by x or by p separately, but by the combination of them. This was not fully recognised by Mauger and Escorne, who only studied the influence of the Mn concentration. By combining the present results with those for other Mn concentrations and charge carrier concentrations the relation between x , p , and the low-temperature magnetic behaviour, in other words the three dimensional (T, x, p) magnetic phase diagram, can be constructed. This will be discussed in the next chapter, where it will also be demonstrated that with the assumption of RKKY interactions between the magnetic moments it is possible to understand the carrier-concentration-induced transition between a ferromagnetic regime and a spin-glass regime at fixed Mn concentration.

It is obvious that additional experiments on samples with carrier concentrations in the range $11 \times 10^{20} \text{ cm}^{-3} < p < 23 \times 10^{20} \text{ cm}^{-3}$ are essential to study the gradual breakdown of ferromagnetism with increasing p at fixed x in more detail. However, thus far it has been difficult to control the isothermal annealing process in such a way that every desired carrier concentration can be achieved. Concerning the neutron scattering experiments, especially for the $\text{Sn}_{0.96}\text{Mn}_{0.04}\text{Te}$ crystal with $p = 11 \times 10^{20} \text{ cm}^{-3}$ measurements below 1.8 K would be interesting. In zero field a further decrease of the size of the ferromagnetically ordered clusters might be expected, which might eventually lead to results similar to those found in the present experiments on the $p = 23 \times 10^{20} \text{ cm}^{-3}$ sample. Also the effect of the magnetic field should be studied in more detail. Measurements in a field of 2.5 mT might reveal whether in this field the observed decrease of the integrated intensity is also accompanied by a decrease of the correlation length, starting at a lower temperature than in the zero field case. A decrease of the intensity at low temperatures can also not be excluded in the 5.0 mT field. The observed field dependence of the integrated intensity and the correlation length actually implies the extension of

the three dimensional (T,x,p) phase diagram to a four dimensional (T,x,p,B) phase diagram. Besides neutron scattering experiments, also magnetisation measurements, both field cooled and zero field cooled, in different fields can contribute to the compilation of such a diagram. Finally, for the crystal with $p = 23 \times 10^{20} \text{ cm}^{-3}$ inelastic neutron scattering experiments with a better energy resolution might clarify the nature of the fluctuation processes that cause the observed difference between the double- and triple-axis measurements.

References

1. W.J.M. de Jonge, T. Story, H.J.M. Swagten, and P.J.T. Eggenkamp, *Europhys. Lett.* **17**, 631 (1992).
2. H. Maletta, G. Aeppli, and S.M. Shapiro, *J. Magn. Magn. Mater.* **31-34**, 1367 (1983).
3. B.H. Verbeek, G.J. Nieuwenhuys, H. Stocker, and J.A. Mydosh, *Phys. Rev. Lett.* **40**, 586 (1978).
4. H. Kunkel, R.M. Roshiko, W. Ruan, and G. Williams, *Phil. Mag. B* **64**, 153 (1991).
5. R.B. Goldfarb, F.R. Fickett, K.V. Rao, and H.S. Chen, *J. Appl. Phys.* **53**, 7687 (1982).
6. V. Cannella and J.A. Mydosh, *Phys. Rev. B* **6**, 4420 (1972).
7. A.F.J. Morgownik and J.A. Mydosh, *Phys. Rev. B* **24**, 5277 (1981).
8. J.A. Mydosh and G.J. Nieuwenhuys in *Ferromagnetic Materials*, vol. 1, E.P. Wohlfarth, editor (North Holland, Amsterdam, 1980).
9. H. Maletta and W. Felsch, *Phys. Rev. B* **20**, 1245 (1979).
10. R.S. Tebble and D.J. Craik, *Magnetic Materials* (Wiley, London, 1969).
11. C.A.M. Mulder, A.J. van Duynveldt, and J.A. Mydosh, *Phys. Rev. B* **23**, 1384 (1981).
12. C.Y. Huang, *J. Magn. Magn. Mater.* **51**, 1 (1985).
13. J.L. Dormann, A. Saifi, V. Cagan, and M. Nogues, *Phys. Stat. Solidi (b)* **131**, 573 (1985).
14. G.J. Nieuwenhuys, B.J. Verbeek and J.A. Mydosh, *J. Appl. Phys.* **50**, 1685 (1979).
15. L.E. Wenger and P.H. Keesom, *Phys. Rev. B* **13**, 4053 (1976).
16. D.L. Martin, *Phys. Rev. B* **21**, 1906 (1980).
17. D.L. Martin, *Phys. Rev. B* **20**, 368 (1979).
18. B.M. Boerstael, J.J. Zwart, and J. Hansen, *Physica* **57**, 397 (1972).
19. H. Maletta and P. Convert, *Phys. Rev. Lett.* **42**, 108 (1979).
20. see for example J. Als-Nielsen in *Phase Transitions and Critical Phenomena*, vol. 5A, C. Domb and S.M. Green, editors, (Academic Press, London, 1976).
21. A.P. Murani and A. Heidemann, *Phys. Rev. Lett.* **41**, 1402 (1978).
22. H. Maletta, G. Aeppli, and S.M. Shapiro, *Phys. Rev. Lett.* **48**, 1490 (1982).
23. G. Aeppli, S.M. Shapiro, R.J. Birgeneau, and H.S. Chen, *Phys. Rev. B* **28**, 5160 (1983).
24. T. Story, R.R. Galazka, R.B. Frankel, and P.A. Wolff, *Phys. Rev. Lett.* **56**, 777 (1986).
25. T. Story, P.J.T. Eggenkamp, C.H.W. Swüste, H.J.M. Swagten, W.J.M. de Jonge, and L.F. Lemmens, *Phys. Rev. B* **45**, 1660 (1992).
26. H.J.M. Swagten, W.J.M. de Jonge, R.R. Galazka, P. Warmenbol, and J.T. Devreese, *Phys. Rev. B* **37**, 9907 (1988).
27. A. Mauger and M. Escorne, *Phys. Rev. B* **35**, 1902 (1987).

Chapter 5

The three-dimensional (T,x,p) magnetic phase diagram

5.1 Introduction

In chapter 4 it was shown that the low-temperature magnetic behaviour of $\text{Sn}_{1-x}\text{Mn}_x\text{Te}$ with carrier concentrations above the critical value p_c was dependent on the Mn concentration x as well as on the charge carrier concentration p . At constant x a transition from a long-range-ordered ferromagnetic phase to a spin-glass phase, via an intermediate reentrant spin-glass phase, was induced by a change in the charge carrier concentration *alone*: for $x = 0.04$ a ferromagnetically ordered phase was observed in a sample with $p = 7 \times 10^{20} \text{ cm}^{-3}$, reentrant spin-glass behaviour in a sample with $p = 11 \times 10^{20} \text{ cm}^{-3}$, and a spin-glass phase in a sample with $p = 23 \times 10^{20} \text{ cm}^{-3}$. In this chapter (section 5.2) the results for $x = 0.04$ will be combined with those for other Mn concentrations. The data will show that the transition from the ferromagnetic to the spin-glass regime with increasing carrier concentration at fixed x can also be observed for other compositions, and, moreover, that it is a gradual transition. In section 5.3 the experimental results will be confronted with theoretical predictions on the location of the boundary between the ferromagnetic and spin-glass regimes in the x - p phase diagram. A phenomenological description of the different magnetic phases in terms of a cluster model will be given in section 5.4. Finally, in section 5.5, some suggestions for further research will be presented.

5.2 Survey of experimental data

Experimental data for $\text{Sn}_{1-x}\text{Mn}_x\text{Te}$ are available¹⁻⁴ for compositions $0.016 \leq x \leq 0.10$ and carrier concentrations $3 \times 10^{20} \text{ cm}^{-3} \leq p \leq 23 \times 10^{20} \text{ cm}^{-3}$. In Table 5.1 a survey of the observed low-temperature magnetic behaviour is presented for three typical ranges of carrier concentrations. The trend that is observed for $x = 0.04$ is also seen for other compositions: with increasing charge carrier concentration the ferromagnetic order, observed for p immediately above p_c , deteriorates. To what degree this breakdown of

x	$p = 5 - 7 \times 10^{20} \text{ cm}^{-3}$	$p = 10 - 12 \times 10^{20} \text{ cm}^{-3}$	$p = 20 - 23 \times 10^{20} \text{ cm}^{-3}$
0.016	FM/RSG	SG	---
0.025	FM	RSG	SG
0.03	FM	RSG	SG
0.04	FM	RSG	SG
0.05	FM	RSG	SG
0.06	FM	FM	SG
0.08	FM	FM	RSG
0.10	FM	FM	FM

Table 5.1: Low-temperature magnetic phase in $\text{Sn}_{1-x}\text{Mn}_x\text{Te}$ as a function of the nominal Mn concentration for three typical ranges of charge carrier concentrations. No data are available for $x = 0.016$ with $p = 20 - 23 \times 10^{20} \text{ cm}^{-3}$. FM = ferromagnetic phase, RSG = reentrant spin-glass phase, SG = spin-glass phase.

ferromagnetic phase into a spin-glass phase is completed within the range of carrier concentrations up to $p = 23 \times 10^{20} \text{ cm}^{-3}$ depends on the Mn concentration: for $x \leq 0.06$ a spin-glass phase is observed for $p \approx 20 \times 10^{20} \text{ cm}^{-3}$, for $x = 0.08$ a reentrant spin-glass transition occurs, and for $x = 0.10$ a ferromagnetic order is maintained down to 1.3 K, the lowest temperature covered in the experiments. This is illustrated in Fig. 5.1, where the real component of the ac susceptibility is displayed versus temperature for samples with $x = 0.04, 0.06, 0.08,$ and 0.10 with $p \approx 20 \times 10^{20} \text{ cm}^{-3}$. For the lower two Mn concentrations a spin-glass like cusp is observed. For $x = 0.08$ two maxima are observed, of which the first one, at $T = 10.8 \text{ K}$, is interpreted to be related to the transition to the ferromagnetic phase and the second one, at $T = 2.3 \text{ K}$, to the transition to the reentrant spin-glass phase. For $x = 0.10$ a sharp transition to a ferromagnetically ordered phase occurs at $T \approx 15 \text{ K}$ and for $T > 1.3 \text{ K}$ no transition to a reentrant spin-glass phase is observed. However, considering the flattening of the curve for $x = 0.10$ below 3 K and the similarity in shape to the curve for $x = 0.08$, it cannot be excluded that such transition occurs at lower temperatures.

The data in Table 5.1 and Fig. 5.1 show that the breakdown of ferromagnetic order not only occurs if p is increased at fixed x , but also if x is decreased at fixed p , at least for $p \geq 10 \times 10^{20} \text{ cm}^{-3}$ and probably also for smaller p if x is reduced below $x = 0.016$. This suggests that, as a first approximation, the low-temperature magnetic behaviour is determined by the ratio p/x . However, as described in chapter 1, the contribution to the RKKY interaction by the holes from the light-hole band is negligible compared to that by those from the heavy-hole Σ band. Therefore, it seems reasonable that it is rather the ratio p_{Σ}/x , where $p_{\Sigma} = p - p_c = p - 3 \times 10^{20} \text{ cm}^{-3}$ is the concentration of holes in the Σ band, that is decisive for the nature of the low-temperature magnetic phase. To test this hypothesis, Fig. 5.2 has been compiled. The Curie-Weiss temperature Θ and the

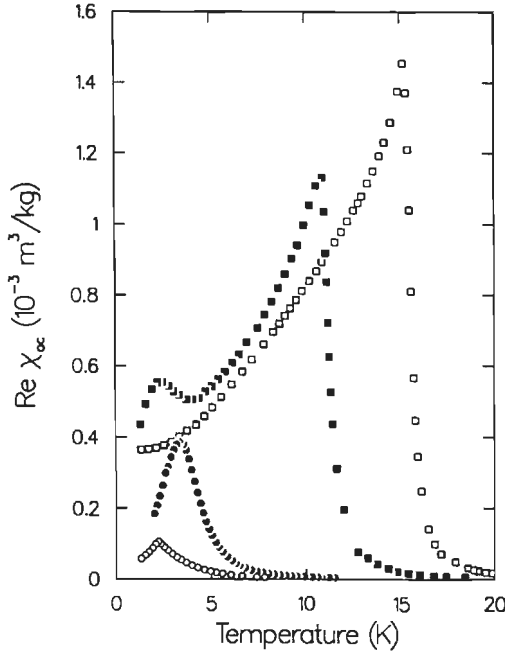


Figure 5.1: Temperature dependence of the real component of the ac susceptibility of $\text{Sn}_{1-x}\text{Mn}_x\text{Te}$ with $p \approx 20 \times 10^{20} \text{ cm}^{-3}$ and $x = 0.04$ (\circ), $x = 0.06$ (\bullet), $x = 0.08$ (\blacksquare), and $x = 0.10$ (\square).

temperature T_{\max} , at which the real component of the ac susceptibility has its maximum, both scaled on x (in % Mn), are plotted versus p_{Σ}/x (in units 10^{20} cm^{-3} per % Mn). The objective quantity T_{\max} is plotted instead of the critical temperature T_c and/or the freezing temperature T_f to avoid errors because of a possible misinterpretation of the experimental data. The scaling of Θ and T_{\max} on x has been performed to make it possible to include and compare data for different compositions. Data are included for Mn concentrations $0.016 \leq x \leq 0.10$ and carrier concentrations $3 \times 10^{20} \text{ cm}^{-3} \leq p \leq 23 \times 10^{20} \text{ cm}^{-3}$.

The figure shows that Θ/x remains more or less constant at $\Theta/x = 1.75 \text{ K}/(\% \text{ Mn})$ for $p_{\Sigma}/x \geq 1.0 \times 10^{20} \text{ cm}^{-3}/(\% \text{ Mn})$. For convenience the units for Θ/x , T_{\max}/x , and p_{Σ}/x will be omitted in the further discussion. A part of the step-like increase of Θ at $p = p_c$ can be seen for $p_{\Sigma}/x \leq 0.5$ (cf. Fig. 1.3). In the T_{\max}/x data the same increase can be seen. For $0.5 \leq p_{\Sigma}/x \leq 1.5$, T_{\max}/x goes through a rounded maximum, with a maximum value $T_{\max}/x \approx 1.5$. In this range of p_{Σ}/x the samples discussed in chapter 3 ($x = 0.03$ with $p = 7 \times 10^{20} \text{ cm}^{-3}$, $x = 0.06$ with $p = 11 \times 10^{20} \text{ cm}^{-3}$, $x = 0.10$ with $p = 14 \times 10^{20} \text{ cm}^{-3}$) and the ferromagnetic sample from chapter 4 ($x = 0.04$ with $p = 7 \times 10^{20} \text{ cm}^{-3}$) are situated. For these samples a long-range ordered ferromagnetic phase was observed. For samples with $1.5 \leq p_{\Sigma}/x \leq 3.0$ an initial transition from the paramagnetic phase to a phase with a ferromagnetic order of restricted range is followed by a transition to a spin-glass phase at lower temperature. The ferromagnetic transition is characterised by a maximum in the susceptibility at T_{\max} , with $1.5 \geq T_{\max}/x \geq 0.6$ and T_{\max}/x decreasing

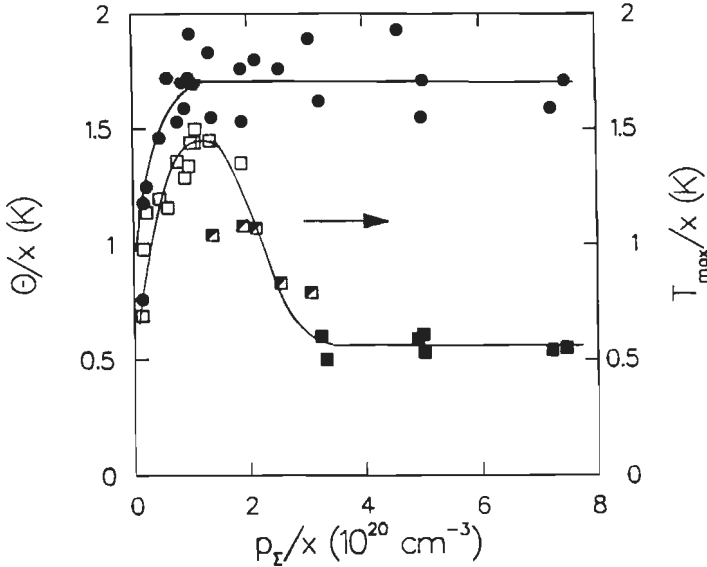


Figure 5.2: $\text{Sn}_{1-x}\text{Mn}_x\text{Te}$, $0.016 \leq x \leq 0.10$, $3 \times 10^{20} \text{ cm}^{-3} \leq p \leq 23 \times 10^{20} \text{ cm}^{-3}$: Curie-Weiss temperature (circles) and the temperature at which the real component of the ac susceptibility is maximum (squares), both scaled on the Mn concentration x (expressed in % Mn), versus the charge carrier concentration in the Σ band p_Σ , also scaled on x . Open squares: ferromagnet; semi-filled squares: reentrant spin glass; filled squares: spin glass. The lines are guides to the eye.

with increasing p_Σ/x . Simultaneously the ratio Θ/T_{\max} increases from $\Theta/T_{\max} \approx 1.2$ to $\Theta/T_{\max} \approx 3.0$. In this range the reentrant spin-glass sample from chapter 4 ($x = 0.04$ with $p = 11 \times 10^{20} \text{ cm}^{-3}$) is located. For samples with $p_\Sigma/x \geq 3.0$ a spin-glass phase is formed, directly from the paramagnetic phase, at the freezing temperature $T_f/x = T_{\max}/x \approx 0.6$. In this range Θ/T_{\max} remains constant at $\Theta/T_{\max} \approx 3.0$. The sample with $x = 0.04$ and $p = 23 \times 10^{20} \text{ cm}^{-3}$ is situated in this range of p_Σ/x .

The data in Fig. 5.2 strongly support the hypothesis that the magnetic behaviour at low temperature is determined by the ratio p_Σ/x . Moreover, the data indicate that, at fixed x , the transition from the ferromagnetic regime to the spin-glass regime with increasing p_Σ is a *gradual* transition: the gradual decrease of T_{\max}/x suggests a gradual breakdown of the ferromagnetic order for $p_\Sigma/x > 1.5$, until, for $p_\Sigma/x > 3.0$, a ferromagnetic order is no longer formed on cooling from the paramagnetic temperature range. The decisive role of the ratio p_Σ/x is in agreement with the assumption of RKKY-like interactions. As was sketched in Fig. 1.4, the RKKY interaction is a rapidly oscillating function with argument $2k_F R_j$, where k_F ($\sim p^{1/3}$) is the Fermi wave vector and R_j is the distance between the magnetic ions. For $2k_F R_j \rightarrow 0$ the interaction is ferromagnetic. In the present systems two characteristic distances can be distinguished. The first, R_0 , is the distance at which the first change from ferromagnetic to antiferromagnetic interaction occurs. R_0 depends

on the charge carrier concentration as $R_0 \sim p^{-1/3}$. The second, $R_{\text{Mn-Mn}}$, is the average spin-spin distance, which depends on the Mn concentration as $R_{\text{Mn-Mn}} \sim x^{-1/3}$. The ratio between $R_{\text{Mn-Mn}}$ and R_0 , or, equivalently, p and x , is of crucial importance for the magnetic behaviour. If $R_0 \ll R_{\text{Mn-Mn}}$ there is a strong competition between positive, ferromagnetic interactions and negative, antiferromagnetic interactions, leading to the formation of a spin-glass phase. If $R_0 \gg R_{\text{Mn-Mn}}$, ferromagnetic interactions dominate over the oscillatory behaviour and no spin-glass phase will be formed, but a ferromagnetically ordered phase. In the next section it will be shown that in $\text{Sn}_{1-x}\text{Mn}_x\text{Te}$ the situation is intermediate between these two extremes. R_0 and $R_{\text{Mn-Mn}}$ are of comparable magnitude and a relatively small decrease of R_0 , induced by an increase of the charge carrier concentration, can lead to the observed collapse of ferromagnetism. It will also be demonstrated that within the framework of the RKKY interaction the carrier-concentration-induced breakdown of ferromagnetism can not only be understood qualitatively, but that also satisfactory quantitative predictions on the relation between p , x , and the low-temperature magnetic behaviour are possible.

Returning to Fig. 5.2, some care must be taken in the interpretation of the data for constant x . Generally, for each x experimental data have been obtained only for values of p in the three ranges indicated in Table 5.1. This means that a figure such as Fig. 5.2 cannot yet be compiled for one constant value of x . A complete set of data at fixed Mn concentration could demonstrate whether Θ and especially T_{max} are really constant if p exceeds a certain value at fixed x , or that the constancy suggested by Fig. 5.2, is the result of including data for several x in one figure. Samples with $x \leq 0.025$ would be the most suited ones to study the p dependence of Θ and T_{max} at fixed x , because only for small x the full range of $0 \leq p/x \leq 8$ can be covered. Only for $x < 0.025$ extension to $p/x > 8$ by increasing p is possible within the stability area in the metallurgical (T, p) SnTe phase diagram (Fig. 2.4). Concerning Θ , the available data for $x \leq 0.06$ indicate that, if p is increased at fixed x , Θ remains constant at the value it has in the ferromagnetic regime, in spite of the occurring collapse of the ferromagnetic state into a spin-glass state for these Mn concentrations. For $x = 0.04$ this was demonstrated in chapter 4 (see Table 4.1), where it was already noted that this behaviour is in agreement with recent calculations by Story *et al.*⁵ The Curie-Weiss temperature monitors the total interaction strength. In principle, Θ might be expected to decrease to zero if p is increased so far that the condition $R_0 \ll R_{\text{Mn-Mn}}$ is fulfilled and the antiferromagnetic contributions to the total interaction outweigh the ferromagnetic contributions. Because of the limited range of carrier concentrations that can be achieved, for $\text{Sn}_{1-x}\text{Mn}_x\text{Te}$ this situation might be reached only for very small x , i.e. $x < 0.01$. However, thus far it is not known whether for these Mn concentrations a ferromagnetic phase is formed at all. Concerning T_{max} , the data in Fig. 5.2 indicate that the freezing temperature is independent of p at fixed x and equal to $T_f \approx 0.6x$ for $p/x > 3$. However, this has not yet been verified for one constant value of x experimentally. Therefore, Fig. 5.2 should provisionally be interpreted such that for $x \leq 0.06$ the freezing temperature for $p \approx 20 - 23 \times 10^{20} \text{ cm}^{-3}$ scales with the Mn concentration.

For the reentrant spin-glass systems the transition temperature T_f to the spin-glass phase, determined from the maximum in the imaginary component of the ac susceptibility, is

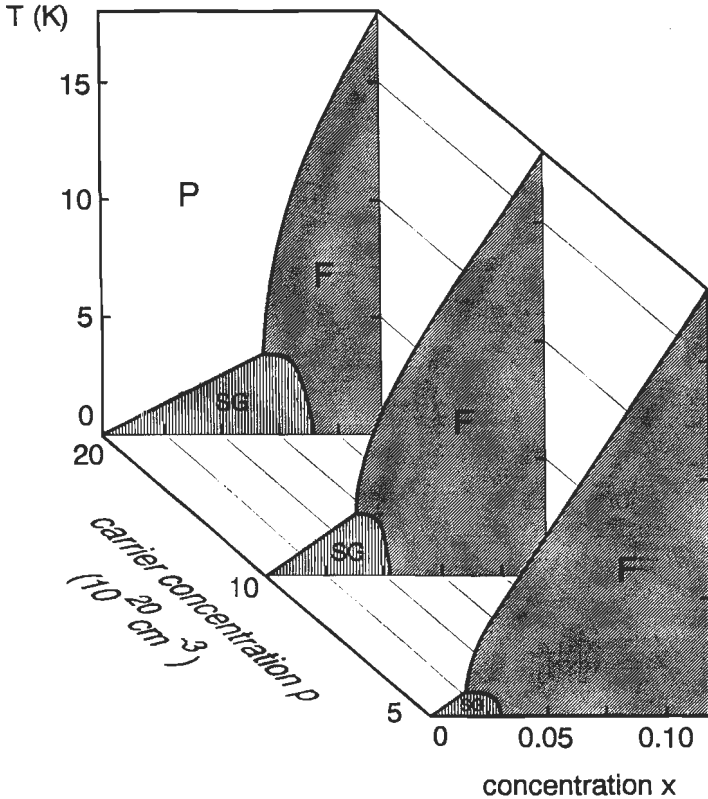


Figure 5.3: Three-dimensional (T,x,p) magnetic phase diagram of $\text{Sn}_x\text{Mn}_{1-x}\text{Te}$. P = paramagnetic phase, F = ferromagnetic phase, SG = spin-glass phase. The p scale is not linear.

not included in Fig. 5.2. Up till now a reentrant spin-glass phase has been observed in samples with $x = 0.03$, $x = 0.04$, and $x = 0.05$ with $p \approx 10 \times 10^{20} \text{ cm}^{-3}$ and $x = 0.08$ with $p \approx 22 \times 10^{20} \text{ cm}^{-3}$. For these samples T_g/x is in the range 0.3 - 0.7, but there is no clear trend with p_g/x . This is also reflected in Fig. 5.3, where a tentative three-dimensional (T,x,p) magnetic phase diagram is presented. If a cross section at a fixed charge carrier concentration is made, a (T,x) phase diagram is obtained which is similar to that reported by Mauger and Escorne⁶, reproduced in Fig. 1.8. However, as mentioned in section 4.4, the role of the charge carrier concentration was not fully recognised by Mauger and Escorne. Three phases can be distinguished in such a (T,x) diagram: the paramagnetic, the ferromagnetic, and the spin-glass phase. These phases meet in a triple point, which shifts towards higher x and higher T with increasing p . The exact shape of the boundary between the ferromagnetic phase and the spin-glass phase, corresponding to the reentrant spin-glass transition, is not yet clear. The available data indicate that, starting from the triple point, towards higher x an initially slow decrease of the transition temperature is followed by a steep decline towards $T = 0 \text{ K}$. Of course the diagram in

Fig. 5.3 is still far from complete. We will come back to this in the final section of this chapter, where suggestions for further research will be presented.

5.3 Model calculations on the x-p magnetic phase diagram

5.3.1 Introduction

In this section the attention will be concentrated on the x-p cross section at $T = 0$ K of the three-dimensional (T,x,p) magnetic phase diagram. An extended version of this x-p diagram is displayed in Fig. 5.4. The p scale now stretches from $p = 1.0 \times 10^{20} \text{ cm}^{-3}$ to $p = 1.0 \times 10^{23} \text{ cm}^{-3}$, and the data on $\text{Sn}_{1-x}\text{Mn}_x\text{Te}$ have been supplemented with data on $\text{Pb}_{1-x-y}\text{Sn}_y\text{Mn}_x\text{Te}$.^{3,7,8,9} The compound $\text{Pb}_{0.28-x}\text{Sn}_{0.72}\text{Mn}_x\text{Te}$ has been shown to display an analogous carrier-concentration-induced breakdown of a ferromagnetic state³. Strictly speaking, the data in Fig. 5.4 represent the magnetic phase at $T = 1.3$ K, the lowest temperature generally covered in the experiments on both compounds. The utmost left side of the diagram represents the carrier-concentration-induced ferromagnetism. As described in chapter 1, this phenomenon is intimately related to the band structure of $\text{Pb}_{1-x-y}\text{Sn}_y\text{Mn}_x\text{Te}$. For $p < p_c = 3 \times 10^{20} \text{ cm}^{-3}$ paramagnetic behaviour, denoted by crosses, is maintained down to at least $T = 1.3$ K. At $p = p_c$, denoted by the dashed line, the ferromagnetic interactions become effective, resulting in a ferromagnetically ordered phase (open symbols), as was demonstrated in chapter 3. When p is further increased the phenomenon described in chapter 4 occurs: the ferromagnetically ordered phase collapses, via an intermediate reentrant spin-glass phase (semi-filled symbols), into a spin-glass phase (filled symbols). At the right-hand side of the diagram a few representative examples of canonical RKKY spin-glasses, which have carrier concentrations $\sim 10^{23} \text{ cm}^{-3}$, are shown.¹⁰

In the remainder of this section the location of the boundary between the ferromagnetic and the spin-glass regimes in this diagram will be calculated in two different ways. All calculations have in common that they are based on the two-band RKKY model, described in section 1.3. In this model the total exchange interaction contains contributions from two valence bands:

$$J_{\text{tot}} = x \sum_{i=1}^2 \sum_j z_j J_{\text{VBi}}(R_j) \quad (5.1)$$

where x is the concentration of Mn ions, z_j is the number of lattice positions at a distance R_j , and $J_{\text{VBi}}(R_j)$ is the contribution to the exchange integral from valence band VBi:

$$J_{\text{VBi}}(R_j) = \frac{m_i^* J_i^2 a_0^6}{512 \pi^3 \hbar^2} \frac{\sin(2k_{F,i} R_j) - 2k_{F,i} R_j \cos(2k_{F,i} R_j)}{R_j^4} \exp\left[-\frac{R_j}{\lambda}\right] \quad (5.2)$$

where m_i^* is the effective mass of the carriers in VB_i, J_i and $k_{F,i}$ are the sp-d exchange constant and Fermi wave number for VB_i, respectively, λ is the mean free path of the carriers, and a_0 is the lattice constant. The Mn ions are located on an fcc sublattice of the rocksalt crystal structure at distances $R_j = a_0(j/2)^{1/2}$ from a reference spin. The exchange interaction J_{VB_i} depends on the carrier concentration via $k_{F,i}$.

As was clarified in section 1.3, the contribution from the carriers in the heavy-hole Σ band is dominating for $p > p_c$. Therefore, only this contribution will be considered. The Σ band consists of 12 equivalent valleys, among which the $p_\Sigma = p - p_c$ holes are distributed. If the Σ band is assumed¹¹ to be parabolic and isotropic, $k_{F,\Sigma}$ and p_Σ are related by:

$$k_{F,\Sigma} = \left(\frac{3\pi^2 p_\Sigma}{12} \right)^{1/3} \quad (5.3)$$

This proportionality of $k_{F,\Sigma}$ with $p^{1/3}$ was already used in the previous section to demonstrate that the dependence of the low-temperature magnetic state on the ratio p_Σ/x is in accordance with the assumption of RKKY interactions between the Mn ions.

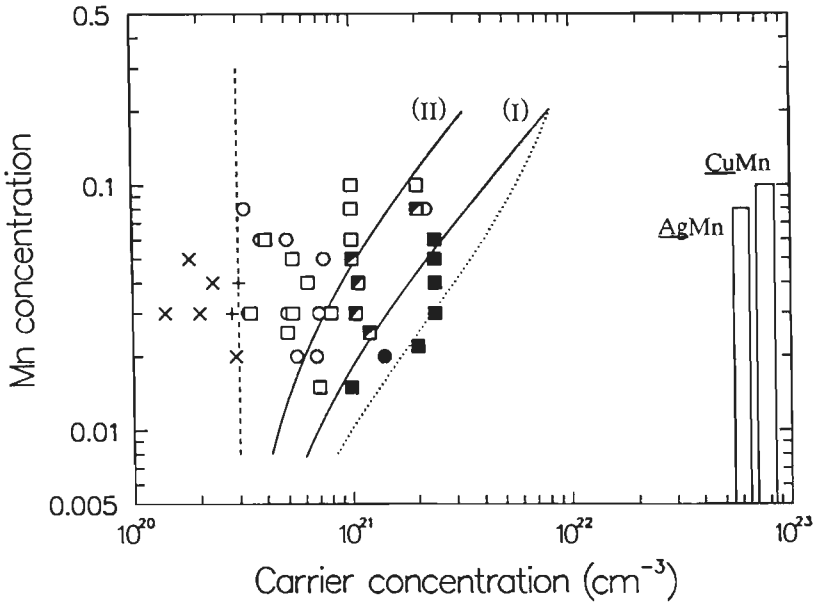


Figure 5.4: The x - p magnetic phase diagram at $T = 1.3$ K of $\text{Sn}_{1-x}\text{Mn}_x\text{Te}$ (squares and +), supplemented with data on $\text{Pb}_{0.28-x}\text{Sn}_{0.72}\text{Mn}_x\text{Te}$ (circles and \times) and canonical spin-glasses. Open symbols: ferromagnetic phase; semi-filled symbols: reentrant spin-glass phase; filled symbols: spin-glass phase; (+, \times): paramagnetic phase. Full curves: $x/p_\Sigma = 0.26$ (I) and $x/p_\Sigma = 0.67$ (II). Dotted curve: Mean Random Field model. Dashed line: $p = p_c = 3 \times 10^{20} \text{ cm}^{-3}$.

5.3.2 Geometrical model

The first attempt to locate the cross-over from ferromagnetic to spin-glass behaviour in the x-p diagram is based on a geometrical consideration of the RKKY interaction. In section 5.2 it was argued that there are two characteristic distances that are important for the low-temperature magnetic behaviour: R_0 , where the first change of sign of the RKKY interaction occurs, and R_{Mn-Mn} , the average spin-spin distance. If $R_0 \ll R_{Mn-Mn}$ there is a strong competition between positive, ferromagnetic interactions and negative, antiferromagnetic interactions, leading to the formation of a spin-glass state. Because of their high carrier concentrations this is the case in the canonical spin glasses displayed at the right-hand side of Fig. 5.4. If $R_0 \gg R_{Mn-Mn}$ ferromagnetic interactions dominate over the oscillatory behaviour and no spin-glass state is formed, but a ferromagnetically ordered state. A transition between the two regimes might be anticipated when⁶

$$R_0 \approx R_{Mn-Mn} \quad (5.4)$$

Now, it will be shown that the condition $R_0 = R_{Mn-Mn}$ indeed corresponds to a constant ratio between the Mn concentration x and the charge carrier concentration p_Σ , as was already stated in the preceding section.

The first change of sign of the RKKY interaction occurs for $2k_F R_0 = 4.49$. R_0 depends on the carrier concentration via the relation between k_F and p_Σ in Eq. (5.3), yielding:

$$R_0 = \frac{4.49}{2k_F} = \frac{4.49}{2} \left(\frac{\pi^2 p_\Sigma}{4} \right)^{-1/3} \quad (5.5)$$

The relation between R_0 and p_Σ is illustrated in Fig. 5.5a.

The other characteristic distance, R_{Mn-Mn} , depends, of course, on the Mn concentration. To relate R_{Mn-Mn} to x , the average volume V per Mn ion is considered. In the rocksalt structure the unit cell contains four formula units $Sn_{1-x}Mn_xTe$, so:

$$V = \frac{a_0^3}{4x} \quad (5.6)$$

with $a_0 = 6.26 \text{ \AA}$. If the volume V per Mn ion is approximated by a sphere with a radius $\frac{1}{2} R_{Mn-Mn}$, it can alternatively be expressed as:

$$V = \frac{4}{3} \pi \left(\frac{R_{Mn-Mn}}{2} \right)^3 \quad (5.7)$$

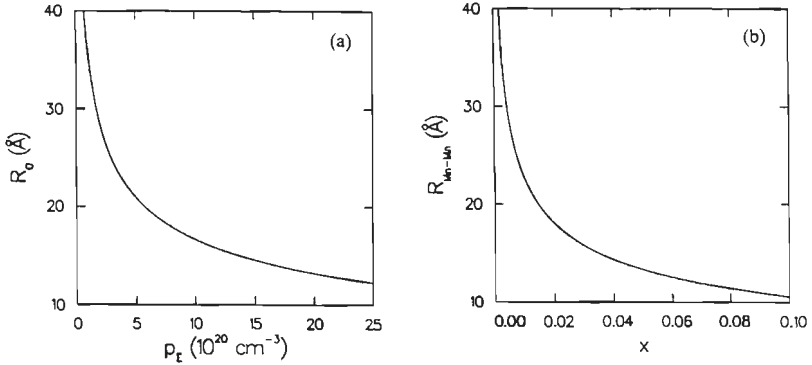


Figure 5.5: (a) Relation between R_0 , the distance at which the first change of sign of the RKKY interaction occurs, and p_z , the charge carrier concentration in the Σ band; (b) Relation between $R_{\text{Mn-Mn}}$, the average distance between two Mn ions, and the Mn concentration x .

Combining Eqs. (5.6) and (5.7) yields:

$$R_{\text{Mn-Mn}} = \left(\frac{3a_0^3}{2\pi x} \right)^{1/3} \quad (5.8)$$

The dependence of $R_{\text{Mn-Mn}}$ on x is illustrated in Fig. 5.5b.

Comparing Figs. 5.5a and 5.5b confirms that, as was mentioned in section 5.2, R_0 and $R_{\text{Mn-Mn}}$ are of the same order of magnitude. Inserting Eqs. (5.5) and (5.8) in (5.4) yields:

$$x = 0.26 p_z \quad (5.9)$$

where x is expressed in % Mn and p_z in units 10^{20} cm^{-3} . The phase boundary expressed by Eq. (5.9) is denoted by the solid line labelled (I) in Fig. 5.4. The agreement with the experimental results is very satisfactory, considering the rather simple argument on which the derivation of Eq. (5.9) is based. Although the line is located somewhat at the high- p side, it indeed appears to be situated in the range of Mn concentrations and carrier concentrations covered by $\text{Sn}_{1-x}\text{Mn}_x\text{Te}$ and $\text{Pb}_{1-x-y}\text{Sn}_y\text{Mn}_x\text{Te}$. For comparison, the line $p_z/x = 1.5$, which was deduced from Fig. 5.2 as the value of p_z/x above which the deterioration of the ferromagnetic order begins, is also shown in Fig. 5.4 as the solid line labelled (II).

In the canonical, metallic RKKY spin-glasses it is not possible to reduce the carrier concentration far enough at constant composition to induce a ferromagnetic ordering. The transitions between a ferromagnetic regime and a spin-glass regime with an intermediate reentrant spin-glass regime reported¹² for systems such as AgFe and AuFe were induced by changing the concentration of magnetic ions and thus " $R_{\text{Mn-Mn}}$ " instead of changing R_0 at constant composition.

5.3.3 Mean Random Field model

In the Mean Random Field (MRF) approximation¹³ the probability $P(H)dH$ is calculated that a spin, positioned in the origin, senses a molecular or internal field between H and $H+dH$. The molecular field acting on spin i is given by:

$$H_i = \frac{2S}{g\mu_B} \sum_{j=1}^N n_j J(R_j) \quad (5.10)$$

where the summation is carried out over N shells of neighbours, in which n_j Mn ions are located, and the RKKY expression (Eqs. (5.1) and (5.2)) is inserted for $J(R_j)$. Each spin has its own configuration, characterised by the number of spins in each shell of neighbours, and corresponding internal field.

The MRF equations describing $P(H)dH$ are¹⁰:

$$P(H) = \frac{1}{2\pi} \int_0^{\infty} e^{-iH\rho} e^{-4\pi n D(\rho)} d\rho \quad (5.11a)$$

with

$$D(\rho) = \int_0^{\infty} r^2 (1 - e^{i\gamma\rho J(r)}) dr \quad (5.11b)$$

where n is the density of magnetic ions ($n = 4x/a_0^3$) and $\gamma = 2S/g\mu_B$. In the MRF model a continuous distribution of the spins is assumed, i.e. not confined to the discrete lattice positions. Because the RKKY interaction diverges at $r = 0$, the integration is in practice not started at $r = 0$, but at $r = R_1$, the smallest distance at which a neighbouring spin can be positioned.¹⁴ Key-parameter for the prediction of the nature of the low-temperature magnetic behaviour is the parameter η_H , defined as:

$$\eta_H \equiv \frac{\langle H \rangle}{\Delta H} \quad (5.12)$$

where $\langle H \rangle$ and ΔH are the mean and the variance of the distribution $P(H)$. The parameter η_H is the MRF-analogue¹⁴ of the Sherrington-Kirkpatrick¹⁵ (SK) parameter η_{SK} . In the SK model η_{SK} is defined analogous to Eq. (5.12) on basis of a distribution of interactions $P(J_{ij})$ instead of internal fields. Sherrington and Kirkpatrick derived that in zero external field a spin-glass phase is formed if $\eta_{SK} < 1$, whereas for $\eta_{SK} > 1.25$ a ferromagnetic phase results. For $1.00 \leq \eta_{SK} \leq 1.25$ a reentrant spin-glass phase is predicted. In the same way the value of $\eta_H(x,p)$ can be used to predict the location of the phase

boundary in the x - p phase diagram¹⁴. However, this would require the calculation of $P(H)$ for a large number of combinations of x and p . Eggenkamp *et al.*⁴ calculated $P(H)$ at $T = 0$ K for $p = 13 \times 10^{20} \text{ cm}^{-3}$ and $x = 0.01$, $x = 0.025$, $x = 0.05$, and $x = 0.10$. Their calculations were performed using an infinite mean free path as well as $\lambda = 40 \text{ \AA}$. The results for $\lambda = 40 \text{ \AA}$ are reproduced in Fig. 5.6. For $x = 0.01$ the distribution is sharply peaked just below $H_i = 0$ T and strongly asymmetric. With increasing Mn concentration the distribution widens, accompanied by a shift of the mean value towards higher fields. Calculating η_H yields a spin-glass state for $x = 0.01$, both for $\lambda = \infty$ and for $\lambda = 40 \text{ \AA}$, whereas for larger concentrations a ferromagnetic state results in both cases. In the case of $\lambda = 40 \text{ \AA}$, η_H increases from $\eta_H = 0.87$ for $x = 0.01$ to $\eta_H = 2.66$ for $x = 0.10$. Using an infinite free mean path widens the distributions and shifts the mean value towards larger internal fields, which turns out to yield a slight increase of η_H .

For $T = 0$ K and $\lambda = \infty$ it is also possible to calculate $\eta_H(x,p)$ analytically, without knowing the exact shape of $P(H)$. We will not present the details of this calculation¹⁶ here, but only the resulting line $\eta_H(x,p) = 1$, the dotted line in Fig. 5.4. Although this line is also located in the range of x and p covered by $\text{Sn}_{1-x}\text{Mn}_x\text{Te}$, as was the case for the geometrical model discussed in the previous section, the agreement with the experimental data is less satisfactory. By accounting for a finite mean free path this might be improved.

Story *et al.*¹⁷ calculated the location of the cross-over from ferromagnetic to spin-glass behaviour in the x - p diagram by calculating the aforementioned SK parameter η_{SK} as a function of x and p . Their approximation can be considered as the discrete analogue of the MRF model: instead of a continuous distribution of spins, the positions of the spins are restricted to the discrete lattice positions. Apart from features resulting from the discrete lattice positions, which are observed for small x , the resulting distributions $P(H)$ have the same shape as those in Fig. 5.6.

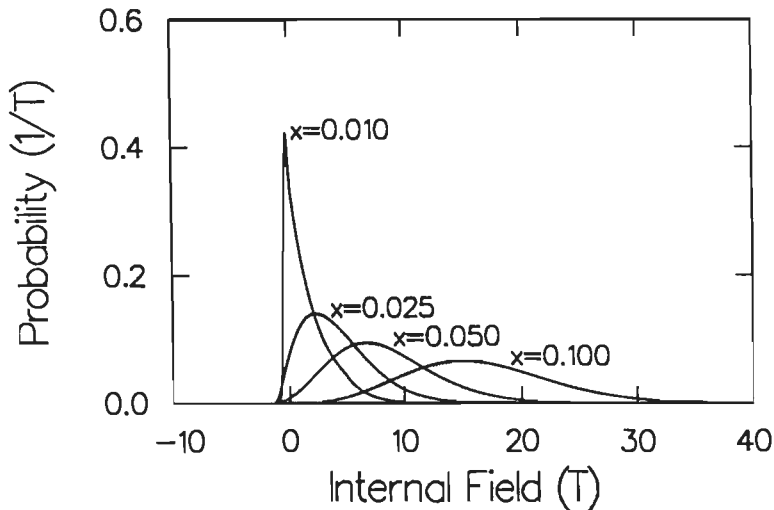


Figure 5.6: Distribution of internal fields, calculated with the Mean Random Field model, for various Mn concentrations (x) with $p = 13 \times 10^{20} \text{ cm}^{-3}$ and $\lambda = 40 \text{ \AA}$. After Ref. 4.

5.4 Discussion

The two models used to predict the location of the crossover from ferromagnetic to spin-glass behaviour in the x - p phase diagram yielded a quantitatively satisfactory agreement with the experimental data. In both cases the boundary line was situated in the range of charge carrier concentrations and Mn concentrations covered by the $\text{Sn}_{1-x}\text{Mn}_x\text{Te}$ samples. In this section an attempt will be made to present a phenomenological picture of the mechanism of the carrier-concentration induced breakdown of the ferromagnetic state. This picture will be developed starting from the literature on other systems in which a transition from ferromagnetic to spin-glass behaviour with an intermediate reentrant spin-glass regime is observed. Once more, it must be emphasised that in all these systems such a transition was not induced by a change in the charge carrier concentration, but by a change in the concentration of magnetic ions.

In particular, we consider the transition from the ferromagnetic to the reentrant spin-glass phase, occurring on cooling a reentrant spin-glass sample. In the literature^{18,19} generally two concepts are used for the description of the mechanism of this transition. The first concept is based on a mean-field treatment of a system of Heisenberg spins, which are coupled by infinitely long-ranged interactions, by Gabay and Toulouse (GT).²⁰ In this concept the transition from the ferromagnetic state to the reentrant spin-glass state is caused by the freezing of the spin components transverse to the direction of the ferromagnetic magnetisation. Essential is that this magnetisation does not vanish at the freezing temperature. Instead, the reentrant spin-glass state is characterised by a coexistence of a long-range ferromagnetic order with a spin-glass "ordering" of the transverse components of the spins. This implies that in this concept the reentrant spin-glass phase is essentially different from the spin-glass phase entered directly from the paramagnetic regime. In the three dimensional phase diagram in Fig. 5.3 this could be reflected, at fixed p , by an extra vertical line, down from the triple point to $T = 0$ K, to separate the two phases.

The second concept describes the ferromagnet to reentrant spin-glass transition in terms of clusters and random fields.^{21,22} In this model the ferromagnetic order, developed below the critical temperature T_c , vanishes at the freezing temperature T_f due to a random field, originating from the freezing of spins that do not participate in the ferromagnetic order. Above T_f an infinite, ferromagnetically ordered network coexists with smaller, magnetically isolated clusters of magnetic ions. This isolation can be the result of percolation as well as frustration. At the freezing temperature the magnetic moments of these clusters freeze in random directions, thereby imposing a random field on the ferromagnetic network. Consequently this network decomposes into finite clusters and the ferromagnetic order is destroyed: no ferromagnetic order exists below T_f , contrary to the GT model.

It is not clear whether there is one unique concept to describe the properties of *all* reentrant spin-glass materials.^{19,23} For example, Mössbauer experiments²⁴ and neutron depolarisation measurements²⁵ on AuFe indicate that indeed a ferromagnetic long-range order coexists with a spin-glass "ordering" of the transverse spin components below T_f , in agreement with the GT model. This can alternatively be described as a canting of

the spins²⁶, as was mentioned in section 3.3, in which possible causes of the observed reduction of the saturation magnetisation in the ferromagnetic samples with $x = 0.06$, $p = 11 \times 10^{20} \text{ cm}^{-3}$ and $x = 0.10$, $p = 14 \times 10^{20} \text{ cm}^{-3}$ were discussed. For other reentrant spin glasses, such as $\text{Eu}_x\text{Sr}_{1-x}\text{S}$ and $(\text{Fe}_{1-x}\text{Mn}_x)_{75}\text{P}_{16}\text{B}_6\text{Al}_3$, the experimental results support the second model. Neutron diffraction experiments²⁷ on these systems demonstrated the absence of a long-range ferromagnetic order in the reentrant spin-glass state. Neutron depolarisation experiments²⁵ on a $\text{Fe}_{1-x}\text{Al}_x$ reentrant spin glass indicated that the long-range ferromagnetic order, existing at temperatures between T_c and T_f , is decomposed into finite clusters below T_f . There are also theoretical arguments²⁸ that in these systems with predominantly short-range interactions a long-range-ordered ferromagnetic phase cannot coexist with a spin-glass freezing of transverse spin components in zero field. The frozen transverse spin components would act as a random field on the ferromagnetic order, and, because the ordered state is unstable against an arbitrarily weak random field²⁸, this random field would destroy the order.

For $\text{Sn}_{1-x}\text{Mn}_x\text{Te}$ the results of the neutron scattering experiments on the reentrant spin-glass sample with $x = 0.04$ and $p = 11 \times 10^{20} \text{ cm}^{-3}$ (section 4.3.3) support the description in terms of clusters and random fields. In zero field the observed ferromagnetic order is never long-ranged, not even in the ferromagnetic state at temperatures between T_c and T_f , and below T_f the range of the order rapidly decreases with decreasing temperature (see Fig. 4.12). Simultaneously, the order parameter decreases, as demonstrated in both the neutron diffraction experiments (Fig. 4.10) and the low-field magnetisation measurements (Fig. 4.6). The great influence of the small external magnetic fields employed in the neutron scattering measurements on this sample can in this concept be understood from a compensation of the random field by the external field.²² In a field of 5.0 mT the ferromagnetic order could not be distinguished from long range order at all temperatures below $T = 4 \text{ K}$. The transition to the spin-glass state was, if not totally absent, at least suppressed down to a temperature below 1.8 K.

Considering that the reentrant spin-glass transition can be explained within a model based on clusters and random fields, it seems worthwhile to try to describe the phenomenon of the carrier-concentration-induced transition from the ferromagnetic to the spin-glass regime in the same terms. An additional argument to do so is that cluster models are also frequently used to explain the experimental properties of canonical spin glasses, especially the frequency dependence of the susceptibility.^{28,29} In these cluster models the spin system is treated as consisting of dynamically evolving magnetic clusters, which develop out of the high-temperature magnetic phase. A cluster is defined as a group of spins, each of which is coupled to at least one other member of the group by an exchange interaction stronger than the disordering thermal energy. Each spin will tend to align according to the internal field imposed on it by neighbouring spins. This does not necessarily imply that all spins within a cluster are ferromagnetically aligned. Spins for which the thermal energy exceeds the energy corresponding to the internal field can exist as loose, isolated spins or as a smaller cluster of spins within a larger cluster. As the temperature is decreased, the exchange interaction becomes more dominating, hence clusters will grow and simultaneously new clusters may be formed.

To describe the carrier-concentration-induced breakdown of the ferromagnetic state at

fixed Mn concentration in terms of a cluster model, it is necessary to consider the effect of the charge carrier concentration on the process of cluster formation. The exchange interaction responsible for the clustering of spins in $\text{Sn}_{1-x}\text{Mn}_x\text{Te}$ is the oscillating RKKY interaction. As already mentioned in section 5.3, the distance R_0 , at which the RKKY interaction has its first switch from ferromagnetic to antiferromagnetic, depends on the carrier concentration. At fixed Mn concentration this distance decreases with increasing carrier concentration, implying that simultaneously the number of Mn ions, which have a significant antiferromagnetic interaction with one or more other Mn ions, increases. Consequently, the number of frustrated spins increases. This frustration is a basic ingredient for the formation of a spin-glass phase.

We assume that at low carrier concentrations all spins are included in very large ferromagnetically aligned clusters, the size of which is in practice only limited by the formation of domains. Within the domains all spins are included in one, "infinite" ferromagnetic network. If the charge carrier concentration is increased, for a certain value of p , which possibly is related to the value of p_z/x for which T_{max}/x goes through a maximum (cf. Fig. 5.2), spins or groups of spins will arise that are frustrated and hence decoupled from the ferromagnetic network. This situation is the one described above in the discussion of the second concept for the mechanism of the reentrant spin-glass transition. As the temperature is lowered from the paramagnetic phase, first a ferromagnetically ordered phase is formed. If the temperature is lowered further, the spins that are not included in the ferromagnetic clusters freeze in random directions and the resulting random field destroys the ferromagnetic order. As p is increased further, the number of not-ferromagnetically-coupled spins will increase and the ferromagnetic ordering temperature will decrease. Simultaneously the freezing temperature will increase, until both temperatures merge and a spin-glass phase is formed directly from the paramagnetic phase.

This model is consistent with the results of the neutron diffraction experiments on the samples with $x = 0.04$ and different carrier concentrations, presented in chapter 4. For the sample with $p = 7 \times 10^{20} \text{ cm}^{-3}$ the observed magnetic intensity was equal to the value expected if all Mn ions were included in ferromagnetic domains, and, moreover, the range of the ferromagnetic order could not be distinguished from infinite. In the case of the sample with $p = 11 \times 10^{20} \text{ cm}^{-3}$ the ferromagnetic order between T_c and T_f is not long-ranged, implying the presence of ferromagnetically aligned clusters of finite size only. This means that for some charge carrier concentration between $p = 7 \times 10^{20} \text{ cm}^{-3}$ and $p = 11 \times 10^{20} \text{ cm}^{-3}$ the number of spins that are not included in the ferromagnetic alignment has grown so far that it is no longer possible to form an infinite ferromagnetic network. Increasing the carrier concentration to $p = 23 \times 10^{20} \text{ cm}^{-3}$ yields the situation where the number of spins that are not ferromagnetically coupled has increased so far, that a spin-glass phase is formed directly from the paramagnetic phase. However, the neutron diffraction experiments indicate the presence of short-ranged ferromagnetic correlations, suggesting that even for this carrier concentration ferromagnetically aligned clusters are still present.

Concerning the other experiments on the $x = 0.04$ samples, the observed frequency dependence of the ac susceptibility for $p = 7 \times 10^{20} \text{ cm}^{-3}$ and $p = 11 \times 10^{20} \text{ cm}^{-3}$ (section

4.2.1) supports the assumption of a cluster model. With each cluster size corresponds a relaxation time, which increases with the size of the cluster. In the ac susceptibility measurements a cluster will appear blocked if its relaxation time exceeds the characteristic time determined by the ac frequency and a blocked cluster does not contribute to the susceptibility.

The experimental results on the ferromagnetic samples with as-grown charge carrier concentrations, presented in chapter 3, are consistent with the cluster model as far as the $x = 0.03$ sample with $p = 7 \times 10^{20} \text{ cm}^{-3}$ is concerned, for which the experimental behaviour is similar to that of the $x = 0.04$ sample with the same carrier concentration. For the samples with $x = 0.06$, $p = 11 \times 10^{20} \text{ cm}^{-3}$ and $x = 0.10$, $p = 14 \times 10^{20} \text{ cm}^{-3}$ the neutron diffraction experiments also revealed the existence of a long-range ordered ferromagnetic phase at low temperatures. However, both the saturation magnetisation deduced from the neutron diffraction experiments and that determined from high-field magnetisation measurements were significantly below the value expected for $S = 5/2$ and the nominal Mn concentrations. In the discussion in section 3.3 a number of possible explanations for this reduction were suggested, two of which are very much analogous to the two mechanisms used in the literature to describe the reentrant spin-glass transition. The first one, a canting or reduction of the spin of each Mn ion, was in fact already rejected in section 3.3. The second explanation was the existence of groups of antiferromagnetically coupled Mn ions that do not take part in the ferromagnetic ordering. These groups should persist as isolated regions within an infinite ferromagnetic network down to $T = 0 \text{ K}$. At first sight the existence of groups of spins that are not included in the infinite ferromagnetic network is not inconsistent with the cluster model. However, if the RKKY interaction alone would be effective, all Mn ions might be expected to be included in an infinite ferromagnetic network for these combinations of carrier concentration and Mn concentration and there would be no reason for the observed reduction of the saturation magnetisation. This suggests the presence of other, non-RKKY, antiferromagnetic nearest-neighbour interactions, the role of which increases for high Mn concentrations. The fact that for $x = 0.04$ and, if we take the value determined from the neutron scattering experiments (section 3.2.1), also for $x = 0.03$ no significant reduction of the saturation magnetisation is observed, is in agreement with this explanation. It is obvious that the model described here is highly qualitative. A complete theoretical description for the phenomenon of the carrier-concentration-induced breakdown of ferromagnetism is not yet available. More experimental data are necessary to enable the development of such description. In the next section a number of suggestions for future experiments will be presented.

5.5 Suggestions for further research

Some experiments to augment and extend the work described in this thesis have already been proposed in the discussions at the end of the chapters 3 and 4. Some of them will be repeated in this section, where a number of suggestions for further research will be

given, starting from the three-dimensional magnetic phase diagram in Fig. 5.3. The extension of the experiments described in the foregoing chapters towards temperatures below 1.5 K is essential for two reasons: first, to establish the exact position of both boundaries of the spin-glass regime, and, second, to further substantiate the characterisation of the (reentrant) spin-glass phase. For this latter purpose field cooled and zero field cooled magnetisation measurements should be performed, since differences between the field cooled and the zero field cooled magnetisation are generally considered as one of the characteristic features of a spin glass.³⁰

Concerning the neutron diffraction experiments, especially for the reentrant spin-glass sample ($x = 0.04$, $p = 11 \times 10^{20} \text{ cm}^{-3}$) measurements below 1.8 K are necessary to establish whether the spontaneous magnetisation indeed completely vanishes and to monitor the decrease of the size of the ferromagnetically ordered clusters in zero field. Possibly inelastic effects similar to those observed in the spin glass sample with $x = 0.04$ and $p = 23 \times 10^{20} \text{ cm}^{-3}$ might occur. The influence of the magnetic field should also be studied in more detail. For the sample with $p = 23 \times 10^{20} \text{ cm}^{-3}$ experiments with a better energy resolution might clarify the nature of the fluctuation processes that cause the observed differences between the measurements with analyser and those without. This kind of experiments could be facilitated by using a sample with a higher freezing temperature, for example the $x = 0.06$ spin-glass sample (Fig. 5.1), for which $T_f \approx 3.5 \text{ K}$.

Along the x -axis an extension of the phase diagram in Fig. 5.3 is possible in both directions. Experiments on samples with $x \leq 0.02$ and carrier concentrations just above p_c could reveal whether there is a lower limit in x for the existence of a ferromagnetically ordered phase. However, Mn concentrations below $x = 0.03$ must be considered as too small for neutron diffraction experiments. For samples with $x \geq 0.10$ an increasing importance of direct antiferromagnetic interactions may be expected. It would be interesting to investigate how the saturation magnetisation develops as x is increased, and also whether there is an upper limit for the existence of a ferromagnetic phase. Besides the extension to lower and higher x it is also necessary to obtain more data in the range $0.02 \leq x \leq 0.10$, for example on the saturation magnetisation for Mn concentrations between $x = 0.06$ and $x = 0.10$.

Along the p -axis there is a lack of data in the range $11 \times 10^{20} \text{ cm}^{-3} \leq p \leq 20 \times 10^{20} \text{ cm}^{-3}$. Measurements on samples with carrier concentrations in this range are indispensable to study the gradual breakdown of the ferromagnetic order. However, thus far it has been difficult to precisely control the isothermal annealing process. It is not yet possible to tune the annealing parameters in such a way that every desired carrier concentration can be achieved. Variation of the annealing temperature and/or the source material are possible approaches to reach carrier concentrations other than in the ranges $5 - 7 \times 10^{20} \text{ cm}^{-3}$ or $20 - 23 \times 10^{20} \text{ cm}^{-3}$. For example, using Zn as source material instead of Sn yields carrier concentrations below p_c , as described in section 2.2. Instead of annealing as-grown material, it might also be possible to *grow* material with a charge carrier concentration different from $p = 9 - 11 \times 10^{20} \text{ cm}^{-3}$. According to the Sn-Te phase diagram (Fig. 2.4) another cation-anion ratio in the starting materials should lead to another carrier concentration. Another possibility is the replacement in the starting materials of a few

percent Sn by an element with a valency other than +2. Preliminary experiments with up to 3 % In as dopant in material with 3 % Mn yielded lower carrier concentrations than in undoped 3 % Mn material, but there are indications that the magnetic properties are also changed in comparison to undoped $\text{Sn}_{0.97}\text{Mn}_{0.03}\text{Te}$ with the same carrier concentration. Doping will be inevitable to reach charge carrier concentrations above $p = 23 \times 10^{20} \text{ cm}^{-3}$ (see Fig. 2.4).

In principle, the related compound $\text{Pb}_{1-x}\text{Sn}_y\text{Mn}_x\text{Te}$ offers better opportunities to study the gradual breakdown of the ferromagnetic state with increasing charge carrier concentration. In comparison with the (T,p) phase diagram of SnTe (Fig. 2.4), the shape of the (T,p) phase diagram of $\text{Pb}_{1-y}\text{Sn}_y\text{Te}$ makes it easier to tune the desired carrier concentration by variation of the annealing temperature. The maximum achievable carrier concentration, however, decreases with increasing Pb concentration, which could have the disadvantage that the *complete* transition from ferromagnetic to spin-glass behaviour at fixed x might be observable for small x only. Thus far, a carrier-concentration-induced breakdown of a ferromagnetic order has been reported³¹ for $\text{Pb}_{0.28-x}\text{Sn}_{0.72}\text{Mn}_x\text{Te}$ with carrier concentrations $p \leq 15 \times 10^{20} \text{ cm}^{-3}$ for $x = 0.015$ and $x = 0.02$, but for $x = 0.04$ the effect was not observed. The data for $x = 0.02$, with six different carrier concentrations in the range $5 \times 10^{20} \text{ cm}^{-3} \leq p \leq 15 \times 10^{20} \text{ cm}^{-3}$, show that the breakdown of the ferromagnetic state with increasing carrier concentration is a gradual process, in accordance with the data for $\text{Sn}_{1-x}\text{Mn}_x\text{Te}$ in Fig. 5.2.

Only little attention has been paid to the semiconducting properties of $\text{Sn}_{1-x}\text{Mn}_x\text{Te}$ in the present work. Very little is known yet on how properties such as the band gap, the energy difference between the maxima of the two valence bands, the effective masses of the carriers in the two bands, and the mean free path, depend on the Mn concentration and on the charge carrier concentration. For the calculations in the two-band RKKY model a detailed knowledge of these properties is indispensable.

References

1. W.J.M. de Jonge, H.J.M. Swagten, S.J.E.A. Eltink, and N.M.J. Stoffels, *Semicond. Sci. Technol.* **5**, S131 (1990).
2. C.W.H.M. Vennix, E. Frikkee, H.J.M. Swagten, K.Kopinga, and W.J.M. de Jonge, *J. Appl. Phys.* **69**, 6025 (1991).
3. W.J.M. de Jonge, T. Story, H.J.M. Swagten, and P.J.T. Eggenkamp, *Europhys. Lett.* **17**, 631 (1992).
4. P.J.T. Eggenkamp, T. Story, H.J.M. Swagten, C.W.H.M. Vennix, C.H.W. Swüste, and W.J.M. de Jonge, *Semicond. Sci. Technol.* **8**, S152 (1993).
5. T. Story, P.J.T. Eggenkamp, C.H.W. Swüste, H.J.M. Swagten, W.J.M. de Jonge, and L.F. Lemmens, *Phys. Rev. B* **45**, 1660 (1992).
6. A. Mauger and M. Escorne, *Phys. Rev. B* **35**, 1902 (1987).
7. T. Story, R.R. Galazka, R.B. Frankel, and P.A. Wolff, *Phys. Rev. Lett.* **56**, 777 (1986).
8. H.J.M. Swagten, W.J.M. de Jonge, R.R. Galazka, P. Warmenbol, and J.T. Devreese, *Phys. Rev. B* **37**, 9907 (1988).
9. T. Story, G. Karczewski, L. Swierkowski, and R.R. Galazka, *Phys. Rev. B* **42**, 10477 (1992).
10. J.A. Mydosh and G.J. Nieuwenhuys, in *Ferromagnetic Materials*, vol. 1, E.P. Wohlfarth, editor (North Holland, Amsterdam, 1980).
11. G. Karczewski, L. Swierkowski, T. Story, A. Szczerbakow, J. Niewodniczanska-Blinowska, and G. Bauer, *Semicond. Sci. Technol.* **5**, 1115 (1990).
12. G.J. Nieuwenhuys, B.J. Verbeek, and J.A. Mydosh, *J. Appl. Phys.* **50**, 1685 (1979).
13. M. Klein, *Phys. Rev.* **173**, 552 (1968).
14. D. Sherrington and S. Kirkpatrick, *Phys. Rev. Lett.* **35**, 1792 (1975).
15. M. Klein, *Phys. Rev. B* **14**, 5008 (1976).
16. H.J.M. Swagten and P.J.T. Eggenkamp, to be published.
17. T. Story, C.H.W. Swüste, H.J.M. Swagten, and P.J.T. Eggenkamp, unpublished.
18. K. Binder and A.P. Young, *Rev. Mod. Phys.* **58**, 801 (1986).
19. J.L. Dormann and M. Nogues in *Proc. of the 3rd Int. Conf. on Physics of Magnetic Materials*, Szczyrk-Bila, Poland, p. 531 (1986).
20. M. Gabay and G. Toulouse, *Phys. Rev. Lett.* **47**, 201 (1981).
21. B.R. Coles, B.V. Sarkissian, and R.H. Taylor, *Phil. Mag. B* **37**, 489 (1978).
22. G. Aeppli, S.M. Shapiro, R.J. Birgeneau, and H.S. Chen, *Phys. Rev. B* **28**, 5160 (1983).
23. B.R. Coles, *Phil. Mag. B* **49**, L21 (1984).
24. I.A. Campbell, S. Senoussi, F. Varret, J. Teillet, and A. Hamzic, *Phys. Rev. Lett.* **30**, 1615 (1983).
25. S. Mitsuda, H. Yoshizawa, and Y. Endoh, *Phys. Rev. B* **45**, 9788 (1992).
26. M. Escorne, M. Godinho, J.L. Tholence, and A. Mauger, *J. Appl. Phys.* **57**, 3424 (1985).
27. G. Aeppli, S.M. Shapiro, H. Maletta, R.J. Birgeneau, and H.S. Chen, *J. Appl.*

- Phys. **55**, 1628 (1984).
28. Y. Imry and S. Ma, Phys. Rev. Lett. **35**, 1399 (1975).
 29. D.A. Smith, J. Phys. F **5**, 2148 (1975).
 30. C.Y. Huang, J. Magn. Magn. Mater. **51**, 1 (1985).
 31. T. Story, R.R. Galazka, P.J.T. Eggenkamp, H.J.M. Swagten, and W.J.M. de Jonge, Acta Phys. Pol. **82**, 630 (1992).

Summary

Diluted magnetic semiconductors are compound semiconductors in which a part of the nonmagnetic cations has been randomly substituted by magnetic ions. These materials are of interest, from the fundamental as well as from the technological point of view, because of their semiconducting and their magnetic properties, and also because of the close relationship between these properties. The research described in this thesis was concentrated on the magnetic correlations in the compound $\text{Sn}_{1-x}\text{Mn}_x\text{Te}$, with $x \leq 0.10$, which has the special property that its magnetic behaviour is determined not only by the temperature (T) and the concentration of magnetic ions (x), but also by the charge carrier concentration (p). At the start of the present research, $\text{Sn}_{1-x}\text{Mn}_x\text{Te}$ was known to display the so-called carrier-concentration-induced ferromagnetism, which had previously been discovered in the related compound $\text{Pb}_{1-x-y}\text{Sn}_y\text{Mn}_x\text{Te}$. This phenomenon is characterised by the existence of a critical carrier concentration p_c , which is critical with respect to the low-temperature magnetic behaviour. For samples with p reduced below p_c paramagnetic behaviour is observed, whereas for $p > p_c$ the results of measurements of the susceptibility, the magnetisation, and the magnetic specific heat indicate the presence of a ferromagnetic-like state. In earlier publications the low-temperature magnetic phase of $\text{Sn}_{1-x}\text{Mn}_x\text{Te}$ with as-grown carrier concentrations $p > p_c$ had already been identified as ferromagnetic by several authors, but the existence of a (reentrant) spin-glass phase had also been reported. The first aim of the present work was to resolve this discrepancy by the characterisation of the low-temperature magnetic phase of samples with as-grown carrier concentrations $p > p_c$ by means of neutron diffraction experiments. With the aid of neutron diffraction it is possible to gain insight not only in the nature of the magnetic correlations, but also in their range.

The discovery of the carrier-concentration-induced ferromagnetism was the first demonstration that the charge carrier concentration has to be included as a parameter in the magnetic phase diagram, besides the temperature and the Mn concentration. The second and major aim of the research described in this thesis was the extension of this three-dimensional (T, x, p) magnetic phase diagram. Especially the extension towards higher charge carrier concentrations was the subject of interest, to study how the ferromagnetic-like behaviour, observed for p just above p_c , is affected by an increase of the carrier concentration.

In chapter 1 a short introduction on diluted magnetic semiconductors in general is given, followed by a survey of the literature on $\text{Sn}_{1-x}\text{Mn}_x\text{Te}$ and $\text{Pb}_{1-x-y}\text{Sn}_y\text{Mn}_x\text{Te}$. This survey includes an experimental and theoretical description of the carrier-concentration-induced ferromagnetism. Chapter 2 deals with a number of experimental aspects. The growth of the single crystals and the isothermal annealing procedures applied to change the carrier concentration of an as-grown crystal are described. Attention is paid to the determination of the crystal structure of $\text{Sn}_{1-x}\text{Mn}_x\text{Te}$. Some basic concepts of neutron diffraction are also treated.

In chapters 3 and 4 the experimental results are presented. In both chapters the results of single crystal neutron diffraction experiments are combined with those of measurements

of the ac susceptibility, the magnetisation (both low- and high-field), and the magnetic specific heat. In chapter 3, the low-temperature magnetic phase of $\text{Sn}_{1-x}\text{Mn}_x\text{Te}$ with as-grown, $p > p_c$, charge carrier concentrations and $x = 0.03$, $x = 0.06$, and $x = 0.10$ is characterised as a long-range-ordered ferromagnetic phase. However, for the crystals with $x = 0.06$ and $x = 0.10$ the observed saturation magnetisation, both that deduced from the neutron diffraction experiments and that from high-field magnetisation measurements, amounts to only roughly 80 % of the theoretical saturation magnetisation. A possible origin for this reduction is found in the presence of groups of antiferromagnetically coupled Mn ions, that do not take part in the ferromagnetic ordering. No indications for the existence of a (reentrant) spin-glass phase are found for the combinations of x and p discussed in chapter 3.

The effect of an increase of the charge carrier concentration on the low-temperature magnetic behaviour at fixed Mn concentration is the subject of chapter 4. Three $x = 0.04$ crystals, all with $p > p_c$, are studied. The experimental results demonstrate a carrier-concentration-induced breakdown of ferromagnetism. In the crystal with the lowest carrier concentration a transition from the paramagnetic phase to a long-range-ordered ferromagnetic phase takes place at low temperature, whereas in the crystal with the highest carrier concentration a direct transition from the paramagnetic phase to a spin-glass phase occurs. In the crystal with the intermediate carrier concentration two transitions are observed on cooling from the paramagnetic phase: an initial transition to a state with a ferromagnetic order of restricted range is followed by a transition to a reentrant spin-glass phase at lower temperature. Such a carrier-concentration-induced transition from a ferromagnetic phase to a spin-glass phase at fixed concentration of magnetic ions has thus far not been observed in any other material.

In chapter 5 the results from chapters 3 and 4 are combined with those on other combinations of x and p in a three-dimensional (T, x, p) magnetic phase diagram. The ferromagnet to spin-glass transition, that is observed for $x = 0.04$, can also be observed for other values of x . With increasing Mn concentration it is shifted towards higher carrier concentration, which can be explained within an RKKY model for the interactions between the magnetic ions. The location of the ferromagnet to spin-glass crossover in the x - p plane is calculated, under the assumption of RKKY interactions, in two different ways. The first calculation is based on geometrical considerations, the second on the Mean Random Field model. Subsequently a qualitative description of the carrier-concentration-induced breakdown of ferromagnetism is given in terms of a cluster model. In the last section some suggestions for further research are presented. Extension of the experiments towards the temperature range below $T = 1.3$ K and research on methods to change the carrier concentration continuously in a controllable way deserve priority.

Samenvatting

Verdunde magnetische halfgeleiders zijn halfgeleiderlegeringen, waarin een deel van de niet-magnetische kationen vervangen is door magnetische ionen. Deze materialen zijn, zowel vanuit fundamenteel als vanuit technologisch oogpunt gezien, interessant vanwege hun eigenschappen als halfgeleider, vanwege hun eigenschappen als verdund magnetisch systeem, en ook vanwege de nauwe samenhang tussen deze eigenschappen. Het in dit proefschrift beschreven onderzoek was geconcentreerd op de magnetische correlaties in de verbinding $\text{Sn}_{1-x}\text{Mn}_x\text{Te}$, met $x \leq 0.10$. Dit materiaal heeft de bijzondere eigenschap dat het magnetische gedrag niet alleen bepaald wordt door de temperatuur (T) en de concentratie van de magnetische ionen (x), maar ook door de concentratie van de elektrische laders (p). Bij het begin van dit onderzoek was reeds bekend dat er een kritieke ladersconcentratie p_c bestaat voor het magnetische gedrag bij lage temperaturen van $\text{Sn}_{1-x}\text{Mn}_x\text{Te}$. Preparaten waarvan p verlaagd was tot beneden p_c vertonen paramagnetisch gedrag, terwijl voor preparaten met $p > p_c$ de resultaten van metingen van de susceptibiliteit, de magnetisatie, en de soortelijke warmte wijzen op een overgang naar een ferromagnetisch geordende toestand bij afnemende temperatuur. In de literatuur over het magnetische gedrag bij lage temperatuur van $\text{Sn}_{1-x}\text{Mn}_x\text{Te}$, die in het algemeen betrekking had op preparaten met $p > p_c$, was al eerder melding gemaakt van het optreden van een ferromagnetische ordening, maar ook het bestaan van een (reënterante) spinglasfase was gerapporteerd. Het eerste doel van het hier beschreven onderzoek was duidelijkheid te verkrijgen met betrekking tot deze schijnbaar tegenstrijdige resultaten door het karakteriseren van de magnetische fase bij lage temperatuur in $\text{Sn}_{1-x}\text{Mn}_x\text{Te}$ preparaten met $p > p_c$ door middel van neutronendiffractie-experimenten. Met behulp van neutronendiffractie is het niet alleen mogelijk om inzicht te verkrijgen in de aard van de magnetische ordening, maar ook in de dracht van die ordening.

De ontdekking van het bestaan van p_c was de eerste aanwijzing dat de ladersconcentratie als parameter moet worden opgenomen in het magnetische fasediagram, naast de temperatuur en de Mn-concentratie. De verdere uitbreiding van dit driedimensionale (T, x, p) magnetische fasediagram vormde het tweede en belangrijkste doel van het onderzoek. Het betrof met name de uitbreiding naar grotere ladersconcentraties, om na te gaan of, en, zo ja, hoe het ferromagnetische gedrag, zoals waargenomen voor p net boven p_c , verandert als de ladersconcentratie vergroot wordt.

In hoofdstuk 1 wordt een korte, algemene inleiding over verdunde magnetische halfgeleiders gegeven, gevolgd door een overzicht van de literatuur over $\text{Sn}_{1-x}\text{Mn}_x\text{Te}$ en de verwante verbinding $\text{Pb}_{1-x-y}\text{Sn}_y\text{Mn}_x\text{Te}$. Dit overzicht bevat onder andere een experimentele en theoretische beschrijving van de door een verandering in de ladersconcentratie veroorzaakte overgang van para- naar ferromagnetisch gedrag bij $p = p_c$. In hoofdstuk 2 wordt een aantal experimentele aspecten behandeld. De kristalgroei en de methodes die worden gebruikt om de ladersconcentratie van een gegroeid kristal te veranderen worden besproken, en ook wordt aandacht besteed aan de bepaling van de kristalstructuur van $\text{Sn}_{1-x}\text{Mn}_x\text{Te}$. Ook een aantal basisbegrippen van de neutronendiffractie wordt geïntroduceerd.

De experimentele resultaten worden gepresenteerd in de hoofdstukken 3 en 4. In beide hoofdstukken worden de resultaten van neutronendiffractie-experimenten aan eenkristallen gecombineerd met die van metingen van de ac susceptibiliteit, de magnetisatie (zowel in laag als in hoog veld), en de magnetische soortelijke warmte. In hoofdstuk 3 wordt de magnetische fase bij lage temperatuur in niet nabehandelde ("as-grown") $\text{Sn}_{1-x}\text{Mn}_x\text{Te}$ kristallen, dat wil zeggen met ladingsdragersconcentratie $p > p_c$, met $x = 0.03$, $x = 0.06$, en $x = 0.10$, gekarakteriseerd als een fase met een lange-dracht ferromagnetische ordening. Hierbij moet wel de kanttkening worden gemaakt dat voor de kristallen met $x = 0.06$ en $x = 0.10$ de waargenomen verzadigingsmagnetisatie, zowel die afgeleid uit de neutronendiffractie-experimenten als die uit hoog veld magnetisatiemetingen, slechts ongeveer 80 % bedroeg van de theoretische waarde. Een mogelijke oorzaak hiervan zou kunnen zijn het voorkomen van groepjes antiferromagnetisch gekoppelde Mn ionen, die niet deelnemen aan de ferromagnetische ordening. Voor de combinaties van x en p die in hoofdstuk 3 worden besproken, zijn geen aanwijzingen gevonden voor het bestaan van een (reëtrante) spinglasfase.

Het effect op het magnetische gedrag bij lage temperatuur van het vergroten van de ladingsdragersconcentratie bij vaste Mn concentratie wordt onderzocht in hoofdstuk 4. Drie kristallen met $x = 0.04$ en verschillende $p > p_c$ zijn onderzocht. De resultaten leiden tot de conclusie dat door een vergroting van de ladingsdragersconcentratie de afbraak van de ferromagnetisch geordende toestand veroorzaakt wordt. In het preparaat met de laagste ladingsdragersconcentratie treedt bij lage temperatuur een overgang van de paramagnetische fase naar een toestand met een lange-dracht ferromagnetische ordening op, vergelijkbaar met de resultaten uit hoofdstuk 3. In het preparaat met de hoogste ladingsdragersconcentratie vindt een rechtstreekse overgang van de paramagnetische fase naar een spinglastoestand op. Het kristal met de tussenliggende ladingsdragersconcentratie vertoont een dubbele overgang bij afkoeling vanuit de paramagnetische fase: een eerste overgang naar een toestand met een ferromagnetische ordening met een beperkte dracht wordt gevolgd door een overgang naar een reëtrante spinglasfase. Een dergelijke, door een verandering in de ladingsdragersconcentratie geïnduceerde, overgang van een ferromagnetische fase naar een spinglasfase bij een vaste concentratie magnetische ionen is tot dusver in geen enkel ander materiaal waargenomen.

In hoofdstuk 5 worden de resultaten uit de hoofdstukken 3 en 4 gecombineerd met die voor andere combinaties van x en p in een driedimensionaal (T, x, p) magnetisch fasediagram. De overgang van ferromagneet naar spinglas, die voor $x = 0.04$ is waargenomen, blijkt ook voor andere waarden van x op te treden. Met toenemende Mn concentratie verschuift de overgang naar grotere ladingsdragersconcentratie. Dit kan verklaard worden binnen een RKKY-model voor de interacties tussen de magnetische ionen. De grens tussen de ferromagnetische en de spinglasfase in het x - p vlak wordt onder aanname van deze RKKY-interacties op twee manieren berekend. De eerste methode is gebaseerd op een geometrische beschouwing van de RKKY-interactie en de tweede op het zogenaamde Mean Random Field model. Na deze kwantitatieve beschouwingen wordt een kwalitatieve beschrijving van de afbraak van de ferromagnetisch geordende toestand ten gevolge van een verandering in de ladingsdragersconcentratie gegeven in termen van een clustermodel. Tenslotte wordt een aantal suggesties voor verder onderzoek

gegeven, waarbij vooral het belang van experimenten bij temperaturen beneden 1.3 K, en onderzoek naar het gecontroleerd en continu variëren van de ladingsdragersconcentratie wordt benadrukt.

Dankwoord

Op deze plaats wil ik iedereen bedanken die de afgelopen jaren op enigerlei wijze heeft bijgedragen aan het in dit proefschrift beschreven werk. Een aantal mensen wil ik graag met name noemen. De promotoren Evert Frikkee en Wim de Jonge en de copromotor Klaas Kopinga, wil ik bedanken voor de uitstekende begeleiding en hun voortdurende belangstelling. Henk Swagten en Paul Eggenkamp, die als promovendus in Eindhoven onmisbare bijdragen hebben geleverd aan het onderzoek, voor de uiterst plezierige en uiterst collegiale samenwerking en voor het in goede banen leiden van de in Eindhoven uitgevoerde experimenten. Rinus Broekmans, Stephan Eltink, Marc Haast, Ad de Laat, Ton Menting, Marc van Opstal, Nico Stoffels, en Marc Willekens, de studenten die deze experimenten uitvoerden, bedank ik voor hun inzet daarbij, en een aantal van hen ook voor hun inzet tijdens de gezamenlijke lunches. Aad Bontenbal, Herman Plas, en Erwin Werkhoven voor hun technische ondersteuning binnen en buiten de reactorhal. Tot slot dank ik alle leden en ex-leden van de groepen Vaste Stof Fysica en Structurele Karakterisering van ECN voor de prettige dagelijkse werksfeer en de leden van de groep Coöperatieve Verschijnselen in Eindhoven voor de altijd gastvrije ontvangst en eveneens prettig te noemen sfeer aldaar.

Curriculum Vitae

22 september 1964 Geboren te Oost-, West- en Middelbeers.

1976-1982 V.W.O., Rythoviuscollege, Eersel.

1982-1987 Studie Technische Natuurkunde aan de Technische Universiteit Eindhoven.

Afgestudeerd in de groep Coöperatieve Verschijnselen en Fysische Materiaalkunde van de vakgroep Vaste Stof Fysica. Afstudeeronderzoek "Thermokracht- en geleidingsmetingen aan overgangsmetaaloxiden", onder begeleiding van dr. dipl. ing. phys. A.D.D. Broemme en dr. ir. V.A.M. Brabers.

1987-1988 Militaire dienst.

1989-1993 Promovendus in dienst van het Energieonderzoek Centrum Nederland (ECN) te Petten.

Promotieonderzoek "Magnetic correlations in the diluted magnetic semiconductor $\text{Sn}_{1-x}\text{Mn}_x\text{Te}$ ", uitgevoerd in samenwerking met de groep Coöperatieve Verschijnselen en Fysische Materiaalkunde van de vakgroep Vaste Stof Fysica van de faculteit der Technische Natuurkunde van de Technische Universiteit Eindhoven.

Stellingen

behorende bij het proefschrift

**Magnetic correlations in the diluted
magnetic semiconductor $\text{Sn}_{1-x}\text{Mn}_x\text{Te}$**

An experimental study

C.W.H.M. Vennix

8 oktober 1993

1. In hun beschouwing van het (T,x) magnetische fasediagram van $\text{Sn}_{1-x}\text{Mn}_x\text{Te}$ besteden Mauger en Escorne onvoldoende aandacht aan de rol van de ladingsdragersconcentratie.

A. Mauger en M. Escorne, Phys. Rev. B 35, 1902 (1987); dit proefschrift, hoofdstuk 5.

2. Het precieze effect van waterstofpassivering van silicium ten behoeve van de fabricage van zonnecellen blijft onzeker zolang niet is aangetoond waar en hoeveel waterstof in de cel komt.
3. Het is niet terecht om bij de interpretatie van magnetoweerstand- en magnetisatiemetingen aan Co/Cu multilagen reeds uit te gaan van een kubische anisotropie op basis van hysteresecurven, waarbij het extern aangelegde magnetische veld slechts langs twee richtingen is gevarieerd.

F. Giron, P. Boher, Ph. Houdy, P. Beauvillain, K. Le Dang, en P. Veillet, J. Magn. Magn. Mater. 121, 318 (1993).

4. In tegenstelling tot wat Laaksonen en Clementi beweren, is het wel mogelijk om de interne energie van gesmolten natriumchloride te berekenen door middel van een moleculaire dynamica simulatie, gebaseerd op ab initio paarpotentialen. De rigide-ion benadering moet dan ook bij de paarpotentiaalbepaling gebruikt worden, en niet alleen bij de simulatie.

A. Laaksonen en E. Clementi, Mol. Phys. 56, 495 (1985).

5. Indien de boriumdistributie in het te bestralen doelgebied bij de kankertherapie BNCT (boron neutron capture therapy) onbekend is, volstaat een "treatment planning" dosisberekening die gebaseerd is op empirisch bepaalde neutrontransportverschijnselen in referentieomstandigheden.

C.P.J. Raaijmakers, L. Dewit, M.W. Konijnenberg, B.J. Mijnheer, R.L. Moss, en F. Stecher-Rasmussen in "Boron Neutron Capture Therapy", D. Gabel and R.L. Moss (eds.), Plenum Press, New York, 1992.

6. Bij de reacties van 14 MeV neutronen op de wand van een fusiereactor spelen multi-step directe kernreacties een grotere rol dan tot nu toe werd aangenomen.
7. Het door Gijs *et al.* consequent gebruiken van de term "pilaren" voor hun met behulp van microlithografie verkregen meetstructuren in Fe/Cr multilagen ter bepaling van de zogenaamde CPP (current perpendicular to plane) magnetoweerstand, zou de lezer op verkeerde gedachten kunnen brengen.

M.A.M. Gijs, S.K.J. Lenczowski, en J.B. Giesbers, Phys. Rev. Lett. 70, 3343 (1993); M.A.M. Gijs, J.B. Giesbers, S.K.J. Lenczowski, en H.H.J.M. Janssen, Appl. Phys. Lett. 63, 111 (1993).

8. Brownse dynamica simulaties zijn ongeschikt voor het bestuderen van enzyme-substraat reacties. Beter is het gebruik te maken van continuüm/ Navier-Stokes hydrodynamica.

S.H. Northrup, S.A. Allison, en J.A. McCammon, J. Chem. Phys. 80, 1517 (1984).

9. De gevolgen van de sluiting van de faciliteiten voor neutronenverstrooiing bij de Hoge Flux Reactor in Petten zijn slechts voor een deel te ondervangen door het uitvoeren van experimenten bij buitenlandse bronnen.
10. Als de nood het hoogst is, is de ontredding nabij.
11. Weelderige haargroei op de borst moet niet zozeer beschouwd worden als een teken van mannelijkheid, als wel van een evolutieachterstand.